Università degli Studi di Padova
Facoltà di Ingegneria
Dipartimento di Ingegneria dell'Informazione

Tesi di Dottorato

Multiuser mimo downlink systems with limited feedback and Remote sensing of vital signs

PhD Candidate: Ermanna Conte

Advisor: Dr. Stefano Tomasin

Padova, January 29, 2010

Contents

List of Figures

List of Tables

Sommario

Questa tesi di dottorato raccoglie i contributi principali dell'attività di ricerca svolta durante i tre anni del mio percorso di dottorato. Come suggerisce il titolo, l'attivita' di ricerca condotta in questo triennio è divisa in due parti principali. La prima riguarda l'argomento di ricerca che ho seguito sin dall'inizio sui sistemi di downlink Multiuser MIMO con feedback limitato; è parte di un ampio filone di ricerca finalizzato alla progettazione della quarta generazione di sistemi cellulari, e piu' in generale di futuri sistemi di comunicazioni wireless con terminali mobili. In particolare, i miei studi si sono concentrati sui sistemi cellulari in cui le stazioni base sono provviste di antenne multiple; la presenza di piu' antenne alla stazioni base fornisce dei gradi di liberta' nelle comunicazioni di downlink, ovvero nelle comunicazioni dalla stazioni base ai terminali mobili, che possono essere utilizzati per servire piu' di un utente simultaneamente e ottenere un rate piu' elevato rispetto al caso singola antenna. A tal fine e' pero' necessario fornire alla stazioni base la conoscenza dei canali di downlink per ciascuno degli utenti che intende servire; tanto piu' fine e' la stima del canale in possesso della stazioni base, tanto maggiore e' il rate raggiungibile in questo schema di downlink. La progettazione di strategie di feedback, con cui i terminali trasmettono su un canale dedicato informazioni sul canale di downlink alla stazioni base e' quindi un aspetto di grande interesse, essendo il canale di feedback a rate limitato (dell'ordine di qualche bit/simbolo). In particolare, mi sono occupata della scelta del quantizzatore e delle strategie di feedback che tenessero conto della correlazione temporale del canale. All'inizio del triennio (gennaio 2007) la maggior parte delle analisi teorica era stata sviluppata; di conseguenza, il mio lavoro è incentrato sull'ottimizzazione dei parametri del sistema, tenendo conto delle limitate risorse disponibili in uno scenario realistico. I contributi principali riguardano la progettazione del canale di feedback a rate limitato e algoritmi di scheduling subottimi a bassa complessità, sia per sistemi single carrier che in uno scenario OFDM. In particolare, i contributi riguardanti la progettazione del canale di feedback a

rate limitato traggono vantaggio dalla correlazione temporale del canale, utilizzando sistemi di quantizzazione con memoria. E' stato inoltre proposto un algoritmo di scheduling a bassa complessita', e si sono studiate le prestazioni in confronto con i principali algoritmi presenti in letteratura. Tale confronto evidenzia che a parita' di condizioni, l'algoritmo da noi proposto e' caratterizzato da prestazioni analoghe alle altre soluzioni e molto vicine all'ottimo, sia in termini di throughput che di outage throughput, ma con una minor complessita'. La seconda e più recente parte della tesi affronta l'argomento della stima di segnali vitali, ovvero la respirazione e il battito cardiaco, attraverso un sistema remoto, dove non c'e' contatto tra il sensore ed il target a distanza. Questo argomento e' stato affrontato, in collaborazione con Philips Research, Eindhoven (NL), dove sono stata come Visiting Student da ottobre 2008 a maggio 2009. Ho studiato la tecnologia ultra wide band per il rilevamento remoto dei segni vitali, con il vincolo di rispettare i limiti di potenza imposti dalla legislazione vigente. Lo studio e' stato condotto sia analiticamente, che tramite simulazioni, ed infine attraverso l'allestimento di una demo e la raccolta di risultati sperimentali. In particolare, ho proposto un modello generico per il segnale ricevuto e descritto analiticamente la modulazione che i segnali vitali operano sui principali parametri del segnale ricevuto. Sulla base di questo modello, ho studiato le tecniche di rilevazione del respiro e del cuore periodi di battere; in particolare, ho proposto un metodo di stima del periodo a bassa complessita', che migliora le prestazioni di altre soluzioni proposte in letteratura, sia in termini di errore quadratico medio che di complessita' richiesta. Infine, è stato derivato lo stimatore maximum likelihood (ML), ed è stato verificato che il metodo proposto risulta da un'approssimazione del metodo ML.

Abstract

This PhD thesis collects the main contribution of my research activity, performed during my PhD program. As the title suggests, it is divided into two main parts.

The first part collects the research I performed since the beginning of my PhD on Multiuser multiple input multiple output (MIMO) downlink systems with limited feedback; the topic is part of the wide research work on the fourth generation cellular systems. When I begun my research, on January 2007, most of the theoretical analysis had already been illustrated; therefore, my work focused on optimizing system parameters considering the limited resources available in a realistic scenario. The main contributions are on the design of the low rate feedback channel, and sub-optimal, low complexity scheduling algorithms, both in single carrier and in a orthogonal frequency division multiplexing (OFDM) scenario.

The second, and most recent part of the thesis deals with remote sensing of vital signs, i.e. respiration and heart rate; I have been addressing this topic since October 2008, in cooperation with Philips Research, Eindhoven (NL), where I have been visiting student. We investigated the ultra wide band technology for remote sensing of vital signs. We propose a generic model for the received signal and described how vital sign modulates the main parameters of the received signal. Furthermore, we focused on detection techniques of respiration and heart beating periods; we derived the ML period estimator of a zero mean signal with unknown shape, and we proposed a novel low complexity approximated ML estimator. The proposed methods have application in many areas where only the periodicity is required and the complexity is an important issue. In particular, we applied the proposed algorithms to the remote heart rate estimation problem; both simulation and experimental results indicate that the proposed method outperforms the state of the art methods in detecting the period of a signal with low signal to noise ratio like the heart beating, even with a short observation of the periodic signal.

Though the two parts of research I performed during my PhD program seem to have

little in common, they can be investigated with the same analytical tools, particularly for signal processing and detection techniques.

Part I

Multiuser MIMO Downlink Systems with Limited Feedback

Main Abbreviations and Notation

BF: beamforming;

BFB: basic feedback;

BS: base station;

$\mathcal{C}$: Codebook;

CC: centroid condition;

CLS: complex locations;

CDI: channel direction information;

CMUX: complex multiplications;

CQI: channel quality information;

CSI: channel state information;

CSIT: channel state information at the transmitter side;

CV: channel vector;

DPC: dirty paper coding;

$\mathrm{E}[\cdot]$: expectation operator;

EA: exhaustive algorithm;

FB: feedback signalling;

FDD: frequency division duplexing;

LBG: generalized Linde, Buso, and Gray algorithm;

LTE: long term evolution;

M: number of BS antennas;

MG: multicarrier greedy algorithm;

MIMO: multiple input multiple output;

MMSE: minimum mean square error;

MSE: mean square error;

MSUS: multicarrier semi orthogonal user selection algorithm;

MT: mobile terminal;

MU: multiuser;

NNC: nearest neighborhood condition

OFDM: orthogonal frequency division multiplexing;

PBG: projection based greedy algorithm;

PDF: probability density function;

PFB: predictive feedback;

PFS: proportional fair scheduler;

QEV: quantization of the error vector;

QoS: quality of service;

RB: resource block;

RM: unitary rotation matrix;

RVQ: random vector quantization;

SC: single carrier;

SCM: spatial channel model;

SNIR: signal to noise plus interference ratio;

SPPBG: projection based greedy with simplified preselection algorithm;

SR: sum rate;

SU: single user;

TDD: time division multiplexing

TS: training set;

UD: updown feedback;

WSR: weighted sum rate;

ZF: zero forcing;

Introduction

Next generation wireless cellular systems are expected to support high quality multimedia services; this motivates the interest in multi antenna (MIMO) systems, where both spatial diversity and multiplexing can be used to increase the achievable throughput. In fact, it has been shown that the downlink capacity of a MIMO system with perfect channel state information (CSI) scales as a linear function of the number of transmit antennas [2]. Although non linear dirty paper coding (DPC) scheme achieves the system capacity, it has a high computational cost [3], and simpler solutions have been investigated. Linear beamforming has been shown [4] to achieve a large part of DPC capacity; in particular, zero forcing (ZF) beamforming matched to an opportunistic scheduling is widely used [4].

However, benefits of MIMO are obtained only by a proper scheduling of transmissions, which opportunistically exploits channel conditions in order to increase throughput, while ensuring quality of service (QoS). Several scheduling techniques have been proposed for MIMO single carrier (SC) systems on flat fading channels based on various approaches, including clique search [5], maximization of the Frobenius norm of the composite channel matrix [6, 7], user channel orthogonality [8, 9, 10], single bit feedback [11], waterfilling [12], tree search [13], evolutionary algorithm [14] and greedy scheduling [15] extended to the case of limited feedback in [16]. In some cases, optimization of scheduling and power allocation are performed jointly [5, 6, 7, 11, 12, 14], while in other cases only scheduling is considered [8, 9, 10, 15]. Moreover, QoS oriented multiuser scheduling and beamforming have been investigated in [17], in order to conciliate the request of high throughput with low packet delays. An overview of research on cross layer scheduling for multiuser MIMO SC systems is given in [18]. A similar problem to multiuser MIMO scheduling can be found in other transmission systems, such as multicarrier code-division multiple access [19].

In frequency selective channels, SC modulation is often replaced by orthogonal frequency division multiplexing (OFDM) due to its efficiency in overcoming multipath fading. In fact, the combination of MIMO and OFDM technology is a good candidate for future wireless cellular systems, as it has been proposed for downlink in the long term evolution (LTE) release of 3GPP standard [20, 21]. When MIMO OFDM is considered, scheduling becomes more complex, as the number of resources to be allocated, i.e. the number of subcarriers, increases and only suboptimal approaches are viable [13]. Complexity is further increased in a frequency division duplexing (FDD) system, where CSI is provided to the base station (BS) by each mobile terminal (MT) through a feedback (FB) channel. In fact, due to the limited FB rate, only a partial CSI is available at the BS and additional processing is required to compensate the channel uncertainty. Some of the scheduling techniques considered for SC transmissions can be extended to OFDM. For example, in [22] a scheduling algorithm has been proposed for MIMO OFDM systems which extends the method proposed in [15] for SC systems: the set of scheduled MTs on each subcarrier is built in a greedy fashion, by adding one user at the time with the aim of maximizing a weighted sum rate (WSR). In [23] this approach has been further simplified to avoid the need of computing a new beamforming matrix upon the insertion of a new candidate in the set of scheduled MTs. A further scheduling simplification is achieved by excluding from the selection process MTs that would not contribute to the WSR, by introducing a bound of their signal to noise plus interference ratio [24].

In this first part of the thesis, we propose efficient and low complexity strategies for multiuser MIMO downlink systems. We discuss the main parameters of a MIMO SC downlink systems, i.e. the beamforming, scheduling and feedback signalling. Then we revise the scheduling techniques proposed in the literature for multiuser MIMO OFDM system with limited feedback and compare them both in terms of computational and memory cost and in terms of achieved throughput in a LTE 3GPP scenario.

This part is organized as follows. In Chapter 1 we describe the downlink MIMO SC system; in particular we discuss beamforming techniques and FB strategies. In Chapter 2 we introduce the OFDM MIMO system, and we discuss the scheduling strategies. Experimental results are illustrated in Chapter 3.

In Chapter 4 we derive some conclusion of this first part of the thesis. Notation: bold upper and lower letters denote matrices and vectors, respectively; $(\cdot)^H$ denotes Hermitian operation (transpose complex conjugate), while $(\cdot)^T$ denotes transpose; $\|\cdot\|$ is the vector norm, and $\mathrm{E}[\cdot]$ stands for expectation trace.

Chapter 1

Multiuser MIMO SC Downlink System

In multiuser MIMO downlink systems the BS requires channel knowledge to achieve spatial multiplexing across users. While in time division duplexing (TDD) systems CSIT can be acquired from channel estimation in the uplink, in FDD systems CSIT can be obtained only by setting up an explicit FB channel from each user. Since the number of bits required to describe the channels grows as the product of the number of transmit and receive antennas, the channel delay spread and the number of users [25], only by a proper optimization of the FB signalling its impact on the network throughput can be limited. In fact, if a reliable CSIT provides an higher system throughput, on the other hand a low FB rate is necessary to guarantee an high payload.

The tradeoff between CSI quality and FB rate has been recently addressed and various aspects have been investigated including transmitter and receiver design [26], [27], [28] and feedback optimization in both single user (SU) and multiuser (MU) systems [29], [30], [31] [32].

FB bits are mostly used to index a set of vectors (or codewords) in a codebook $\mathcal{C}$ which is known to the transmitter and all receivers. For example, b bits per feedback interval can be used to index a codebook with 2^b vectors. For a transmitter, each codeword in $\mathcal{C}$ is a multi-dimensional vector that characterizes the MIMO channel for that user or more generally provides information on the reconstruction of the user's channel. A well-designed codebook will contain codewords that effectively span the set of MIMO channels experienced by the users [30], [31].

In SU systems it has been shown that only a few FB bits (roughly on the order of transmit antennas) are needed to achieve near perfect-CSIT performance. On the other hand, in downlink channels accurate channel knowledge is essential to avoid multiuser interference and a severe degradation of the achievable throughput [26]. An opportunistic user selection approach can increase the performance of this system, leading to asymptotically optimum performance when the number of users goes to infinity [29],[26],[28] . In [16, 33] the codebook is a set of vectors randomly chosen from an isotropic distribution on the unit hypersphere, in a space having the dimension of the number of BS antennas. This technique is called random vector quantization (RVQ).

In this chapter we focus on single-antenna mobile terminals and SC scenario; in particular, we investigate the beamformer design for a opportunistic downlink MIMO system, i.e. the transmission from the BS to a group of MTs, selected by the BS, using the multiplexing properties of the MIMO system. The term opportunistic underlines that the BS policy of user selection favors the MT with a good channel quality.

In Section 1.2, we revise ZF beamforming and propose a new minimum mean square error (MMSE) beamformer under incomplete CSIT that takes into account the quantization error of the channel vector [34]. As shown in [35] under perfect CSIT, MMSE BF shows significant performance improvements in case of randomly selected users but gives reduced gains with respect to ZF BF in case of opportunistic user selection. In the second part of the chapter, we propose various channel quantization techniques and FB strategies based on the Lloyd-Max algorithm [36] that exploit both spatial and time correlation of the MIMO channel. In particular in Subsection 1.4.2 we derive a Up-or-Down (UD) FB approach where FB bits are accumulated over multiple signalling intervals in order to index a much larger codebook; this technique has been proposed in [37], and then it has been extended to the multi antenna receiver scenario with the name of hierarchical FB (HFB), e.g. [38, 39].

Moreover we propose new predictive FB strategies where both BS and MTs predict the evolution of the channel vector and users adjusts the prediction by feeding back a quantized version of the prediction error to the BS [37, 34]. Finally, we describe a predictive FB strategy with unitary rotation matrix, exploiting the geometric properties of unit norm CDI vectors; a similar technique has been proposed in [40] for a single user MIMO scenario, and it is here generalized to the multiuser scenario. In Section 1.3 a general quantization scheme is described: the generalized Linde, Buso, and Gray (LBG) algorithm is described in Section 1.3.1, and used for codebook design in Subsection 1.3.2; finally, the quantization process is described. In Section 1.4 we introduce four different FB strategies: i) Basic Feedback (BFB), ii) UpDown Feedback (UD), iii) Predictive Feedback with quantization of the error vector (QEV), and iv) Predictive Feedback with Unitary Rotation Matrix (RM). A numerical comparison of the proposed strategies is given in Chapter 3.

1.1 System Model

We consider the downlink of a cellular system where a BS has M transmit antennas and K MTs have one antenna each. The symbol period is denoted as T_s, transmission is performed in time slots of duration T and in each time slot MTs feed back a partial CSI, which is used by the BS to schedule downlink transmissions.

For slot n, let $\mathcal{S}(n)$ be the set of MTs scheduled for downlink transmissions, l_s a natural number, and $\mathbf{d}(t)$ and $\mathbf{y}(t)$ be the column vectors of transmitted and received signals at time $t = l_s T_s$, respectively. We consider a flat fading channel described by the complex $|\mathcal{S}(n)| \times M$ matrix $\mathbf{H}(t) = [\mathbf{h}_1(t), \ldots, \mathbf{h}_{|\mathcal{S}(n)|}(t)]^T$.

The discrete-time complex baseband model is given by

$$\mathbf{y}(t) = \mathbf{H}(t)\mathbf{d}(t) + \mathbf{n}(t)\,, \tag{1.1}$$

where $\mathbf{n}(t)$ is a complex Gaussian vector noise with i.i.d. components having zero mean and unit variance.

The transmit signal is subject to the average power constraint

$$\mathrm{E}\left[\|\mathbf{d}(t)\|^2\right] \leq P\ , \tag{1.2}$$

where P is the available power. From (1.2) and noise assumptions, the average system signal to noise ratio at the receiver is $SNR = P$.

The channel matrix $\mathbf{H}(t)$ is not perfectly known at the BS while we assume that MT k perfectly estimates the channel vector $\mathbf{h}_k(t)$ once a slot. As in [33, 16] we adopt a double FB information and each MT feeds back $i)$ a channel direction information (CDI) of the direction of channel vector (CV) at each slot, namely

$$\tilde{\mathbf{h}}_k(n) = \frac{\mathbf{h}_k(nT)}{||\mathbf{h}_k(nT)||} \tag{1.3}$$

and $ii)$ a channel quality information (CQI), evaluated as

$$\xi_k \triangleq \frac{||\mathbf{h}_k||^2 |\tilde{\mathbf{h}}_k^H \bar{\mathbf{h}}_k|^2}{1 + \frac{P}{M}||\mathbf{h}_k||^2 (1 - |\tilde{\mathbf{h}}_k^H \bar{\mathbf{h}}_k|^2)}\,, \tag{1.4}$$

where $\bar{\mathbf{h}}_k$ is the unit-norm *reconstructed* CVs of MT k. We focus here on the quantization and FB of the CDI. We assume that the FB channel has a finite rate of b bits per slot and allows zero-delay error free transmissions.

The BS stores the partial CSI of selected users into the matrix $\bar{\mathbf{H}}(\mathcal{S}(n)) = [\bar{\mathbf{h}}_{s_1}(n), \ldots, \bar{\mathbf{h}}_{s_{|\mathcal{S}(n)|}}(n)]^T$, with $s_i \in \mathcal{S}(n)$, containing the unit-norm *reconstructed* CVs. Based on the partial CSI, the BS evaluates the $M \times |\mathcal{S}(n)|$ complex beamforming matrix $\mathbf{G}(\mathcal{S}(n)) = \left[\mathbf{g}_1, \ldots, \mathbf{g}_{|\mathcal{S}(n)|}\right]$, and vector $\mathbf{p}$ enforcing the power constraint (1.2), i.e. [16]

$$\mathbf{p} = \frac{P}{|\mathcal{S}(n)\mathbf{g}_k(n)|}. \tag{1.5}$$

Once MTs have been selected for downlink transmission, the transmitted vector $\mathbf{d}(t)$ is obtained by beamforming, i.e.,

$$\boldsymbol{d}(t) = \mathbf{G} \quad \operatorname{diag}(\mathbf{p})^{1/2}\big(\mathcal{S}(n)\big)\mathbf{u}(t) \quad nT \leq t < (n+1)T\,, \tag{1.6}$$

where vector $\mathbf{u}(t) = [u_1(t), \ldots, u_{|\mathcal{S}(n)|}(t)]^T$ contains the MT data symbols for time slot n, which are assumed independent and identically distributed (i.i.d.) with zero mean and unit variance. The MT k signal to noise ratio (SNIR) is given by

$$SNIR_k(t) = \frac{p_k|\mathbf{h}_k(t)\mathbf{g}_k(n)|^2}{1 + \sum_{i \in \mathcal{S}(n)\backslash k} p_i|\mathbf{h}_k(t)\mathbf{g}_i(n)|^2}. \tag{1.7}$$

1.2 Beamformer Design

In this section we briefly review the ZF-BF design and derive a new MMSE-BF under incomplete CSI assumptions. For ease of notation we drop both the slot (n) and the time (t) index.

1.2.1 Zero-Forcing Beamforming

The ZF approach aims at nulling the interference at the MTs and the corresponding transmit matrix is the normalized version of the right pseudo-inverse of $\bar{\mathbf{H}}$. According to ZF-BF, the beamformer can be written as

$$\mathbf{G}^{(ZF)}(\mathcal{S}) = \bar{\mathbf{H}}(\mathcal{S})^H \left(\bar{\mathbf{H}}(\mathcal{S})\bar{\mathbf{H}}(\mathcal{S})^H\right)^{-1}., \tag{1.8}$$

Provided that each MT feeds back to the BS its current CQI value, an estimate of the SNIR for MT k has been derived in [16] as

$$\gamma_k^{(ZF)} = \xi_k p_k \,, \tag{1.9}$$

under the following assumptions: *a*) CV with i.i.d. components, each Rayleigh fading, *b*) equal power distribution among signals transmitted to MTs, *c*) $|\mathcal{S}| = M$.

1.2.2 MMSE Beamforming

The MMSE beamformer aims at minimizing the sum mean square error (MSE) of the received signals. To this end, we first decompose the CV relative to MT k into two orthogonal vectors $\mathbf{f}_k$ and $\boldsymbol{\epsilon}_k$, parallel and orthogonal to $\bar{\mathbf{h}}_k$, respectively, with

$$\mathbf{h}_k = ||\mathbf{h}_k|| \left(\mathbf{f}_k + \boldsymbol{\epsilon}_k\right) \,, \tag{1.10}$$

where $\mathbf{f}_k = \cos\Theta_k \bar{\mathbf{h}}_k$ and $\cos\Theta_k = |\tilde{\mathbf{h}}_k^H \bar{\mathbf{h}}_k|$. Let also define $\mathbf{F} = [\mathbf{f}_1, \ldots, \mathbf{f}_{|\mathcal{S}|}]^T$ and $\boldsymbol{E} = [\boldsymbol{\epsilon}_1, \ldots, \boldsymbol{\epsilon}_{|\mathcal{S}|}]^T$. We assume that MT k divides the received signal by $\beta||\mathbf{h}_k||$, where β is a power normalization coefficient. In this case, by defining the matrix $\mathbf{N} = \mathrm{diag}\left(||\mathbf{h}_1||, \ldots, ||\mathbf{h}_{|\mathcal{S}|}||\right)$, the normalized received signal can be written as

$$\mathbf{y}' = \beta^{-1}\left(\mathbf{F} + \boldsymbol{E}\right)\mathbf{G}(\mathcal{S})\mathbf{u} + \beta^{-1}\mathbf{N}^{-1}\mathbf{n} \,. \tag{1.11}$$

The MMSE-BF design aims at jointly optimizing $\mathbf{G}(\mathcal{S})$ and β in order to minimize the MSE, i.e.,

$$\mathbf{G}^{(MMSE)}(\mathcal{S}) = \underset{\mathbf{G}(\mathcal{S}),\beta}{\arg\min} \mathrm{E}\left[\left|\left|\mathbf{y}' - \mathbf{u}\right|\right|^2\right] \tag{1.12}$$

under the power constraint (1.2), without imposing equal power allocation among MTs. The expectation in (1.12) is taken with respect to data, noise and the direction of the error vectors $\boldsymbol{\epsilon}_k$, while from (1.10) we observe that $||\boldsymbol{\epsilon}_k||^2 = \sin^2(\Theta_k)$.

The constrained minimization is solved by the Lagrangian multipliers. We assume that $\boldsymbol{\epsilon}_k$ are statistically uncorrelated and that the unit-norm vector $\tilde{\boldsymbol{\epsilon}}_k = \boldsymbol{\epsilon}_k/||\boldsymbol{\epsilon}_k||$ assumes all directions orthogonal to $\bar{\mathbf{h}}_k$ with equal probability.

We derive here $\mathrm{E}\left[\tilde{\boldsymbol{\epsilon}}_k \tilde{\boldsymbol{\epsilon}}_k^H\right]$ under the hypothesis: a) $\bar{\mathbf{h}}_k^H \tilde{\boldsymbol{\epsilon}}_k = 0$; b) $\tilde{\boldsymbol{\epsilon}}_k^H \tilde{\boldsymbol{\epsilon}}_k = 1$; c) $\bar{\mathbf{h}}_k^H \bar{\mathbf{h}}_k = 1$; d) all direction of $\tilde{\boldsymbol{\epsilon}}_k$ in the space orthogonal to $\bar{\mathbf{h}}_k$ are equally probable.

From vector $\bar{\boldsymbol{h}}_k$, by the orthonormalization procedure of Gram-Schmidt, we obtain a $N \times N-1$ orthonormal matrix $\boldsymbol{A}$, such that $\bar{\mathbf{h}}_k^H \boldsymbol{A}_k = \mathbf{0}$ and $\tilde{\boldsymbol{\epsilon}}_k = \boldsymbol{A}_k \boldsymbol{x}_k$, with $\boldsymbol{x}_k$ a $N-1$-size unit-norm vector. We also have

$$\mathrm{E}[\tilde{\boldsymbol{\epsilon}}_k \tilde{\boldsymbol{\epsilon}}_k^H] = \boldsymbol{A}_k \mathrm{E}[\boldsymbol{x}_k \boldsymbol{x}_k^H] \boldsymbol{A}_k^H \,. \tag{1.13}$$

Then, we can write $[\boldsymbol{x}_k]_q = |\,[\boldsymbol{x}_k]_q\,|e^{j\varphi_{k,q}}$. We assume that $\varphi_{k,q}$ are i.i.d. uniform random variables in $(0, 2\pi]$, while $[|\boldsymbol{x}_k|]_i$ are i.i.d. zero mean variables, so that

$$\mathrm{E}[x_p x_q^*] = \begin{cases} 0 & p \neq q \\ \mathrm{E}[|[\boldsymbol{x}_k]_p|^2] & p = q\,. \end{cases} \tag{1.14}$$

We now write $\boldsymbol{x}_k$ in hyper spherical coordinates as

$$|[\boldsymbol{x}_k]_i| = \cos(\phi_i)\prod_{p=1}^{i-1}\sin(\phi_p)\,, \quad i = 1, 2, \ldots, N-2\,,$$

$$|[\boldsymbol{x}_k]_{N-1}| = \prod_{p=1}^{N-2}\sin(\phi_p)\,,$$

where ϕ_i, $i = 1, 2, \ldots, N-2$ are independent uniform random variables in the range $(0, 2\pi]$. Hence we obtain $\mathrm{E}[|[\boldsymbol{x}_k]_p|^2] = \frac{1}{2^p}$, $p < N-1$ and $\mathrm{E}[|[\boldsymbol{x}_k]_p|^2] = \frac{1}{2^{N-2}}$.

Lastly, by defining $\mathbf{R} = \mathrm{E}[\boldsymbol{E}^H\boldsymbol{E}]$, from the assumption that all vectors $\boldsymbol{\epsilon}_k$ are independent, from (1.17) we obtain

$$\mathbf{R} = \mathrm{E}[\boldsymbol{E}^H\boldsymbol{E}] = \sum_{k=1}^{|\mathcal{S}|}\sin^2(\Theta_k)\boldsymbol{A}_k^*\Xi\boldsymbol{A}_k^T\,, \tag{1.15}$$

where Ξ is a diagonal matrix with entries

$$[\Xi]_{p,p} = \frac{1}{2^p}\,, \quad p < N-1\,, \quad [\Xi]_{N-1,N-1} = \frac{1}{2^{N-2}}\,, \tag{1.16}$$

$\boldsymbol{A}_k$ is an $N \times (N-1)$ matrix having as columns a base of the space orthogonal to $\bar{\boldsymbol{h}}_k$; from (1.13) and (1.14) we obtain also

$$\mathrm{E}[\tilde{\boldsymbol{\epsilon}}_k^*\tilde{\boldsymbol{\epsilon}}_k^T] = \boldsymbol{A}_k^*\Xi\boldsymbol{A}_k^T\,. \tag{1.17}$$

Then, by defining the normalized matrix

$$\bar{\mathbf{G}} = \left[\mathbf{F}^H\mathbf{F} + \mathbf{R} + \frac{\sigma_N^2}{P}\mathbf{I}\right]^{-1}\mathbf{F}^H \tag{1.18}$$

where $\sigma_N^2 = \sum_{i\in\mathcal{S}}\frac{1}{\|\boldsymbol{h}_i\|^2}$, and

$$\beta = \sqrt{\frac{P}{\mathrm{trace}\left(\bar{\mathbf{G}}^H\bar{\mathbf{G}}\right)}} \tag{1.19}$$

we obtain

$$\mathbf{G}^{(MMSE)} = \beta\bar{\mathbf{G}}\,. \tag{1.20}$$

The SNIR relative to MT k can be written as

$$\mathrm{SNIR}_k = \frac{||\mathbf{h}_k||^2| \left(\bar{\mathbf{h}}_k^T \cos\Theta_k + \tilde{\boldsymbol{\epsilon}}_k^T \sin\Theta_k\right) \mathbf{g}_k|^2}{1 + ||\mathbf{h}_k||^2 \sum_{i\neq k} | \left(\bar{\mathbf{h}}_k^T \cos\Theta_k + \tilde{\boldsymbol{\epsilon}}_k^T \sin\Theta_k\right) \mathbf{g}_i|^2} \,. \tag{1.21}$$

Neglecting the second term in the numerator of (1.21), i.e., $\boldsymbol{\epsilon}_k^T \mathbf{g}_k \simeq 0$, and taking the expectation with respect to the interference term in the denominator of (1.21), we obtain the SNIR estimate

$$\gamma_k^{(MMSE)} = \frac{||\mathbf{h}_k||^2 \cos^2\Theta_k |\bar{\mathbf{h}}_k^T \mathbf{g}_k|^2}{1 + ||\mathbf{h}_k||^2 \cos^2\Theta_k \sum_{i\neq k} |\bar{\mathbf{h}}_k^T \mathbf{g}_i|^2 + ||\mathbf{h}_k||^2 \sin^2\Theta_k \sum_{i\neq k} \mathbf{g}_i^H \mathrm{E}\left[\tilde{\boldsymbol{\epsilon}}_k^* \tilde{\boldsymbol{\epsilon}}_k^T\right] \mathbf{g}_i} \tag{1.22}$$

Note that for the MMSE-BF design, the BS must know two CQIs beyond CDI: a) the channel norm $||\mathbf{h}_k||$ and b) the correlation $\cos\Theta_k$.

1.3 FB Codebook Design

We introduce in this Section the LBG quantization strategy, proposed in [37]. In particular, in Subsection 1.3.1 we introduce the generalized LBG algorithm [41] as a practical algorithm for the codebook design when the probability density function (PDF) is unknown. Based on LBG, the codebook design strategy is then described in 1.3.2

1.3.1 Generalized Quantization LBG Algorithm

We first recall here the generalized Lloyd algorithm for vector quantization. Let $d(\mathbf{s}, \mathbf{c}_i)$ be a distortion metric where $\mathbf{s} \in \mathbb{C}^M$ is the source vector and $\mathbf{c}_i \in \mathbb{C}^M$ is a generic codeword of codebook $\mathcal{C}$. The generalized Lloyd algorithm [42], generates the optimum codebook that minimizes the average distortion,

$$\min_{\mathcal{Q}[\cdot]} \mathrm{E}\left[d(\mathbf{s}, \mathbf{c}_n)\right] \tag{1.23}$$

where $\mathbf{c}_n = \mathcal{Q}[\tilde{\mathbf{s}}]$ is the quantized vector at minimum distortion.

The algorithm comprises two steps:

- Nearest neighborhood condition (NNC). Given a codebook $\mathcal{C} = \{\mathbf{c}_1, \ldots, \mathbf{c}_N\}$, the optimum partition region (Voronoi cell) $\mathcal{R}_i$, $i = 1, \ldots, N$ of the codevector indexed by i satisfies

$$\mathcal{R}_i = \{\mathbf{s} \,:\, d(\mathbf{s}, \mathbf{c}_i) \geq d(\mathbf{s}, \mathbf{c}_\ell)\,, \forall \ell \neq i\}\ . \tag{1.24}$$

- Centroid condition (CC). For given regions $\{\mathcal{R}_i,\, i = 1, \ldots N\}$, the optimum quantization code-vectors $\mathbf{c}_i$ satisfy

$$\mathbf{c}_i = \underset{\mathbf{c}_\ell \in \mathbb{C}^M}{\arg\min}\ \mathrm{E}\big[d(\mathbf{s}, \mathbf{c}_\ell)\big|\ \mathbf{s} \in \mathcal{R}_i\big] \tag{1.25}$$

for $i = 1, \ldots, N$.

These two steps are iterated until the distortion minimization criterion converges. In particular, we adopt the alternative approach led by Linde, Buso, and Gray (LBG), which considers a large set of vector realizations $\{\mathbf{s}_n\}$ referred as training sequence and replace the statistical expectation $\mathrm{E}\big[d(\mathbf{s}, \mathbf{c}_i)\big|\ \mathbf{s} \in \mathcal{R}_i\big]$ by the sample average $\frac{1}{m_i} \sum\limits_{\mathbf{s}_n \in R_i} d(\mathbf{s}_n, \mathbf{c}_i)$, where m_i is the number of elements of training sequence inside $\mathcal{R}_i$. We recall that the LBG algorithm converges to a minimum that is not guaranteed to be global, nevertheless it provides a practical way for codebook design even when the PDF of the source signal is not known or difficult to characterize.

1.3.2 Codebook Design

For the scenario of CDI FB that we are considering, since system performance is measured in terms of the achievable sum rate, a criterion of the codebook design is the maximization of the estimated SNIR. For a ZF beamforming, maximization of the estimated SNIR is equivalent to the maximization of the average correlation (1.28), since it provides simultaneously the maximization of the numerator and minimization of the denominator of (1.9). For a MMSE beamforming scenario, the maximization of the average correlation (1.28) provides the maximization of the numerator of the estimated SNIR 1.22. Therefore, in both cases the criterion of the codebook design is

$$\max_{\mathcal{C}} \mathrm{E}\left[|\tilde{\mathbf{h}}_k^T \mathbf{c}_n^*|^2\right] \tag{1.26}$$

where $\mathbf{c}$ is the unit norm code vector from the codebook $\mathcal{C}$ at minimum *chordal distance* from the channel direction $\tilde{\mathbf{h}}_k$.

The generalized Lloyd algorithm [42] can be used to generate the optimum codebook according to (1.26), which can be implemented by the LBG approach [43], where the expectation is evaluated as the average on a finite training set (TS) of CVs, randomly chosen according to the channel statistics.

We consider a variant of the LBG algorithm that proceeds iteratively by levels in the codebook design, according to the following steps:

1. From the TS, compute the optimum codebook with two codevectors by the LBG algorithm;
2. Split the TS into two subsets, where each subset collects all the CVs of the TS at minimum chordal distance from the corresponding codevectors;
3. Recursively iterate steps 1) and 2) to each of the subsets of TS.

This binary construction procedure can be represented by a binary tree of B levels, having at level i the codewords of the optimal codebook with 2^i elements.

With the designed codebook, quantization can be performed with a binary search on the tree, thus requiring a lower computation complexity than conventional quantization, at the expense of a larger memory.

A binary representation (codeword) of each codevector is obtained by associating a bit to each of the two branches exiting a node and identifying a node at level i with the i bits on the branches leading from the root. As a consequence, all nodes of the subtree departing from a node at level i have the same i most significant bits. The codeword of $i+1$ bits associated to a CV can be obtained by adding one bit to the CV representation with i bits.

Moreover, slight changes of the channel in subsequent time slots most probably lead to codewords with the same most significant bits. This feature is the key aspect in the UD signaling.

1.3.3 Quantization

MT k quantizes the normalized CV $\tilde{\mathbf{h}}_k$ into a codevector $\hat{\mathbf{c}}_k$, whose index of b bits is fed back at each slot. $\hat{\mathbf{c}}_k$ is selected from a codebook of unit norm codevectors

$$\mathcal{C} = \{\mathbf{c}_1, \ldots, \mathbf{c}_N\} \tag{1.27}$$

with $N = 2^b$. The quantization criterion is the minimum *chordal distance* (see e.g. [44] for a general definition), i.e

$$\hat{\mathbf{h}}_k = \underset{\{\mathbf{c}\in\mathcal{C}\}_{n=1,\ldots,N}}{\arg\max} |\tilde{\mathbf{h}}_k^T \mathbf{c}^*| \, . \tag{1.28}$$

1.4 FB Signalling Design

In this Section we investigate different techniques for FB signalling. Firstly, we introduce the basic technique, which consists on transmitting the quantized version of the actual CV. Then, we propose different FB strategies exploiting the channel correlation in time domain, and in particular: the UD FB approach where FB bits are accumulated over multiple signalling intervals in order to index a much larger codebook; predictive FB strategies where both transmitter and users predict the evolution of the channel vector and users feed back a quantized version of the prediction error to the transmitter; a predictive FB strategy with unitary rotation matrix, exploiting the geometric properties of unit norm CDI vectors.

1.4.1 Basic FB

The simplest FB signalling can be performed by quantizing and transmitting directly the CDI; in other words, MT k quantizes $\tilde{\mathbf{h}}_k$ to a unit norm vector $\hat{\mathbf{h}}_k$ and selects as codeword $\hat{\mathbf{c}}_k = \hat{\mathbf{h}}_k$; the codebook index corresponding to $\hat{\mathbf{c}}_k$ is then sent to the BS. We denote this signaling technique as basic FB (BFB). In BFB, the correlation in time of the MIMO channel is not exploited, and the FB signalling is redundant. In fact, if the channel is changing sufficiently slowly, and assuming that the codebook complies with the nearest neighbor condition, described in Section 1.3.1, the FB signalling of MT k in two adjacent slots differs only of few bits. Based on these considerations we propose different FB strategies, where the mobile CDI FB are aggregated over multiple FB intervals so that the aggregated bits index a larger codebook. By aggregating the FB bits over multiple intervals, the codewords can indicate a variation w.r.t. the past CDIs.

1.4.2 UD FB Signaling

The Up-or-Down (UD) FB signalling technique is based on the tree description of the vector quantizer and an incremental FB strategy, exploiting the channel correlation in time domain.

We assume that at slot $n-1$, both BS and MT k share the reproduced CV $\bar{\mathbf{h}}_k(n-1)$, represented by a binary word of variable length $L_s(n-1)$.

At slot n, MT k quantizes $\tilde{\mathbf{h}}_k(n)$ into $\hat{\mathbf{h}}_k(n)$ and compare the first $L_s(n-1)$ bits of the binary representations of $\hat{\mathbf{h}}_k(n)$ and $\bar{\mathbf{h}}_k(n-1)$. The comparison leads to two cases, corresponding to a match (*Down case*) or no match (*Up Case*) between the two sequences. Let $\mathbf{i}_k(n)$ be the binary word of b bits fed back by MT k at time slot n. The first bit $i_{k,1}(n)$ denotes the Up or Down case. The following bits are determined as follows:

- *Down Case.* The CSI is refined by feeding back further $b-1$ bits of the B-bits code word. These additional bits are obtained by going down by $b-1$ levels into the quantization tree. This is performed by feeding back bits at position $L_s(n-1)+1, \dots, L_s(n-1)+b-1$ of the codeword associated to $\hat{\mathbf{h}}_k(n)$. Moreover, $L_s(n) = L_s(n-1)+b-1$.

- *Up Case.* The CSI must be updated and the $b-1$ bits $L_s(n-1)-2(b-1)+1, \dots, L_s(n-1)-b+1$ of the codeword associated to $\hat{\mathbf{h}}_k(n)$ are fed back to BS. Now, $L_s(n) = L_s(n-1)-b+1$.

The proposed algorithm can be easily generalized to account for boundary conditions imposing that $b-1 \leq L_s(n) < B$. Thanks to this strategy we are able to track channel variations at the cost of an overhead of one flag bit. In this case, the transmitted binary word $\mathbf{i}_k(n)$ has not a single relation to $\hat{\mathbf{c}}_k(n)$, because it has been derived from $\hat{\mathbf{h}}_k(n)$ and $\bar{\mathbf{h}}_k(n-1)$.

1.4.3 Predictive FB (PFB)

The predictive FB (PFB) strategy is based on predictive vector quantization [45].

As depicted in Fig. 1.1, at slot n, both BS and MT obtain a prediction $\mathbf{h}_k^{(p)}(n)$ of the CV direction $\tilde{\mathbf{h}}_k(n)$, based on past reproduced values $\{\bar{\mathbf{h}}_k(m)\,,\, m < n\}$. For example, a simple first order linear predictor yields $\mathbf{h}_k^{(p)}(n) = \bar{\mathbf{h}}_k(n-1)$ where only the previous CSI value is used for prediction. Next, each MT quantizes the prediction error $\mathbf{e}_k(n) = \tilde{\mathbf{h}}_k(n) - \mathbf{h}_k^{(p)}(n)$ and feeds back to BS $\mathbf{i}_k(n)$, a binary representation of the quantized vector error $\hat{\mathbf{e}}_k(n)$ using b bits. Both BS and MT update the reproduced CV $\bar{\mathbf{h}}_k(n)$ by combining the predicted vector with the quantized prediction error, i.e.,

$$\bar{\mathbf{h}}_k(n) = \frac{\mathbf{h}_k^{(p)}(n) + \hat{\mathbf{e}}_k(n)}{||\mathbf{h}_k^{(p)}(n) + \hat{\mathbf{e}}_k(n)||}\,, \tag{1.29}$$

denoted as $+/||.||$ in Fig. 1.1.

In this case, the codebook of the prediction error quantizer is designed by the LBG algorithm minimizing the MSE $\mathrm{E}[||\mathbf{e}_k - \mathbf{c}_i||^2]$. We follow the open loop approach, hence from a TS we first obtain the set of channel predictions and channel prediction errors $\{\mathbf{e}_k(n)\}$, which are then used to design of the codebook by the LBG algorithm.

1.4.4 Unitary Rotation Matrix Predictive FB (RM)

We propose a further FB technique based on the quantization of the prediction error. In particular, since $\mathbf{h}_k^{(p)}(n)$ and $\tilde{\mathbf{h}}_k(n)$ are unit-norm vectors, we model the prediction error as a rotation vector from the predicted vector $\mathbf{h}_k^{(p)}(n)$ to the true normalized CV $\tilde{\mathbf{h}}_k(n)$.

In details, at slot n both MT k and BS derive in the complex hyperspace $\mathbb{C}^{M\times 1}$ of the MIMO channel a unitary basis whose first element is given by the predicted vector $\mathbf{h}_k^{(p)}(n)$. This is done by computing the unitary $M\times M$ matrix $\mathbf{W}_k(n)$ obtained by the Gram-Schmidt orthogonalization procedure [36] applied to the columns of $[\mathbf{h}_k^{(p)}(n)\ \mathbf{I}_M]$, where $\mathbf{I}_M$ is the $M \times M$ identity matrix. With this definition the components of $\mathbf{h}_k^{(p)}(n)$ in the new basis are the constant vector $\mathbf{u} = \mathbf{W}_k(n)^H\mathbf{h}_k^{(p)}(n) = [1\,0\,\ldots\,0]^T$, while the prediction error vector is defined as

$$\mathbf{e}_k(n) = \mathbf{W}_k^H(n)\tilde{\mathbf{h}}_k(n)\,. \tag{1.30}$$

Let $\hat{\mathbf{e}}_k(n)$ be the quantized version of $\mathbf{e}_k(n)$ fed back to the BS. The reconstructed vector is defined as

$$\bar{\mathbf{h}}_k(n) = \mathbf{W}_k(n)\hat{\mathbf{e}}_k(n)\,. \tag{1.31}$$

We note that $\mathbf{e}_k(n)$ is expected to lie with high probability in an hyper-cone centered around the constant vector $\mathbf{u} = [1, 0, \ldots, 0]^T$ and whose surface area, although depending on channel time correlation, is usually much smaller than the complete surface area of the unitary hyper-sphere described by $\tilde{\mathbf{h}}_k(n)$. This suggests that for a target quantization distortion we need fewer codewords to quantize the prediction error $\mathbf{e}_k(n)$ than what we would need to quantize $\tilde{\mathbf{h}}_k(n)$ as in RVQ [33] or Grassmannian line packing [30].

For codebook design we use the LBG algorithm minimizing the average distance

$$\min_{\mathcal{C}} \frac{1}{N_{TS}} \sum_{i=1}^{2^b} \sum_{\tilde{\mathbf{h}}(n)\in\mathcal{R}_i} d(\mathbf{c}_i, \tilde{\mathbf{h}}(n))\,, \tag{1.32}$$

where $\mathcal{C} = \{\mathbf{c}_1, \mathbf{c}_2, \ldots, \mathbf{c}_{N_c}\}$, $N_c = 2^b$, is the generic codebook and $\mathcal{R}_i$ is the partition region of the training set associated to codeword $\mathbf{c}_i$.

From (1.23) and (1.31) the distance to be minimized is given by

$$\begin{aligned} d(\mathbf{c}, \tilde{\mathbf{h}}(n)) &= 1 - \left|\tilde{\mathbf{h}}^H(n)\mathbf{W}(n)\mathbf{c}\right|^2 \\ &= 1 - \mathbf{c}^H\mathbf{W}^H(n)\tilde{\mathbf{h}}(n)\tilde{\mathbf{h}}^H(n)\mathbf{W}(n)\mathbf{c}\ . \end{aligned} \tag{1.33}$$

We follow the open loop approach, hence from a sequence of channel vectors $\{\tilde{\mathbf{h}}(n)\}$ we derive the set of channel predictions $\{\boldsymbol{h}^{(p)}(n)\}$, which are used to compute $\{\mathbf{W}(n)\}$ in (1.33).

We notice that if we define the $M \times M$ complex matrix relative to the partition region $\mathcal{R}_i$ of the training set

$$\mathbf{A}_i = \sum_{\tilde{\mathbf{h}}(n) \in \mathcal{R}_i} \mathbf{W}^H(n) \tilde{\mathbf{h}}(n) \tilde{\mathbf{h}}^H(n) \mathbf{W}(n), \tag{1.34}$$

from (1.23) and (1.33) we have that the optimum codeword for the partition region $\mathcal{R}_i$ is the dominant eigenvector of matrix $\mathbf{A}_i$ normalized to unit norm.

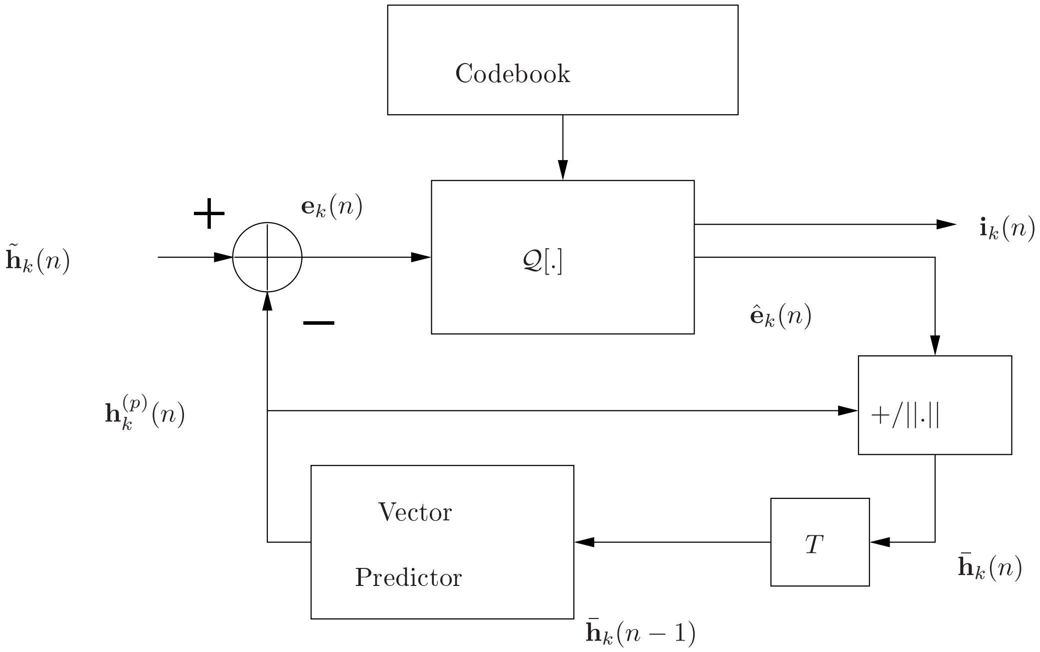

Mobile Terminal

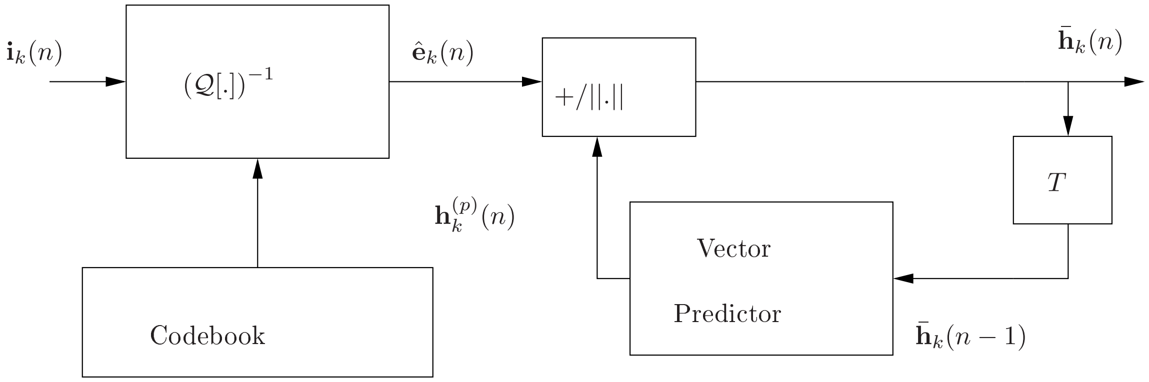

Base Station

Figure 1.1: Predictive FB (PFB).

Chapter 2

Multiuser MIMO OFDM Downlink Systems

MIMO and OFDM are known to provide higher network throughput for the broadcast (downlink) channel, provided that transmissions are suitably scheduled. However, scheduling techniques proposed in Chapter 1 for MIMO SC systems [18, 17], are exceedingly complex when used for OFDM systems, as the number of resources to be allocated increases significantly [13]. Complexity is further increased in FDD systems, where a quantized version of the CSI is provided to the base station by each MT through a FB channel. Among existing efficient solutions we mention the iterative user selection greedy algorithm, proposed for SC systems [15], which requires the computation of a beamforming matrix at each iteration. We propose suboptimal scheduling algorithms, based on simplified BF evaluation during the user selection process. In Section 2.1 the OFDM MIMO downlink system model is illustrated. Section 2.2 addresses the tradeoff between an opportunistic approach in user selection, providing high average sum rate, and quality of service (QoS) requirements: we introduce a general multiuser scheduling, the opportunistic maximum sum rate strategy, and the multicarrier proportional fair scheduling. In Section 2.3 the SC greedy approach is extended and refined. Three user selection strategies are illustrated: i) multicarrier greedy (MG), obtained by extending the SC greedy algorithm; ii) projection based greedy algorithm (PBG), a refined greedy algorithm which requires a lower complexity, and iii) multicarrier semi orthogonal user selection (MSUS). A further refinement of PBG algorithm which performs user selection on a subset of candidate users based on the CQI, is introduced in Section 2.4. Complexity analysis and memory requirements are evaluated for each user selection strategy in Section

2.5. Part of this work has been published in [22, 23].

2.1 System Model

We consider the downlink of a cellular system based on OFDM [46] with N_C subcarriers. The BS has M transmit antennas while K mobile terminals (MTs) have one antenna each. Transmission is performed in time slots of L OFDM symbols, while FB signalling is performed on a time-frequency structure called resource block (RB), according to LTE. For each time slot, we consider in frequency domain N sets of N_S adjacent subcarrier; the RB is defined as the couple time slot, subcarrier set. For each RB, MTs feed back a partial CSI, which is used by the BS to schedule downlink transmissions. In other words, for each time slot each MT feeds back N partial CSI, instead of $N_C = N \cdot N_S$, and therefore both time and frequency channel correlation are exploited.

At slot n, let $\mathcal{S}_c(n) = \left\{u_{1,c}(n), u_{2,c}(n), \cdots, u_{|\mathcal{S}_c(n)|,c}(n)\right\}$ be the set of $|\mathcal{S}_c(n)|$ MTs, $u_{i,c}(n) \in \{1, \cdots, K\}$, scheduled for downlink transmission on RB $c \in \{1, \cdots, N\}$. We denote as *stream* the (MT,RB) pair (k, c). Let also $\mathcal{P}(n)$ be the set of streams scheduled at slot n, i.e.

$$\mathcal{P}(n) = \{(k, c) \,| k \in \mathcal{S}_c(n), c \in \{1, \cdots, N\}\} . \tag{2.1}$$

In our analysis we model the channel as quasi static, i.e., it is considered invariant for the duration of one OFDM symbol, and it has the same frequency response on all subcarriers of each RB.

Hence, the frequency response of the MIMO channel on RB c of OFDM symbol t for all M transmit antennas and all $|\mathcal{U}_c(n)|$ MTs is described by the complex $|\mathcal{U}_c(n)| \times M$ channel matrix $\mathbf{H}_c(t) = [\mathbf{h}_{1,c}(t), \ldots, \mathbf{h}_{|\mathcal{S}_c(n)|,c}(t)]^T$, where the $M \times 1$ column channel vector (CV) $\mathbf{h}_{k,c}(t)$ collects the gains between the M antennas of BS and stream (k, c).

In general, for OFDM symbol t, $\mathbf{d}_c(t, m)$, and $\mathbf{y}_c(t, m)$ are, respectively, the $M \times 1$ and $|\mathcal{S}_c(n)| \times 1$ column vectors of the transmitted and received signals on subcarrier m of RB c. The discrete-time complex baseband transmission model for subcarrier m of RB c is given by

$$\mathbf{y}_c(t, m) = \mathbf{H}_c(t)\mathbf{d}_c(t, m) + \mathbf{n}_c(t, m) , \quad m = 1, \cdots, N_S, \tag{2.2}$$

where $\mathbf{n}_c(t, m)$ is a $|\mathcal{S}_c(n)| \times 1$ complex Gaussian noise vector with i.i.d. components having zero mean and unit variance. The transmit signal is subject to the average power constraint $\mathrm{E}\left[\sum_{c=1}^{N}\sum_{m=1}^{N_S}\|\mathbf{d}_c(t,m)\|^2\right] \leq P$, where P is the available power. In order to exploit spatial diversity, the transmit signal is obtained from the $|\mathcal{S}_c(n)|\times 1$ data signal $\mathbf{U}_c(t,m)$ by applying the ZF BF matrix $\mathbf{G}_c\big(nL\big)$, i.e.

$$\mathbf{d}_c(t,m) = \mathbf{G}_c\big(nL\big)\mathrm{diag}\{\mathbf{p}_c(nL)\}^{1/2}\mathbf{U}_c(t,m), \quad nL \leq t < (n+1)L\,, \tag{2.3}$$

where $\mathbf{p}_c(nL)$ is the power normalization vector which enforces equal stream power, i.e.

$$P_S = \mathrm{E}\left[\|\ \mathbf{d}_{k,c}(t,m)\ \|^2\right] = \frac{P}{\sum_{c=1}^{N}|\mathcal{S}_c(n)|} \tag{2.4}$$

and $\mathbf{d}_{k,c}(t,m)$ is the kth entry of $\mathbf{d}_c(t,m)$.

2.1.1 FB Information

In a FDD system, CSI is provided through a FB channel; therefore, as in the SC case, we assume that matrix $\mathbf{H}_c(t)$ is not perfectly known at the BS while MT k perfectly estimates the CVs once at each slot, i.e. $t = nL$, to obtain $\mathbf{h}_{k,c}(nL)$, $c = 1, 2, \ldots, N$. As in the SC scenario, described in Chapter 1, we adopt a double FB information for all MT at each slot. In particular, at slot n MT k feeds back for each RB c: *i*) a CDI $\bar{\mathbf{h}}_{k,c}$, which ideally should track the normalized CV $\tilde{\mathbf{h}}_{k,c}(nL)$, namely

$$\tilde{\mathbf{h}}_{k,c}(nL) = \frac{\mathbf{h}_{k,c}(nL)}{||\mathbf{h}_{k,c}(nL)||} \quad c = 1, \ldots, N, \tag{2.5}$$

and *ii*) a CQI, based on the estimated SNIR at the receiver for M orthogonal scheduled users evaluated as [16]

$$\xi_{k,c} \triangleq \frac{||\mathbf{h}_{k,c}(nL)||^2|\tilde{\mathbf{h}}_{k,c}^H(nL)\bar{\mathbf{h}}_{k,c}(nL)|^2}{1 + \frac{P}{M\cdot N}||\mathbf{h}_{k,c}(nL)||^2(1 - |\tilde{\mathbf{h}}_{k,c}^H(nL)\bar{\mathbf{h}}_{k,c}(nL)|^2)}\,. \tag{2.6}$$

We assume that the FB channel has a finite rate of N_b bits per slot and per MT and allows zero-delay error free transmission. The BS builds the matrix

$$\bar{\mathbf{H}}_c(nL) = [\bar{\mathbf{h}}_{u_{1,c}}(nL), \ldots, \bar{\mathbf{h}}_{u_{|\mathcal{S}_c(n)|,c}}(nL)]^T, \quad u_{i,c} \in \mathcal{S}_c(n) \tag{2.7}$$

containing the unit-norm *reconstructed* CVs $\bar{\mathbf{h}}_{k,c}(nL)$. Using the partial CSI, BS evaluates an estimate $\gamma_{k,c}(n)$ of the SNIR of stream (k,c) as will be seen in Section 2.3. ZF beamforming with equal power distribution among streams is implemented for each RB, hence the BF matrix is

$$\mathbf{G}_c^{ZF}(nL) = \bar{\mathbf{H}}_c^H(nL)\left(\bar{\mathbf{H}}_c(nL)\bar{\mathbf{H}}_c^H(nL)\right)^{-1}. \tag{2.8}$$

An estimate of the normalized (with respect to the bandwidth) rate achieved by stream $(k, c) \in \mathcal{P}(n)$ at slot n is

$$R_{k,c}(n, \mathcal{P}(n)) = \log_2(1 + \gamma_{k,c}(n)). \tag{2.9}$$

Notation $R_{k,c}(n, \mathcal{P}(n))$ highlights the fact that rates achieved by different streams are mutually dependent, as *i)* more streams allocated simultaneously on the same RBs yield interference, and *ii)* the total power is distributed among active streams. Performance is evaluated in terms of WSR

$$\mathcal{R}\left(\mathcal{P}(n)\right) = \sum_{(k,c)\in\mathcal{P}(n)} w_k(n) R_{k,c}(n, \mathcal{P}(n))\,, \tag{2.10}$$

with $w_k(n)$ suitable weights that take into account fairness and QoS constraints.

2.1.2 Exhaustive Search Scheduling

At each slot, we aim at scheduling the set of streams that maximizes WSR.
This problem can be solved by considering all $(\sum_{i=1}^{M} \frac{K!}{i!(K-i)!})^N$ possible sets and evaluating the WSR achieved by each candidate set. Unfortunately, this *exhaustive search* (EA) scheduling has a high computational cost which becomes infeasible for an increasing number of MTs and subcarriers. Simpler and suboptimal scheduling methods are investigated in Section 2.3.

2.2 Maximum Utility Scheduler

In order to balance the opportunistic use of channel resources with fairness among MTs, we consider a multiuser scheduler. We first consider in this section general criteria for the choice of weights of the WSR and we derive the optimum maximum utility scheduler weights for a general utility function. Then we specialize the result for the maximum sum rate scheduler and the proportional fair scheduling.

2.2.1 General Multiuser Scheduling

The achievable rate associated with MT k is

$$R_k(n, \mathcal{P}(n)) = \sum_{c=1}^{N} R_{k,c}(n, \mathcal{P})$$

. In the first slot, the average throughput achieved by MT k is

$$T_k(1) = 0 \quad k = 1, 2, \ldots, K$$

. The estimate of the average throughput achieved by MT k can be updated as

$$T_k(n+1) = \begin{cases} (1-\alpha_k)T_k(n) + \alpha_k R_k(n, \mathcal{P}(n)) & k \in \bigcup_{c=1}^{N} \mathcal{S}_c(n)\,, \\ (1-\alpha_k)T_k(n) & k \notin \bigcup_{c=1}^{N} \mathcal{S}_c(n)\,, \end{cases} \tag{2.11}$$

where $\bigcup_{c=1}^{N} \mathcal{S}_c(n)$ is the set of scheduled MTs at slot n. If we aim at achieving an average throughput ρ_k for MT k, we can define the normalized averaged throughput at slot n as

$$B_k(n) = \frac{T_k(n)}{\rho_k}\,. \tag{2.12}$$

In [47], the following concave and differentiable utility function has been proposed to design schedulers

$$U_k(B_k(n)) = \frac{\rho_k(1-\alpha_k)^{\kappa}}{\alpha_k} \frac{1}{1-\kappa} (B_k^{1-\kappa}(n) - 1)\,, \tag{2.13}$$

where $\kappa \in [0, 1) \cup (\infty)$ is a fairness parameter to be chosen according to the desired scheduling policy. For example, for $K = 1$, $\alpha_k \to 0$, $\rho_k = 1$ and $\kappa \to 1$ we obtain the *proportional fair* scheduler (PFS). For $\kappa = 0$ we obtain the utility function of the *maximum sum-rate* scheduler. When $\kappa \to \infty$, (2.13) becomes the utility function of the *max-min* scheduler.

We derive the scheduler that maximizes the sum utility

$$\sum_{k=1}^{K} U_k(B_k(n))\,. \tag{2.14}$$

Following the derivations of [47], the maximization of the sum utility (2.14) is achieved for

$$\mathcal{P}(n) = \arg\max_{\mathcal{I} \subset \mathcal{Y}} \sum_{k:(k,c) \in \mathcal{I}} U_k \left[\frac{1}{\rho_k} \delta_k(\mathcal{I}) \alpha_k R_k(n, \mathcal{I}) + \frac{1}{\rho_k} (1-\alpha_k) T_k(n) \right] \tag{2.15}$$

where $\delta_k(\mathcal{I}) = 1$ if $k \in \mathcal{I}$ and $\delta_k(\mathcal{I}) = 0$ if $k \notin \mathcal{I}$. For all but the scheduled MTs, the allocated rate at slot n is zero, therefore we have

$$\begin{aligned}\mathcal{P}(n) = \arg\max_{\mathcal{I}\subset\mathcal{Y}} \Bigg(&\sum_{k:(k,c)\in\mathcal{I}} U_k\left[\frac{1}{\rho_k}\alpha_k R_k(n,\mathcal{I}) + \frac{1}{\rho_k}(1-\alpha_k)T_k(n)\right] + \\ &- \sum_{k:(k,c)\in\mathcal{I}} U_k\left[\frac{1}{\rho_k}(1-\alpha_k)T_k(n)\right]\Bigg)\,.\end{aligned} \tag{2.16}$$

Under the assumption $(1-\alpha_k)T_k(n) \gg \alpha_k R_k(n,\mathcal{I})$, the following approximation holds

$$\begin{aligned}&U_k\left[\frac{1}{\rho_k}\alpha_k R_k(n,\mathcal{I}) + \frac{1}{\rho_k}(1-\alpha_k)T_k(n)\right] - U_k\left[\frac{1}{\rho_k}(1-\alpha_k)T_k(n)\right] \approx \\ &\approx \alpha_k R_k(n,\mathcal{I})\left.\frac{\partial U_k(x)}{\partial x}\right|_{(1-\alpha_k)T_k(n)/\rho_k}\,.\end{aligned} \tag{2.17}$$

The derivative can be written as

$$\left.\frac{\partial U_k(x)}{\partial x}\right|_{(1-\alpha_k)T_k(n)/\rho_k} = \frac{\rho_k(1-\alpha_k)^{-\kappa}}{\alpha_k\rho_k^{-\kappa}}T_k(n)^{-\kappa}\,. \tag{2.18}$$

Hence, the set of MTs $\mathcal{P}(n)$ that maximizes (2.14) is

$$\mathcal{P}(n) = \arg\max_{\mathcal{I}\subset\mathcal{Y}} \quad \mathcal{R}(\mathcal{I}) = \arg\max_{\mathcal{I}\subset\mathcal{Y}} \sum_{(k,c)\in\mathcal{I}} w_k(n)R_{k,c}(n,\mathcal{I})\,, \tag{2.19}$$

with weights

$$w_k(n) = \sum_{c:(k,c)\in\mathcal{I}} \frac{R_{k,c}(n,\mathcal{I})\rho_k^{\kappa}}{(1-\alpha_k)^{\kappa}T_k(n)^{\kappa}}\,, \tag{2.20}$$

where $\mathcal{Y} = \{(k,c) : k\in\{1,\cdots,K\}, c\in\{1,\cdots,N\}\}$ is the set of all possible streams. Note that for $K=1$, (2.20) boils down to the maximum utility scheduler of [47].

2.2.2 Maximum Sum Rate Scheduler

The *maximum sum rate* scheduler does not consider the fairness among users ($\kappa = 0$), and simply aims at maximizing the achievable sum rate (SR), providing $w_k = 1$, for $k = 1,\cdots,K$, and

$$\mathcal{P}(n) = \arg\max_{\mathcal{I}\subset\mathcal{Y}} R(\mathcal{I}) = \arg\max_{\mathcal{I}\subset\mathcal{Y}} \sum_{(k,c)\in\mathcal{I}} R_{k,c}(n,\mathcal{I})\,. \tag{2.21}$$

2.2.3 Proportional Fair Scheduling

The multiuser multicarrier *proportional fair* scheduling (MMPFS) algorithm [48] is an extension to the OFDM multi-user scenario of the PFS algorithm.
For MMPFS, the average throughput of MT k is updated as in (2.11) with $\alpha_k = 1/\tau$, where τ is a parameter related to the time over which fairness should be achieved. In [49] it has been shown that proportional fairness, maximizing $\sum_k \log_2 T_k(n)$, is achieved by scheduling MTs as

$$\mathcal{P}(n) = \arg\max_{\mathcal{I}\subset\mathcal{Y}} \sum_{(k,c)\in\mathcal{I}} \log_2 \left(1 + \frac{R_{k,c}(n,\mathcal{I})}{(\tau-1)T_k(n-1)}\right) . \tag{2.22}$$

We observe that for $\tau >> 1$ we can approximate

$$\log_2 \left(1 + \frac{R_{k,c}(n,\mathcal{I})}{(\tau-1)T_k(n-1)}\right) \approx \frac{R_{k,c}(n,\mathcal{I})}{(\tau-1)T_k(n-1)} \tag{2.23}$$

and MPFS (2.22) coincides with the maximization of the WSR (2.19) with weights (2.20), $\rho_k = 1$, $\alpha_k = \frac{1}{\tau}$ and $\kappa = 1$.

2.3 Greedy Scheduling Strategies

In the following we investigate sub-optimal solutions to the problem (2.19) for a few MTs, i.e. small K, where the probability of having a fully loaded system is small. In fact, in this scenario power distribution has an important role in selecting the optimal MT set. In Section 2.3.3 we will consider the case of a high number of MTs K, and in this case a simplification of scheduling is possible. For ease of notation we drop both slot (n) and OFDM symbol (t) index in the remaining of the Chapter.

2.3.1 Multicarrier Greedy (MG)

In [15], a greedy scheduling algorithm in a SC flat fading system has been proposed, where MTs are selected one by one as long as the throughput increases and it has been then extended to an OFDM system in [22] and denote here multicarrier greedy (MG).

The MG algorithm comprises N_{step} steps, and at each step we select the stream that maximizes the increase of WSR. Let $\mathcal{S}^{(i)}$ be the set of streams scheduled for transmission at step i, $(i = 1, \cdots, N_{step})$, with the corresponding WSR $\mathcal{R}(\mathcal{S}^{(i)})$. Initially we have $\mathcal{S}^{(0)} = \varnothing$. The stream selected at step $i + 1$, is

$$(\bar{k}, \bar{c}) = \arg \max_{(k,c) \in \mathcal{Y} \setminus \mathcal{S}^{(i)}} \mathcal{R}\left(\mathcal{S}^{(i)} \cup \{(k, c)\}\right), \tag{2.24}$$

and we set $\mathcal{S}^{(i+1)} = \mathcal{S}^{(i)} \cup \{(\bar{k}, \bar{c})\}$. The WSR $\mathcal{R}\left(\mathcal{S}^{(i)}\right)$ increases at each step, since stream (k, c) is inserted under the condition that

$$\mathcal{R}\left(\mathcal{S}^{(i)} \cup \{(\bar{k}, \bar{c})\}\right) \geq \mathcal{R}\left(\mathcal{S}^{(i)}\right). \tag{2.25}$$

When (2.25) does not hold, the algorithm is stopped, $N_{step} = i$ and $\mathcal{P} = \mathcal{S}^{(N_{step})}$. Hence, N_{step} is a random variable. Evaluation of the WSR in (2.24) for the current set of streams is based on the SNIR estimate [15] for stream $(j, c) \in \mathcal{S}^{(i)} \cup \{(k, c)\}$, with $(k, c) \in \mathcal{Y} \setminus \mathcal{S}^{(i)}$, i.e.

$$\gamma_{j,c}^{(i+1)} = \frac{P}{(i + 1) \cdot ||\mathbf{g}_{j,c}^{(i)}||^2} \xi_{j,c}, \tag{2.26}$$

where $\xi_{j,c}$ is given by (2.6) while $\mathbf{g}_{j,c}^{(i)}$ is the j-th column of the BF matrix $\mathbf{G}_c^{(i)}$ for MTs scheduled at step i. Note that total power P has been divided by $|\mathcal{S}^{(i+1)}| = i+1$ in order to obtain the per stream power P_S.

2.3.2 Projection Based Greedy (PBG)

According to the MG algorithm, the introduction of a new candidate stream $(\bar{k}, \bar{c})$ into the set $\mathcal{S}^{(i)}$ at step $i + 1$ decreases the SNIRs (2.26) for two reasons:

a) the power is redistributed among all streams;

b) BF of streams already scheduled on the same RB is modified.

Due to a), it is beneficial to perform scheduling jointly among RBs rather than separately on each RB. Due to b), a new BF matrix must be computed for MTs scheduled on RB $\bar{c}$ of the candidate stream. Hence, at each step many BFs must be designed for each RB to test (2.25) and only one candidate stream is then scheduled. In order to reduce the computational complexity, the projection based greedy (PBG) algorithm [23] assumes that the insertion of a new stream does not significantly alter the SNIR of already scheduled streams. Indeed, this assumption holds as long as the CV of the candidate stream is almost orthogonal to CVs of previously scheduled streams. Therefore, we update the SNIR estimate of already scheduled streams as follows

$$\gamma_{p,q}^{(i+1)} = \frac{i}{i+1}\gamma_{p,q}^{(i)} \quad (p,q) \in \mathcal{S}^{(i)}\,, \tag{2.27}$$

for $i = 2, 3, \cdots, N_{step} - 1$, while for the first step we set $\gamma_{p,q}^{(1)} = \xi_{p,q}$, $(p,q) \in \mathcal{S}^{(1)}$. Furthermore, the evaluation of the SNIR for the candidate streams requires only the computation of $||\mathbf{g}_{k,c}^{(i)}||^2$ instead of the entire beamformer. In particular, if we define

$$a_{k,c}(\mathcal{S}^{(i)}) = \frac{1}{||\mathbf{g}_{k,c}^{(i)}||^2}, \tag{2.28}$$

from (2.26) we have

$$\gamma_{k,c}^{(i+1)} = \frac{P}{i+1}\,\xi_{k,c}a_{k,c}(\mathcal{S}^{(i)}) \quad (k,c) \in \mathcal{Y} \setminus \mathcal{S}^{(i)}. \tag{2.29}$$

In order to compute (2.28) and the corresponding SNIR (2.29) of the candidate stream (k,c), it can be observed that its BF vector is obtained by the orthogonalization of $\bar{\mathbf{h}}_{k,c}$ with respect to the normalized CV of already scheduled streams on the same RB. Hence, an orthonormal basis $\mathcal{B}_c(i) = \left\{\bar{\mathbf{b}}_{j,c}\right\}$ is first constructed for the space generated by the channel vectors $\{\bar{\mathbf{h}}_{p,c}\}$ of streams in $\mathcal{S}^{(i)}$ on RB c. Then the BF vector for stream (k,c) would be proportional to

$$\mathbf{g}_{k,c}^{(i)} \propto \bar{\mathbf{h}}_{k,c} - \sum_{j=1}^{|\mathcal{B}_c(i)|} \left(\bar{\mathbf{h}}_{k,c} \cdot \bar{\mathbf{b}}_{j,c}^{H}\right) \bar{\mathbf{b}}_{j,c}\,. \tag{2.30}$$

Now, by imposing $\mathbf{G}_c^{(i)}\bar{\mathbf{H}}_c = \mathbf{I}$, the identity matrix, it is $\bar{\mathbf{h}}_{k,c}^{H}\mathbf{g}_{k,c}^{(i)} = 1$ and we have

$$a_{k,c}(\mathcal{S}^{(i)}) = \left|1 - \sum_{j=1}^{|\mathcal{B}_c(i)|} \left|\bar{\mathbf{h}}_{k,c} \cdot \bar{\mathbf{b}}_{j,c}^{H}\right|^2\right|^2 . \tag{2.31}$$

By using (2.29) and (2.31), there is no need to determine a new BF in correspondence of each candidate stream; instead, only the basis $\mathcal{B}_c(i)$ needs to be updated at each step, and this requires only few vector multiplications. Note that the computation of $a_{k,c}$ is based on the projection of the candidate vector on the basis, as from the acronym PBG. Once all streams have been scheduled, a BF is computed to perform transmission.

2.3.3 Greedy Scheduling Strategies in the High K Scenario

If $K \gg M$, multiuser diversity provides M orthogonal streams on each RB with very high probability, thus we will have almost always a fully loaded system, i.e. $|\mathcal{S}_c| = M$. In this case, both MG and PBG algorithms can be simplified without redistributing the available power at each new insertion, and the per stream power (2.4) becomes

$$P_S = \frac{P}{N \cdot M}. \tag{2.32}$$

Scheduling can then be simplified by operating independently on each RB.

2.3.4 Multicarrier Semi-Orthogonal User Selection Algorithm (MSUS)

The SUS scheme [10] can be easily generalized to the OFDM scenario and is here denoted as multicarrier SUS (MSUS). The generalization includes also the maximization of the WSR instead of the SR as considered in [10]. MSUS proceeds by steps, now applied separately on each RB. For RB c, let $\mathcal{A}_c^{(1)} = \{1, \cdots, K\}$ be the initial set containing the indexes of all MTs. The scheduled stream at step 1 is characterized by having maximum CQI, i.e.

$$k_1 = \arg\max_{k \in \mathcal{A}_c^{(1)}} \quad w_k \cdot \log_2(1 + \xi_{k,c}). \tag{2.33}$$

After selecting i streams, the $(i+1)$th stream k_{i+1} is chosen within the set

$$\mathcal{A}_c^{(i+1)} = \{k \in \mathcal{A}_c^{(i)} \backslash k_{(i)}, c : |\hat{\mathbf{h}}_{k,c}, \hat{\mathbf{h}}_{k_{j,c},c}^H| \leq \epsilon, \quad 1 \leq j \leq i\} \quad i = 2, \cdots, M \tag{2.34}$$

as

$$k_{i+1,c} = \arg\max_{k \in \mathcal{A}_c^{(i+1)}} \quad w_k \log_2(1 + \xi_{k,c}) \tag{2.35}$$

where ϵ is a design parameter that sets the maximum correlation allowed between the quantized channel vectors of the selected MTs. We note that in MSUS we apply N SC SUS in parallel, one for each RB. Also in this case the number of steps is random as the algorithm ends when set $\mathcal{A}_c^{(i)}$ is empty. Once MTs have been scheduled, the total power is equally distributed among scheduled streams according to (2.4).

2.4 Pre-Selection Methods

In the MG algorithm the WSR $\mathcal{R}\left(\mathcal{S}^{(i)}\right)$ increases at each step and using (2.9) and (2.10), condition (2.25) becomes

$$\sum_{(p,q)\in\mathcal{S}^{(i+1)}} w_p \log_2(1+\gamma_{p,q}^{(i+1)}) \geq \sum_{(p,q)\in\mathcal{S}^{(i)}} w_p . \log_2(1+\gamma_{p,q}^{(i)}) \tag{2.36}$$

From (2.26) we obtain that this condition is satisfied only if the SNIR is high enough to compensate for losses incurred by the insertion of a new scheduled stream, i.e. the power redistribution and the BF modification, as described by conditions a) and b) of Section III.B. This observation suggests a further simplification of the PBG algorithm, by a-priori excluding as candidate streams whose SNIR is below a certain threshold. Preselection techniques aim at providing simple methods for excluding streams with low SNIR. Indeed, as for each candidate stream the SNIR (2.29) must be evaluated, by excluding streams that could never be inserted, the scheduling procedure can be fastened [23].

2.4.1 Preselection PBG (PPBG)

We first observe from (2.31) that $a_{k,c}(\mathcal{S}^{(i)}) \leq 1$ and from (2.28) we obtain

$$\gamma_{k,c}^{(i+1)} \leq \xi_{k,c}\frac{P}{i+1}. \tag{2.37}$$

Therefore, at step i of PBG there is a minimum value of $\xi_{k,c}$ that satisfies (2.36), denoted $A_{k,c}(i+1)$, and we consider for scheduling only streams having SNIR

$$\xi_{k,c} > A_{k,c}(i+1). \tag{2.38}$$

At high SNR we have

$$A_{k,c}(i+1) \approx \sqrt[w_k]{\prod_{(p,q)\in\mathcal{S}^{(i)}} \left(\frac{i+1}{i}\right)^{w_p} \frac{(i+1)}{P}}. \tag{2.39}$$

Proof: We observe that condition (2.36) is equivalent to

$$\left[1+\frac{P}{i+1}\xi_{k,c}a_{k,c}(\mathcal{S}^{(i)})\right]^{w_k} \prod_{(p,q)\in\mathcal{S}^{(i)}} [1+\gamma_{p,q}^{(i+1)})]^{w_p} > \prod_{(p,q)\in\mathcal{S}^{(i)}} [1+\gamma_{p,q}^{(i)}]^{w_p} \tag{2.40}$$

where (k,c) is the generic candidate stream.

In the high SNR scenario, with $\xi_{p,q} >> 1$, we have $1+\gamma_{p,q}^{(i)} \approx \gamma_{p,q}^{(i)}$ and from (2.27), condition (2.40) becomes

$$\left(\frac{P}{i+1}\xi_{k,c}a_{k,c}(\mathcal{S}^{(i)})\right)^{w_k} \prod_{(p,q)\in\mathcal{S}^{(i)}} \left(\frac{P}{i+1}\right)^{w_p} > \prod_{(p,q)\in\mathcal{S}^{(i)}} \left(\frac{P}{i}\right)^{w_p}. \tag{2.41}$$

Hence from (2.41), (2.39) follows. We note that, in the high K scenario, (2.40) becomes

$$\left[1 + P_S\xi_{k,c}a_{k,c}(\mathcal{S}^{(i)})\right]^{w_k} > 1 \tag{2.42}$$

and $A_{k,c}(i) = 0$.
Then by considering only streams (k, c) satisfying (2.38), we decrease the number of comparisons and SNIR updates at each step of PBG. In the high K scenario preselection technique is not feasible; in fact, $A_{k,c}(i) \to 0$ for $K \to \infty$, and therefore (2.38) is verified by all streams.
We further note that $A_{k,c}(i)$ is an increasing function of i; hence, streams whose CQI is below the threshold $A_{k,c}(i)$ at step i can be neglected also in the next steps.

2.4.2 Simplified Preselection PBG (SPPBG)

A further simplification in preselection is achieved by considering $w_k \approx w_p \approx 1$ in (2.39) to yield

$$A_{k,c}(i+1) \approx \frac{(i+1)}{P}\left(\frac{i+1}{i}\right)^{i}. \tag{2.43}$$

Within PBG methods, we note that this approach becomes optimal when the scheduling objective coincides with the maximization of the SR. However, for the maximization of the WSR, S-PPBG is in general suboptimal.

2.5 Complexity Analysis

We analyze the worst case complexity of the various approaches, in terms of both computational complexity and memory requirement.

2.5.1 Computational Complexity

We assume that a comparison yields a computational complexity equal to λ complex multiplications (CMUX), while the inversion of an $M \times M$ matrix performed by

Gaussian elimination methods, has complexity $\frac{M \cdot (M^2-1)}{3}$ CMUX. The BF and $\| \mathbf{g}_{k,c} \|^2$ evaluation has therefore complexity

$$BFC = 2|\mathcal{S}_c| \cdot M^2 + \frac{M \cdot (M^2-1)}{3} + |\mathcal{S}_c| \cdot M. \tag{2.44}$$

We first observe that all considered algorithms select one stream per step, until at most M streams are allocated on each RB, thus in general $N_{step} \leq N \cdot M$. At step i, $|\mathcal{Y} \backslash \mathcal{S}^{(i)}| = K \cdot N - i$ streams are considered for insertion in $\mathcal{S}^{(i+1)}$. Furthermore, at each step, the per stream power P_S is adapted, due to the insertion of a candidate stream in $\mathcal{S}^{(i+1)}$. The inversion of an $M \times M$ matrix performed by the Guassian Elimination method has complexity $\frac{M \cdot (M^2-1)}{3}$.

MG complexity. Complexity of the MG algorithm in the low K scenario is given by

$$\begin{aligned} \mathbf{C}_{MG-lowK} = \lambda \cdot N \cdot K + \sum_{i=2}^{N_{step}} (i-1) + \\ + (K - |\mathcal{S}^{(i)}_{\zeta(i-1)}|) \cdot (BFC+2) + \lambda(K \cdot N - i + 1) + \lambda \end{aligned} \tag{2.45}$$

where $\zeta(i-1)$ denotes the RB of the stream selected at step $i-1$. The first term in (2.45) accounts for the selection of the stream with maximum CQI. The remaining terms account for steps 2 through N_{step}, with a) update of SNIR estimate of the $(i-1)$ already scheduled streams, b) computation of a new BF for each of the $(K - |\mathcal{S}^{(i)}_{\zeta(i-1)}|)$ candidate streams on subcarrier $\zeta(i-1)$, c) evaluation of $\| \mathbf{g}_{k,\zeta(i-1)} \|^2$, d) update of the SNIR estimates and e) evaluation of the WSR. Lastly, the algorithm determines the stream which maximizes the WSR at step i and checks condition (2.25).

In the high K scenario complexity becomes

$$\begin{aligned} \mathbf{C}_{MG-highK} = \lambda \cdot N \cdot K + N \cdot \sum_{i=2}^{M} \{(K-i+1) \cdot (BFC+2) + \\ \lambda \cdot (K-i+1) + \lambda\}, \end{aligned} \tag{2.46}$$

since now $N_{step} = M$ and no power update is necessary at each step.

PBG complexity. Complexity of the PBG in the low K scenario is

$$\begin{aligned} \mathbf{C}_{PBG} = \lambda \cdot N \cdot K + N \cdot BFC + \sum_{i=2}^{N_{step}} \Big\{ (i-1) + (K - |\mathcal{S}^{(i)}_{\zeta(i-1)}|) \cdot (M+2) + \\ + |\mathcal{S}^{(i)}_{\zeta(i-1)}| + 2 \cdot M + \lambda \cdot (K \cdot N - i + 1) + \lambda \Big\}. \end{aligned} \tag{2.47}$$

In fact, the PBG algorithm for each candidate stream on RB $\zeta(i-1)$ performs a) the projection of CV on the orthogonal basis and b) updates the SNIR estimate. At each step, the basis is also updated according to the CV of last scheduled stream. At the end, the BF matrix is computed according to the set of scheduled streams. In the high K scenario we have

$$\begin{aligned}\mathbf{C}_{PBG-highK} = \lambda \cdot N \cdot K + N \cdot BFC + N \cdot \sum_{i=2}^{M} \{(M+2)\cdot(K-i+1)+i \\ +2\cdot M + \lambda\cdot(K-i+1)+\lambda\},\end{aligned} \tag{2.48}$$

since scheduling can be performed in parallel on all RBs.

PPBG complexity. The complexity of the PPBG in the low K scenario is given by

$$\begin{aligned}\mathbf{C}_{PPBG} = \lambda \cdot N \cdot K + N \cdot BFC + \sum_{i=2}^{N_{step}} \{(i-1)+ \\ +(K-|\mathcal{S}^{(i)}_{\zeta(i-1)}|)\cdot(M+2)+|\mathcal{S}^{(i)}_{\zeta(i-1)}|+2\cdot M+1+\lambda\cdot(K\cdot N-i+1)+\lambda\Big\}.\end{aligned} \tag{2.49}$$

It only differs from PBG in the evaluation of $A_{k,c}(i+1)$ at each step, since it depends on the set of scheduled streams. Similarly, in the high K scenario we have

$$\begin{aligned}\mathbf{C}_{PPBG-highK} = \lambda \cdot N \cdot K + N \cdot BFC + N \cdot \sum_{i=2}^{M} \{(M+2)\cdot(K-i+1)+ \\ +i+2\cdot M+1+\lambda\cdot(K-i+1)+\lambda\},\end{aligned} \tag{2.50}$$

SPPBG complexity. Applying the S-PPBG algorithm, we have an additional cost due to (2.38); on the other hand, on RB c, at each step i we exclude a number of streams $Q_c(i)$ from the set of possible streams. $Q_c(i)$ takes into account also the scheduled streams. Then at step i we have $J_{i,c} = K - \sum_{j=1}^{i} Q_c(i)$ candidate streams on RB c and in total $J_i = |\mathcal{Y}\backslash\mathcal{S}^{(i)}| = \sum_{c=1}^{N} J_{i,c}$. Complexity becomes

$$\begin{aligned}\mathbf{C}_{SPPBG} = \lambda \cdot N \cdot K + N \cdot BFC + \sum_{i=2}^{N_{step}} \Big\{(i-1)+\big(J_{i,\zeta(i-1)}+ \\ -|\mathcal{S}^{(i)}_{\zeta(i-1)}|\big)\cdot(M+2)+|\mathcal{S}^{(i)}_{\zeta(i-1)}|+2\cdot M+\lambda\cdot(2J_i+1)\Big\}.\end{aligned} \tag{2.51}$$

Note that $Q_c(i)$ is a random variables depending on the channel realization. In the high K scenario we still consider power adjustment; otherwise, from (2.43), we could never exclude streams, and then S-PPBG would become PBG. Complexity of S-PPBG in the high K scenario becomes

$$\begin{aligned} \mathbf{C}_{SPPBG-highK} &= \lambda \cdot N \cdot K + N \cdot BFC + \\ &+ \cdot \sum_{i=2}^{N_{step}} \left\{ (i-1) + (J_{i,\zeta(i-1)} - i + 1|) \cdot (M+2) + \right. \\ &\left. + i + 2 \cdot M + \lambda \cdot (2J_i + 1) \right\}. \end{aligned} \tag{2.52}$$

The MSUS algorithm is equivalent to N SUS algorithms working in parallel. We remind that at each step SUS considers $|\mathcal{A}_c^{(i)}| = K - i - \sum_{j=1}^{i} Q(i)$ candidate MTs, where $Q(i)$ is the number of MTs excluded at step i. It is

$$\begin{aligned} &\mathbf{C}_{MSUS} = N \cdot BFC + \\ &+ \sum_{c=1}^{N} \left(\lambda \cdot K + \sum_{i=2}^{M} (|\mathcal{A}_c^{(i-1)}| \cdot i + \lambda \cdot |\mathcal{A}_c^{(i-1)}| + |\mathcal{A}_c^{(i)}|(\lambda+1)) \right). \end{aligned} \tag{2.53}$$

2.5.2 Asymptotic Complexity Analysis

According to complexities required by various scheduling algorithms, we investigate their asymptotic behavior with respect to K as a function of K. For MG we have

$$\mathbf{C}_{MG-\infty} \approx K[\lambda \cdot N + N(M-1)(BFC + 2 + \lambda)] + \mathcal{O}(K) \tag{2.54}$$

where $\mathcal{O}(K)$ indicates a term which goes asymptotically to 0 faster than K. For PBG and PPBG we have

$$\mathbf{C}_{PBG-\infty} = \mathbf{C}_{PPBG-\infty} \approx K[\lambda \cdot N + N(M-1)(M + 2 + \lambda)] + \mathcal{O}(K) \tag{2.55}$$

Both S-PPBG and MSUS perform the exclusion of worse streams. Let β_i be the percentage of streams excluded at step i, for S-PPBG it is $J_{i,c} = (K - i) \cdot (1 - \beta_i)$ while for MSUS $\mathcal{A}_c^{(i)} = (K - i) \cdot (1 - \beta_i)$. Asymptotic expressions are

$$\mathbf{C}_{SPPBG-\infty} \approx K[\lambda \cdot N + D \cdot (M+2) + \lambda \cdot 2 \cdot D \cdot N] + \mathcal{O}(K), \tag{2.56}$$

and

$$\mathbf{C}_{MSUS-\infty} \approx K\left[N \cdot \lambda + B + \lambda \cdot (M-1) \cdot C + (\lambda+1) \cdot D\right] + \mathcal{O}(K) \tag{2.57}$$

where $B = \sum_{i=2}^{M} i(1 - \beta_{i-1})$ and $C = \sum_{i=2}^{M} (1 - \beta_{i-1})$ and $D = \sum_{i=2}^{M} (1 - \beta_i)$.

2.5.3 Memory Occupation

Lastly we investigate memory requirements of the scheduling algorithms in terms of complex location (CLS) units. We first note that all algorithms store a) CDI and CQI of all streams, b) the set of selected streams and c) the final BFs; then a memory occupation of $\mathcal{M}_{COMM} = N \cdot M \cdot K + K \cdot N + N \cdot M^2 + M \cdot N$ CLS is common to all algorithms. For MG we have

$$\mathcal{M}_{MG} = \mathcal{M}_{COMM} + K \cdot N + M \cdot N + K + M^2 \cdot K + 2 \tag{2.58}$$

since MG stores a) $\gamma_{j,c}$ (or, equivalently, $\| \mathbf{g}_{j,c} \|^2$), requiring $K \cdot N$ CLS, b) per MT rates ($N \cdot M$ CLS as worst case), c) new BF ($K \cdot M^2$ CLS), d) total rate provided by each candidate (K CLS), and e) current and last final rates (2 CLS). For PBG and PPBG we have

$$\mathcal{M}_{PPBG} = \mathcal{M}_{PBG} = \mathcal{M}_{COMM} + K \cdot N + M \cdot N + K + M^2 \cdot N + 2, \tag{2.59}$$

as PBG stores a) the value $\sqrt{a_{k,c}}$, b) total rate provided by each candidate stream (K CLS) and c) orthogonal basis ($M^2 \cdot N$ CLS).
The S-PPBG memory requirement is given by

$$\mathcal{M}_{SPPBG} = \mathcal{M}_{COMM} + \cdot K \cdot N + M \cdot N + K + M^2 \cdot N + 2 + M \cdot N. \tag{2.60}$$

With respect to PBG, it needs to store also $A_{k,c}(i)$ ($M \cdot N$ CLS as worst case).
Finally, for MSUS we have

$$\mathcal{M}_{MSUS} = \mathcal{M}_{COMM} + M \cdot N + N \cdot K + 1 + K \cdot N \tag{2.61}$$

as MSUS stores a) correlations of candidate streams and last inserted stream ($N \cdot K$ CLS), b) the value of ϵ (1 CLS) and c) the set of total rates of each candidate ($K \cdot N$ CLS as worst case).

Chapter 3

Performance Results

We consider a BS equipped with $M = 4$ antennas spaced by 10 wavelength at the carrier frequency of 2 GHz. The channel is modeled as time-variant, flat Rayleigh fading, according to the spatial channel model (SCM) [50]. All MTs are uniformly distributed in a cell of radius 500 m, as in [51]; the time slot duration is $T = 0.5$ ms and each MT transmits the FB once per slot. The codebook for predictive error quantization is designed from a TS composed of CVs of SCM for MT moving at 3, 50 and 130 km/h with equal probability, a first order linear predictor is adopted and the value chosen for the fairness parameter in PFS is $\tau = 0.1$ s.

3.1 Single Carrier Scenario Results

We define the average sum rate (SR) as

$$\mathrm{SR} = \mathrm{E}\left\{ \sum_{k=1}^{|\mathcal{S}(n)|} \log_2 \left[1 + SNIR_k(t)\right] \right\}, \tag{3.1}$$

where $SNIR_k(t)$ is the SNIR relative to MT k, defined in (1.7) as

$$SNIR_k(t) = \frac{p_k |\mathbf{h}_k(t)\mathbf{g}_k(n)|^2}{1 + \sum_{i \in \mathcal{S}(n)\setminus k} p_i |\mathbf{h}_k(t)\mathbf{g}_i(n)|^2}. \tag{3.2}$$

3.1.1 Beamforming Performance Results

In Fig. 3.1 we set $K = 20$ and the average SNR to 15 dB. We compare the BFB and PFB strategies in terms of SR as a function of the number of FB bits b for ZF-BF.

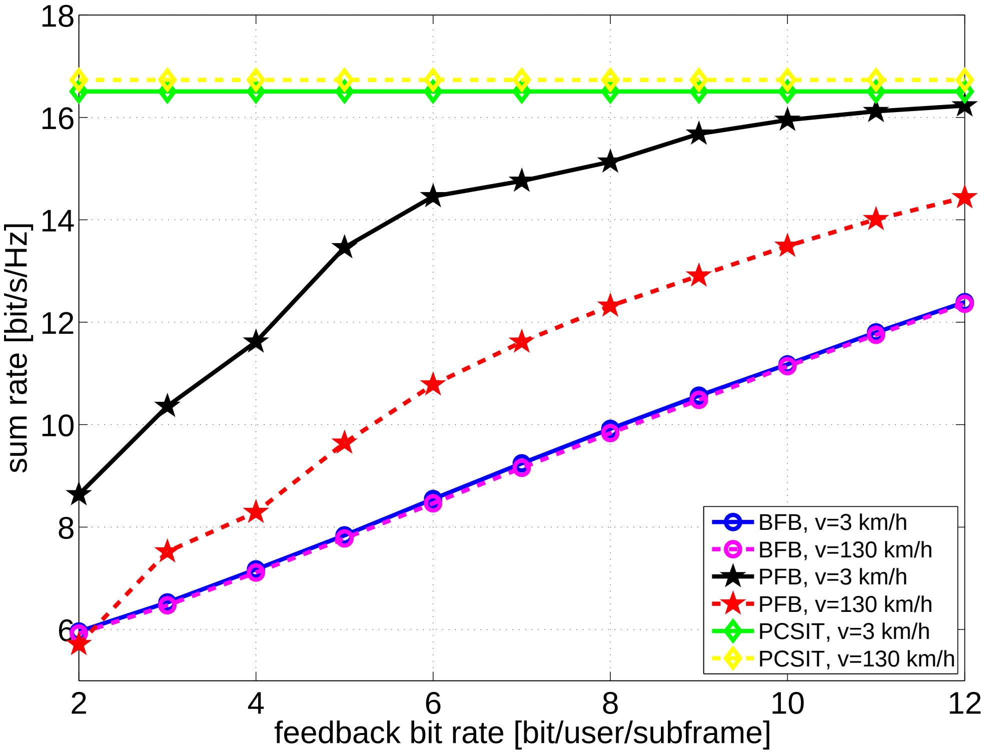

Figure 3.1: SR as a function of FB bits for various FB strategies, with MTs moving at 3 and 130 km/h. SNR = 15 dB.

The proposed PFB significantly outperforms BFB for any FB rate, since it exploits the time correlation of the channel. The gain is more evident at a low MT speed, when, even with a low FB rate, the performance gets close to that of perfect CSI (PCSI). Moreover, even with a highly time variant channel, PFB is still preferable to BFB.

In Fig. 3.2 we evaluate the SR for various FB strategies as a function of the average SNR. First of all, we note that at a low SNR, BFB with MT moving at 130 km/h provides a higher SR than at 3 km/h because with a higher speed PFS does not significantly worsen the achievable throughput. On the other hand, at high SNR BFB with a MT moving at a lower speed gives better performance because at higher velocity the beamformer designed at the beginning of each slot gets outdated for the varying channel conditions causing multiuser interference degradation. And

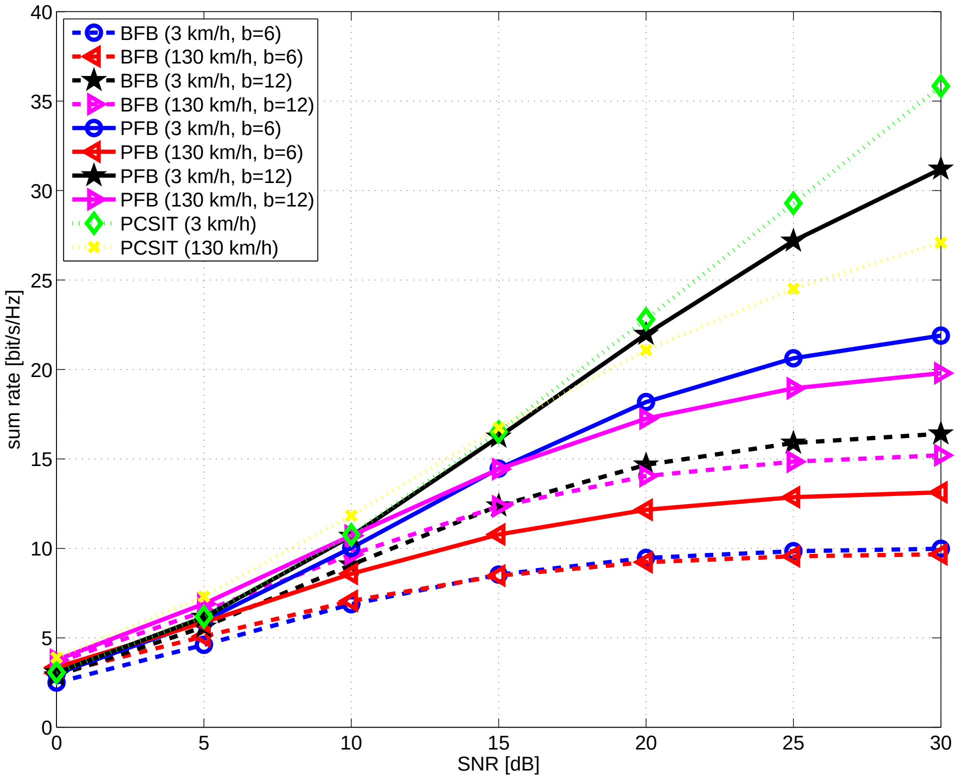

Figure 3.2: SR as a function of SNR for various FB strategies and FB bits. MTs moving at 3 and 130 km/h.

this effect becomes dominant in the high SNR region where interference dominates system noise. We observe that PFB strategy still highly improves BFB especially for a low MT speed and with only $b = 12$ we get performance very close to PCSI. For lack of space we did not include the performance of the proposed FB strategies using MMSE-BF. Nevertheless with this opportunistic approach MMSE-BF does not provide a gain with respect to ZF-BF because the proposed greedy algorithm selects MTs only if this is beneficial for the weighted throughput, thus limiting multiuser interference that MMSE-BF tries to cope with.

Figg. 3.3 and 3.4 compare MMSE-BF and ZF-BF adopting both BFB and PFB and assuming MTs moving at 3 and 130 km/h, respectively; for both figures, we considered $K = 4$ dedicated channels, i.e., in the absence of scheduling, or with a scheduler selecting randomly the $K = 4$ MTs. In this scenario, where the scheduler

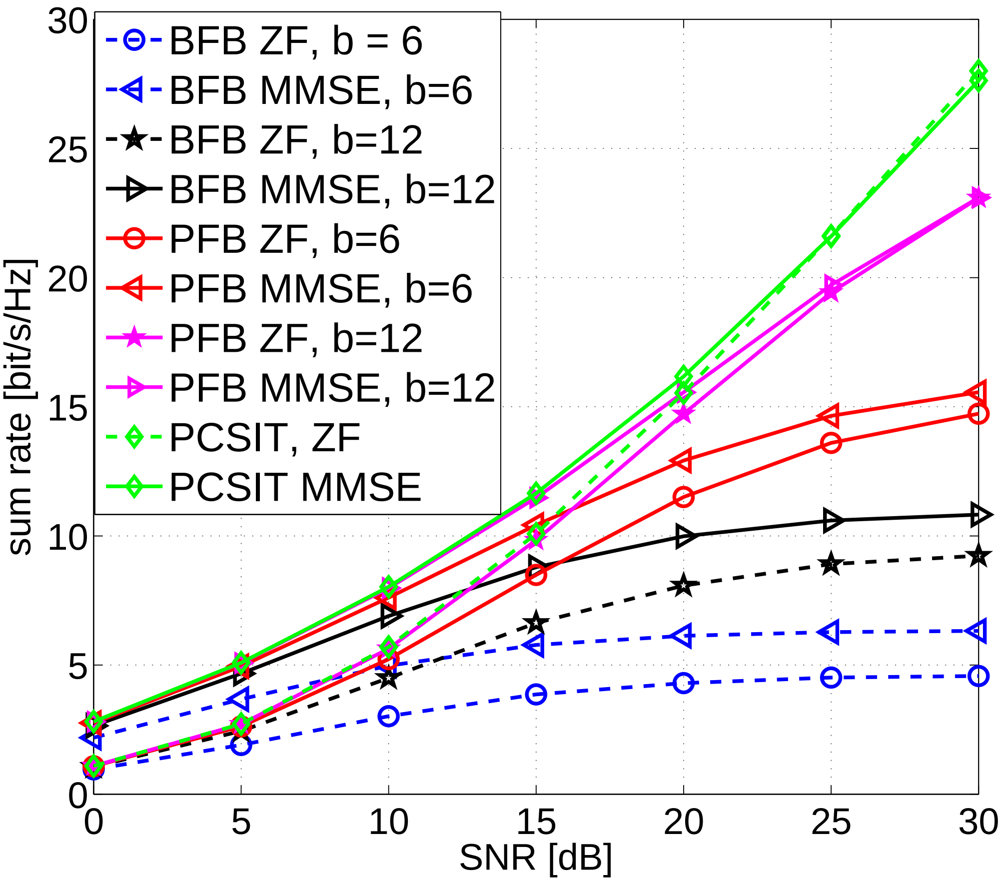

Figure 3.3: SR as a function of SNR for various FB strategies and FB bits adopting both ZF-BF and MMSE-BF. MTs moving at 3 km/h.

does not avoid multiuser interference by a proper user selection, MMSE-BF is preferable because it better copes with multiuser interference due to quantization errors, although it requires a double CQI FB. Nevertheless, we assumed also the case of one CQI FB, considering the mean value of $\cos\Theta_k$ in BF design; also in this case, we verified that MMSE-BF still performs better than ZF-BF in a random scheduling scenario.

3.1.2 FB Performance Results

We evaluate now the performance of FB strategies, as a function of SNR and of FB rate. Simulations are performed considering a set of $K = 20$ users.

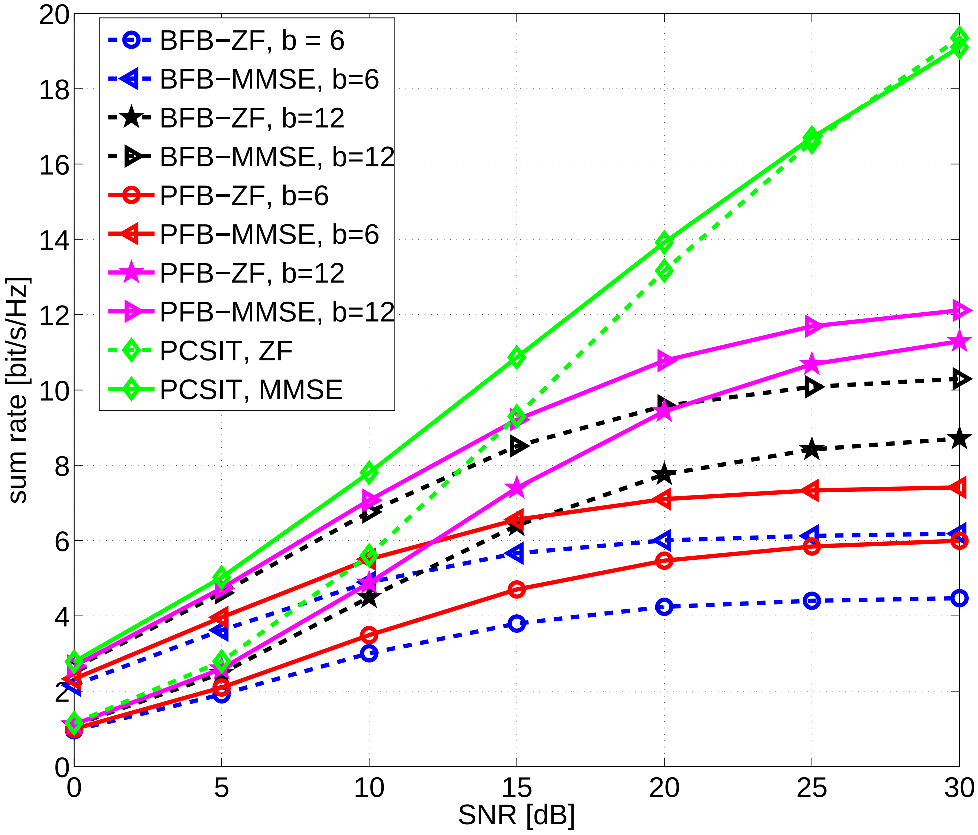

Figure 3.4: SR as a function of SNR for various FB strategies and FB bits adopting both ZF-BF and MMSE-BF. MTs moving at 130 km/h.

We first evaluate LBG technique in terms of average SR in the condition of block fading, where the channel is fixed during the timeslot. Fig. 3.5 shows that for every FB rate the average SR value increases of about 2 bits/s by using the LBG quantization method instead of the RVQ one. Of course, as the FB rate increases the average SR becomes higher as well, since the BS has a better CDI and then on average the achievable rate for users becomes higher. Note that with the SCM model, where the channel is not constant during a timeslot both LBG an RVQ quantization methods provide a worse performance, since the precoder designed at the beginning of the timeslot is not perfectly matched with the actual channel; however, the LBG scheme still have an higher SR than the RVQ one.

We now want to compare the PFB strategy with the UD strategy and BFB. We

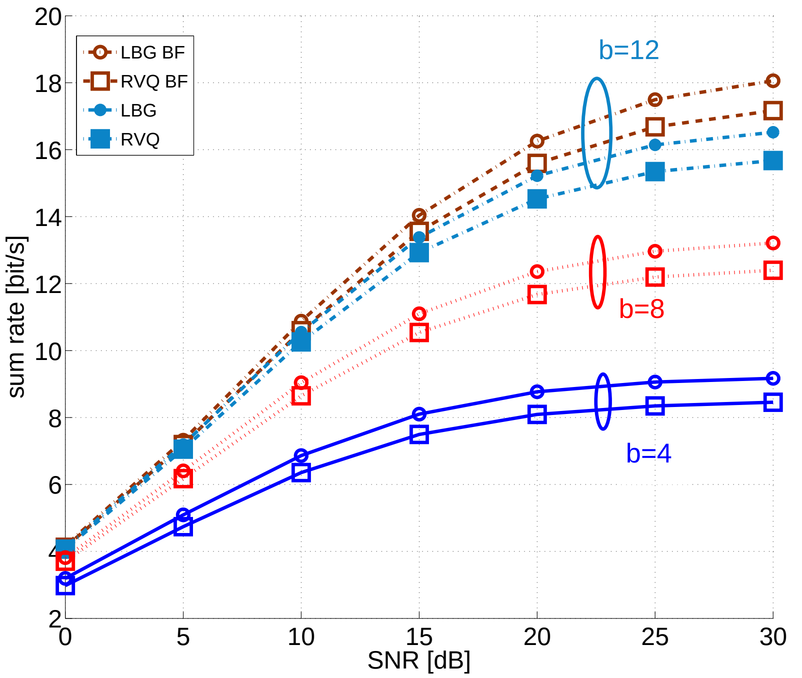

Figure 3.5: Sum rate as a function of SNR using RVQ and LBG quantization methods in case of block fading condition and in case of FB bit rate equal to 12 and terminals moving at speed of 130 Km/h

consider a configuration with channel SNR=15 dB and plot the average SR as a function of the number of FB bit sent by each user. Fig. 3.6 shows that for low speed and low number of FB bits the UD feedback strategy highly improves the average SR with respect to both PFB and BFB. This improvement saturates as the number of FB bits becomes higher than 4, so that with 4 FB bits we achieve the same average SR as the BFB with 11 FB bits. On the other hand, as the number of FB bits becomes higher than 4, the PFB outperforms the UD strategy; in particular, if $b > 10$, the achieved SR differs by only 0.8 bit/s from the one provided by the perfect CSIT once a timeslot. For an higher speed, however, the gap between the three strategies becomes thinner, as illustrated by Fig.3.8; at 50 km/h UD with 8 bits provides the same average SR value as BFB with 11 FB bits; lastly, for 130 km/h the BFB outperforms both UD and PFB with low FB bits , while opposite occurs with more than 6 FB bits, when the PFB provides the highest SR. For the UD strategy, this behavior is due to the fact that with high speed the CSI changes rapidly, and then the user has to send nearly always the most significant b bits; in this case, the control bit used by UD to indicate the meaning of the last $b-1$ bits does not provide useful information and then the UD method provides a worse performance. For the PFB strategy, its behavior in presence of high speed is due to the crude quantization of the prediction error, which affects the direction of the CSIT.

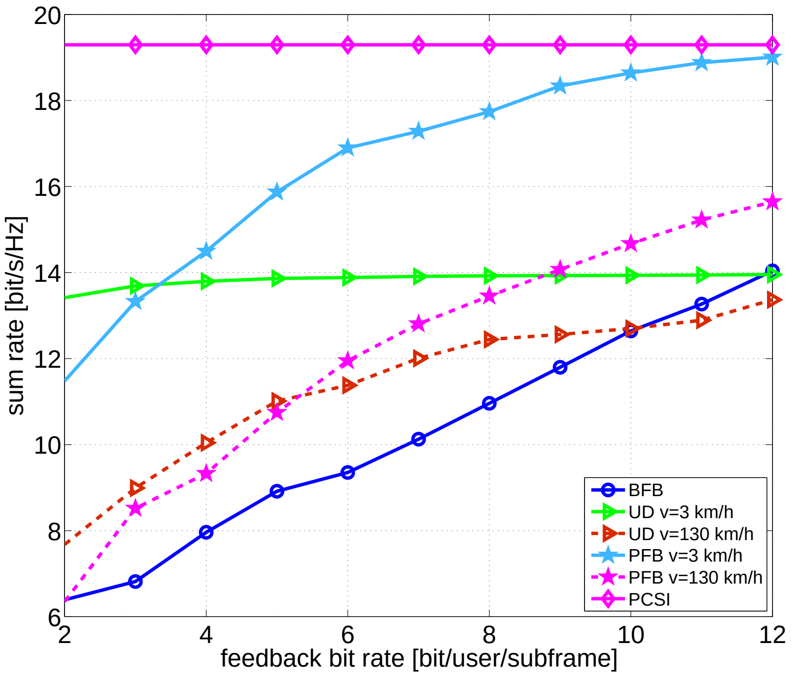

Figure 3.6: Sum rate as a function of FB bits with terminals moving at speed of 3 Km/h

Fig.3.7 illustrates the average SR achieved by BFB UD and PFB schemes with 4 and 12 FB bits when MT speed is 3 km/h; note that with $b = 4$ FB bits UD scheme outperforms both BFB and PFB schemes of about 10 bits/s and provides almost the same average SR as the UD using $b = 12$ bit (the difference between the two is less than 0.5 bit/s). On the other hand, with $b = 8$ and $b = 12$ PFB provides the highest average SR since the quality of CSIT is not limited by the quantization of the direction of the channel, as in UD and BFB; in fact, if we consider UD and BFB with $b = 12$ and $B = 16$, we observe that achieved SR is higher than UD and BFB with $b = 12$ and $B = 12$. For high speed (130 km/h), however, UD and PFB provide a little improvement (of about 1 bit/s for UD and 2 bit/s for PFB) with

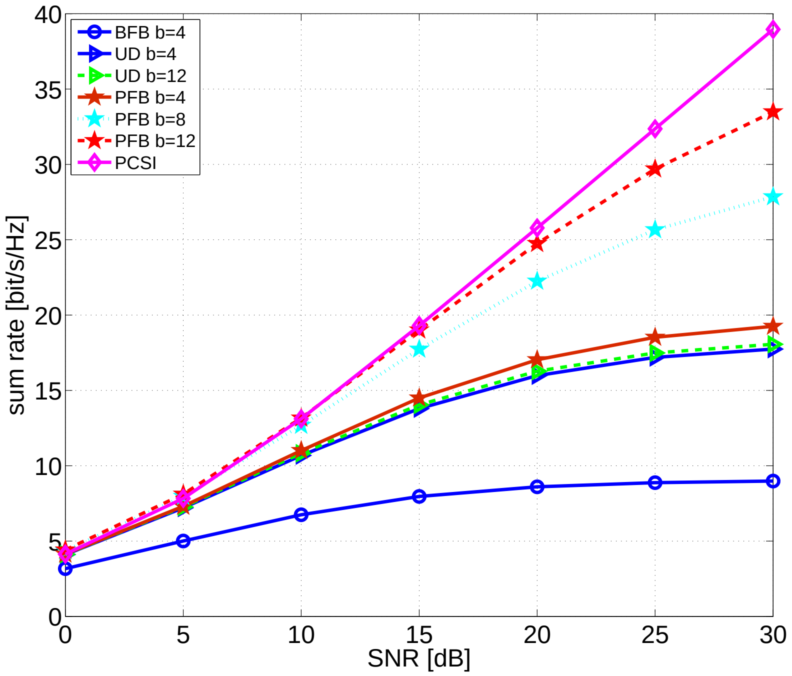

Figure 3.7: Sum rate as a function of SNR using RVQ and LBG quantization methods with terminals moving at speed of 50 Km/h

respect to BFB only with $b = 8$, while with $b = 4$ BFB outperforms both UD and PFB,as illustrated in Fig.3.8; again note that with $b > 4$ PFB outperforms both UD and BFB for it provides the most accurate channel state information at the BS.

3.2 OFDM Scheduling Techniques Performance

We compare the scheduling algorithms in terms of average SR and complexity requirements. we consider an average SNR of 15 dB per RB at the cell border and path loss is included in the channel model. We assume also a realistic MIMO channel with time, frequency and spatial correlation among the elements of $\mathbf{H}_c(t)$, as the channel is modeled as slowly time-variant, frequency selective Rayleigh fading, according the SCM [50] in a OFDM scenario. According to the LTE release, we set transmission bandwidth to 2.5 MHz, divided into $N = 12$ RBs and centered at the carrier frequency of 2 GHz, and each slot is composed of 7 adjacent OFDM symbols. CSI FB is performed with a variable number of bits using an optimized codebook,

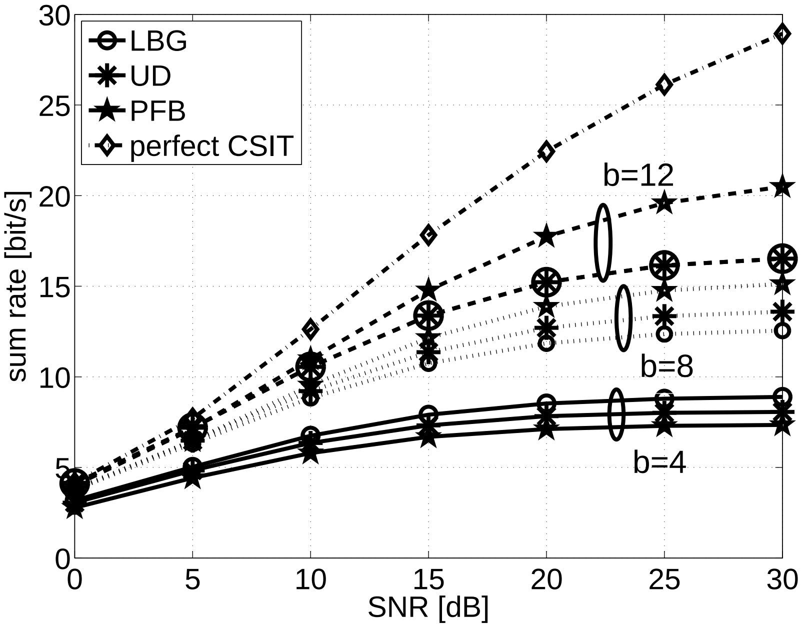

Figure 3.8: Sum rate as a function of SNR using RVQ and LBG quantization methods with terminals moving at speed of 130 Km/h

as detailed in [34].

We extend the definition of average SR provided for SC scenario as

$$\mathrm{SR} = \mathrm{E}\left\{ \sum_{(k,c)\in\mathcal{S}(n)} \log_2\left[1 + SNIR_{k,c}(t)\right] \right\}, \tag{3.3}$$

where $SNIR_{k,c}(t)$ is the SNIR relative to steam (k, c), defined according to (1.7) as

$$SNIR_{k,c}(t) = \frac{p_{k,c}|\mathbf{h}_{k,c}(t)\mathbf{g}_{k,c}(n)|^2}{1 + \sum_{i\in\mathcal{S}_c(n)\setminus k,c} p_i|\mathbf{h}_{k,c}(t)\mathbf{g}_{i,c}(n)|^2}. \tag{3.4}$$

where $\mathbf{g}_{k,c}$ is the k-th column of matrix $\mathbf{G}_c(n)$. We first compare the SR achieved by MG with ES scheduling using as optimization criterion the maximum SR. For complexity reasons simulations have been limited to $N = 4$ RBs. To simplify simulations in the ES method, results of both MG and ES in the high K scenario, $K = 18N, 20N$, refer to $N = 1$. In fact, we verified that for high K the system is fully loaded with a probability higher then 95%; in this scenario the power granted to each carrier is $\frac{P}{N}$, and then user selection can be performed independently on each carrier. We consider both the case of perfect CSI at the transmitter and the case of partial CSI obtained by FB from the receiver, with a FB rate of 12 bit/user/RB/slot. We observe that partial CSI provides a loss on SR of 2 up to 3.5 bit/user/RB/slot, but it does not affect the general behavior of the two algorithms. As we can see from Fig. 3.9, both MG and ES have a very close SR for all K. Hence, in the following we consider MG as performance bound.

Fig. 3.10 illustrates the average SR achieved by the scheduling algorithms as a function of the number of MTs K in the low K scenario for a FB rate of 12 bit/user/RB/slot. We note that there is not an appreciable loss in performance of the simplified, methods. Similarly, simulations in the high K scenario show that MG, PBG and S-PPBG achieve a SR of 16.40 bit/s/Hz, while MSUS provides 15.40 bit/s/Hz. Overall we observe that the simplified algorithms do not provide SR loss for all K. This is mainly due to the fact that all scheduling methods are based on an opportunistic approach, so they all aim at selecting the best set of orthogonal MTs. We also note that all algorithms always select the same first stream, whose CV in turn determines the choice of the other streams. We underline that the average SR of S-PPBG is very close to that of PBG and MG; moreover, since S-PPBG is an approximation of PPBG, we deduce that also PPBG provide the same SR of S-PPBG. Fig. 3.11 confirms this behavior also with a PFS.

We note also in Fig. 3.11 that preselection applied to PBG provides slightly better performance, despite the fact that it considers a lower number of candidate sets. In fact, preselection aims at excluding from scheduling streams that would not increase the WSR, and prevents the scheduler from inserting them for fairness reasons.

Fig. 3.12 reports the average SR versus the FB rate; we observe that the simplified methods are also robust to quantization error; in fact, for all considered values of feedback rate, PBG and S-PPBG provide the same SR of MG.

3.2.1 Outage System Throughput Comparison

At each slot, the BS evaluates a scheduled rate for each stream; since this evaluation is based on imperfect CSIT, the scheduled rate may exceed the channel capacity. In this case, the Shannon theorem does not guarantee the existence of a code allowing an error rate below a given threshold; therefore, the information transmitted is affected by errors with a non-negligible probability.

We consider now the effect of outage on the system throughput, both for the scheduling process and for the performance metric.

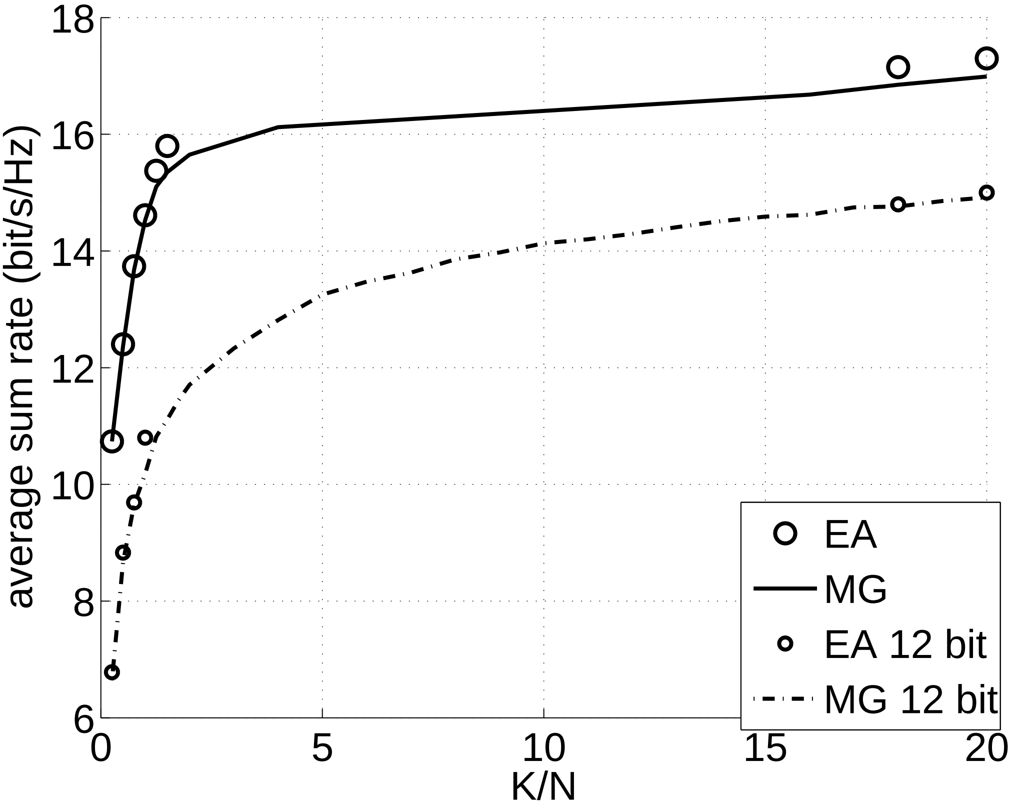

Figure 3.9: Average SR of MG and ES versus of total number of MTs K.

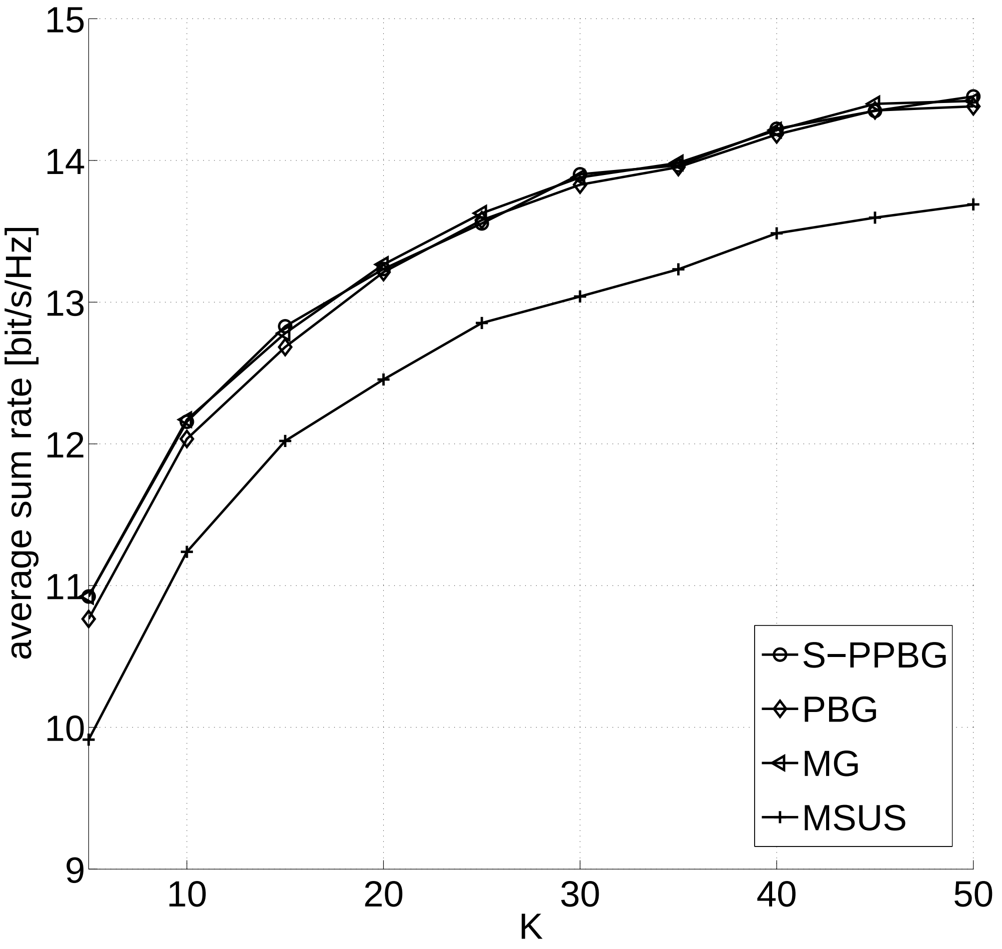

Figure 3.10: Average SR as versus the total number of MTs K.

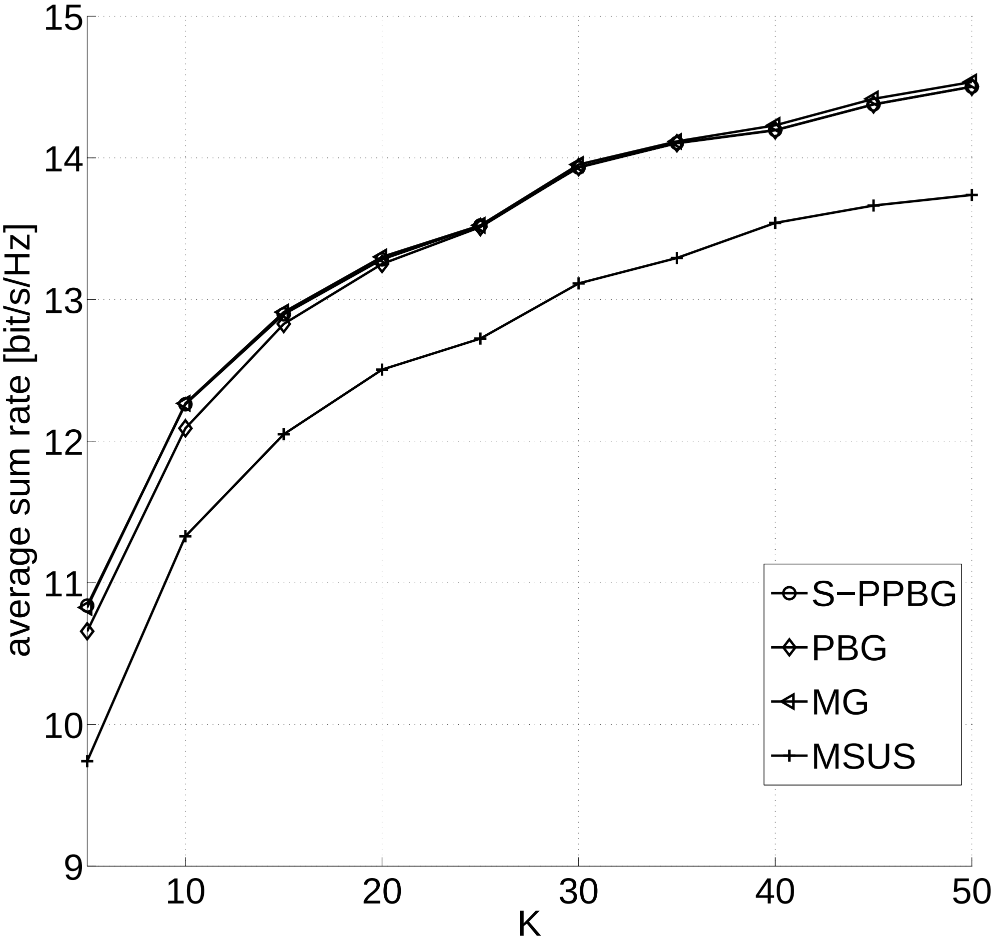

Figure 3.11: Average SR versus the total number of MTs K with PFS.

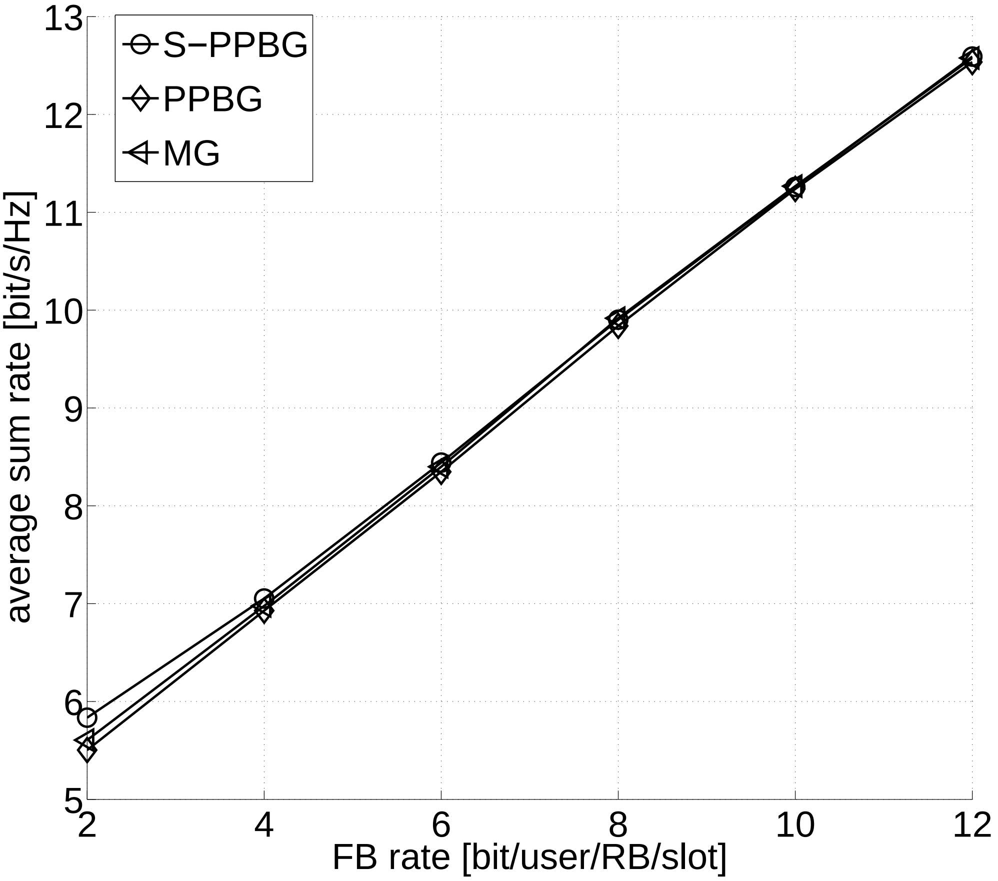

Figure 3.12: Average SR versus per stream FB rate.

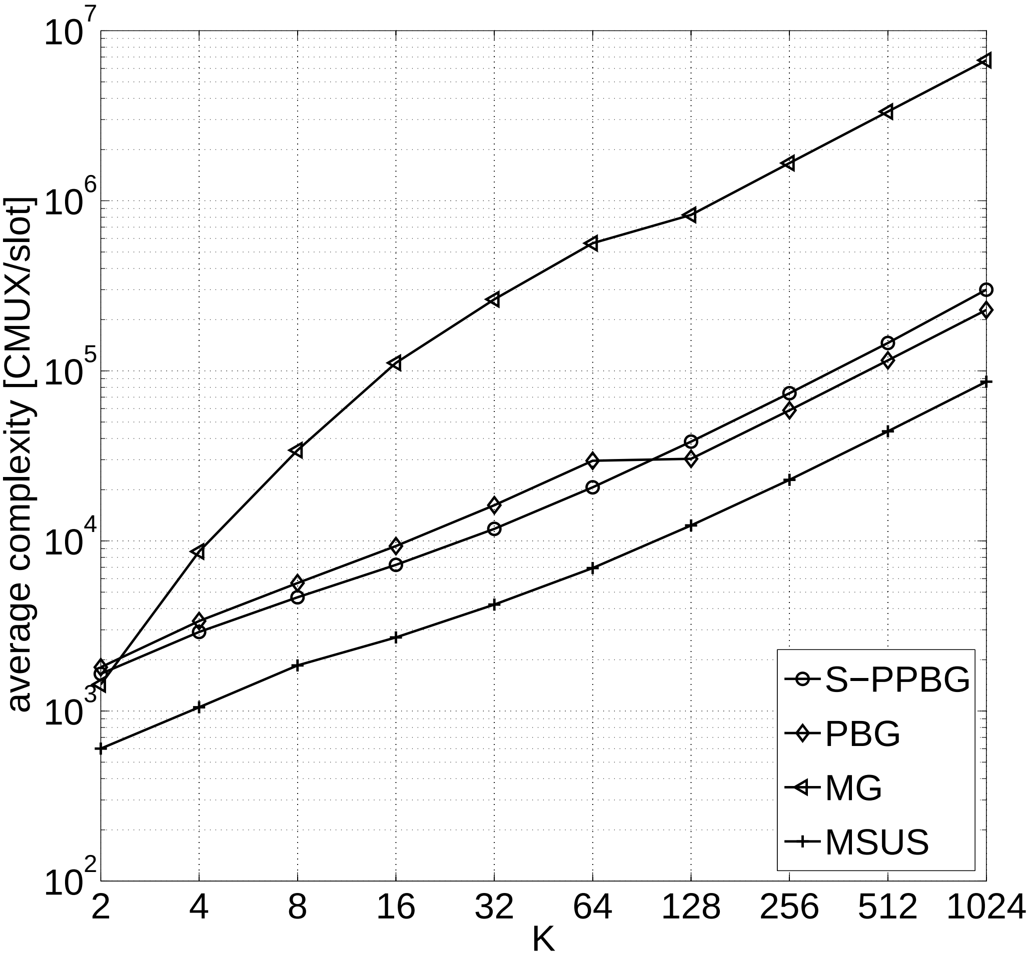

Figure 3.13: Complexity versus K.

At each slot, the scheduling algorithm aims at selecting the set $\mathcal{P}$ of streams that maximizes the weighted system throughput under the constraint that the average probability that the scheduled rate exceeds channel capacity, i.e. the average outage probability, is p_{out}. Each MT k has an associated weight w_k, which takes into account fairness and QoS constraints. In particular, letting $\gamma_{k,c}$ be the estimated SNIR of stream (k, c), we aim at maximizing the weighted system throughput

$$\mathcal{R}(\mathcal{P}) = \sum_{(k,c)\in\mathcal{P}} w_k \log_2(1 + \epsilon_{p_{out}}\gamma_{k,c}) \,, \tag{3.5}$$

where the sum is taken over all streams (k, c) of $\mathcal{P}$, and parameter $\epsilon_{p_{out}} \in [0, 1]$ ensures an average per user outage probability not exceeding p_{out}, [52].

If a stream is affected by outage, i.e, if the allocated rate exceeds the maximum rate available for that stream, due to imperfect channel state information, beamforming and scheduling, the corresponding rate is set to zero. Letting $\beta_{k,c} = 0$ when outage occurs for stream (k, c), and $\beta_{k,c} = 1$ otherwise, the average outage throughput is defined as

$$\mathcal{T}(\mathcal{P}) = \sum_{(k,c)\in\mathcal{P}} \beta_{k,c} \log_2(1 + \epsilon_{p_{out}}\gamma_{k,c}) \,. \tag{3.6}$$

where the sum is taken over all streams (k, c) of $\mathcal{P}$, and parameter $\epsilon_{p_{out}} \in [0, 1]$ ensures an average per user outage probability not exceeding p_{out}, [52].

Fig. 3.14 shows the outage throughput $\mathcal{T}(\mathcal{P})$ as a function of the number of active MTs K with a common outage constraint $p_{out} = 2\%$. We observe that PBG always outperforms MSUS with a gain of about 5%, with a limited increase of complexity. Even the MG algorithm, which provides a performance upper bound in terms of (3.5), is outperformed by the proposed PBG, since also MG is a suboptimal algorithm.

3.2.2 Complexity Comparison

Fig. 3.13 shows complexity versus K. For $K = 2$ to 64 the low K complexity expressions are used, while from $K = 128$ to 1024 we use the high K complexity expressions. We first observe that the complexity ratio between the scheduling algorithms is nearly the same both in the low K and high K regime. As expected, MSUS and S-PPBG complexity trend is not influenced by the value of K. From Fig. 3.13 we note that for $K = 5 \div 50$, with corresponding fully load probability in the range from 1% to 95%, the computational cost of MG is from 2.2 to 18.5 times the

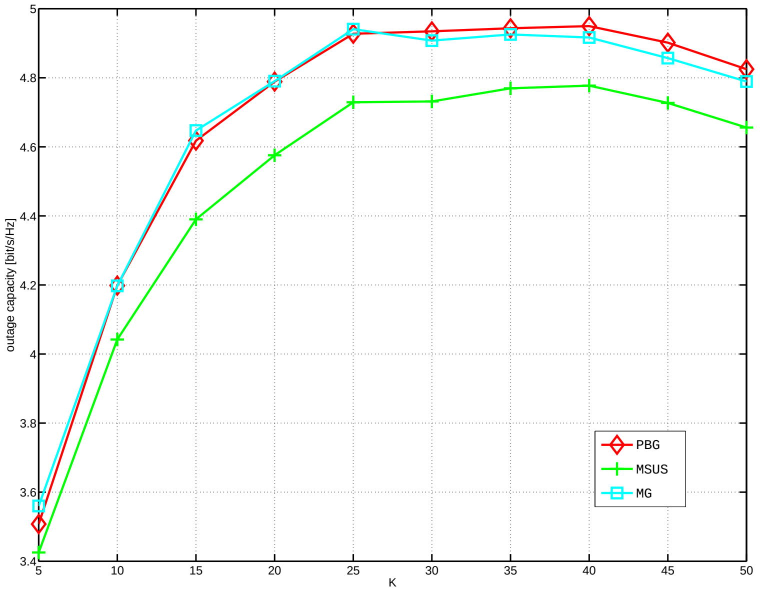

Figure 3.14: Average outage throughput versus the total number of MTs K with proportional fair scheduling and 2% outage probability.

cost of PBG, with a factor increasing in K; as expected, the preselection technique further reduces complexity by a factor $1.2 - 1.4$ with respect to PBG. We note also that complexity of S-PPBG is only $2.4 - 2.9$ times the complexity of MSUS. As complexity of PPBG is bounded between that of PBG and S-PPBG and these two are very close, we omitted to show PPBG in Fig. 3.13.

In the high K scenario, simulations confirm the analysis; in fact, for $K = 400$ we have $\mathbf{C}_{MG} = 2.61 \cdot 10^6$, $\mathbf{C}_{PBG} = 9.4 \cdot 10^4$, $\mathbf{C}_{MSUS} = 3.49 \cdot 10^4$ and $\mathbf{C}_{SPPBG} = 11.9 \cdot 10^4$. We underline that in the high K regime S-PPBG complexity is higher than that of PBG because of the required power distribution; indeed simplification of preselection does not compensate the need of redistributing the total power. On the other hand, we note that the high complexity required by MG is mainly due to the evaluations of BF at each step.

Memory requirements, investigated in Subsection 2.5.1, does not prefigure large differences between different methods; for $K = 400$ memory required locations are 35890 for MG, 29682 for PBG, 29730 for S-PPBG and 33841 for MSUS. Hence, the simplified techniques achieve a reduction of memory requirement with respect to existing algorithms.

Chapter 4

Conclusions

In this first part of the thesis, we focused on MIMO downlink systems with limited feedback, both in SC and in the OFDM scenario. In particular, for a SC scenario, we proposed various channel quantization techniques and feedback strategies based on the Lloyd-Max algorithm [36] that exploit both spatial and time correlation of the MIMO channel. We derived a UD feedback approach where FB bits are accumulated over multiple signalling intervals in order to index a much larger codebook; moreover we proposed new predictive FB strategies where both transmitter and users predict the evolution of the channel vector and users adjusts the prediction by feeding back a quantized version of the prediction error to the transmitter. Furthermore, we described a predictive feedback strategy with unitary rotation matrix, exploiting the geometric properties of unit norm CDI vectors. Finally, we have proposed a MMSE beamformer that takes into account imperfect CSI at the BS and a FB signalling based on the prediction of CDI.

From performance evaluation on SC scenario we conclude that predictive FB outperforms significantly existing techniques in terms of SR and low FB rate; UD is a promising strategy as it provides improved SR with respect to basic FB and does not require channel prediction at both transmitter and receiver side. MMSE-BF is useful when dedicated channels are set up in downlink, while when pure PFS is adopted it provides similar performance to ZF-BF at the cost of an additional CQI parameter.

In MIMO OFDM scenario, we propose suboptimal scheduling algorithms to face the increased dimension of candidate streams set, based on simplified BF evaluation during the user selection process. We addressed the tradeoff between an opportunistic approach in user selection, providing high average sum rate, and quality of service (QoS) requirements, by introducing a general multiuser scheduling, the opportunistic maximum sum rate strategy, and the multicarrier proportional fair scheduling. Furthermore, different user selection strategies are illustrated, and in particular we propose a refined greedy strategy (PBG) requiring a lower complexity. As a further refinement of PBG algorithm, we propose the preselection technique, which reduces the set of candidate users. Complexity analysis is evaluated for each user selection strategy in Section 2.5, both in terms of computational complexity and memory requirements. Simulation results show that the proposed suboptimal algorithm although requires a quarter of the complexity of the comparison algorithm, provides almost the same average sum rate and the same outage throughput. Furthermore, preselection technique applied to the PBG algorithm halves the computational complexity required to PBG by providing the same performance, at the cost of a very little increase of the memory requirements.

Part II

Vital Signs Detection

Main Abbreviations and Notations

AMDF: amplitude maximum difference function;

API: graphic interface;

AV: atrioventricular node;

AWGN: additive white Gaussian noise;

CIR: channel impulse response;

CORR: correlation based estimator;

CW: continuous wave;

EIRP: effective radiated power;

EN: end position for the scan windowing;

FCC: Federal Communications Commission;

HWI: hardware integration coefficient;

IR: impulse radio;

ISI:inter symbol interference;

LCML: low complexity ML

LOS: line of sight;

LRS: locally rich scattering;

MSE: mean square error;

ML: maximum likelihood

L_s: number of samples in a scan;

PC: personal computer;

PMUSIC:Music based detection algorithm;

PPS: pulses per sample;

PRF: pulse repetition frequency;

R: receiver;

RF: radio frequency;

SA: sinoatrial node;

SNR: signal to noise ratio;

ST: start position for the scan windowing;

SWI: software integration coefficient;

T: transmitter;

TD: time domain

ToA: time of arrival;

TEM: transverse electromagnetic wave;

T_P: pulse duration;

T_S: pulse repetition period;

UWB: ultra wide band;

WEIGHTED: weighted autocorrelation function

WELCH: Welch based algorithm.

Introduction

Remote vital signs detection is an emerging topic, whose aim is monitoring a patient vital parameters avoiding physical contact between the patient and the sensor. In fact, a remote monitoring system provides advantages in many scenarios, such as baby monitoring, home monitoring for chronic health diseases and sleep disorders. A remote sensor allows an easier patient monitoring also for long periods of observation. In the last years, different technologies have been proposed with this aim, and in particular: Ka Band, narrowband radar, whose high frequency provides an observable Doppler effect even for low vital signs speeds [53, 54], ultra wide band (UWB) radar [1, 55].

In this work, we focus on radar technologies; in fact, it provides a contactless sensor, easily adaptive to different scenarios. Radar technologies have already been investigated for vital signs detection, for military application and rescue of victims of natural disasters; however, these scenarios allow high values of the transmitted signal, because the remote sensor is used for a short period of time, and it must detect a living person even through walls (e.g., after an earthquake). Home monitoring applications instead are supposed to be used for long periods in an indoor scenario; therefore, for these applications additional constraints have to be taken into account, and in particular the transmitted power has to be limited.

Among all radar technologies, UWB radar provides key advantages, as it relies on ultra-short (nanosecond scale) waveforms that can be free of sine-wave carriers and do not require intermediate frequency (IF) processing because they can operate at baseband. The ultra-short duration of UWB pulses provide unique advantages both for communication and radar applications: i) enhanced capability to penetrate through obstacles; ii) ultra high precision ranging at the centimeter level; iii) potential for very high data rates along with a commensurate increase in user capacity; and iv) potentially small size and processing power. This motivates the increasing interest of the scientific community on the application of UWB radar for vital signs detection [1, 56, 57]. In the second part of the thesis, we focus on vital signs detection using UWB radar in a indoor scenario, and in particular on the model describing the influence of vital signs on the received signal, and on detection algorithms. At the best of the author's knowledge, a complete description of the effect of chest motion on the received signal for a pulse UWB system is not available in the literature. This topic is addressed in Chapter 7, and a description of the effects of vital signs on the signal parameters are provided in Chapter 8. We consider radar device working on the $3.1 - 5.3$ GHz band, which is available for consumer applications according to the Federal Communications Commission (FCC) rules [58]. In this scenario we investigate analytically the parameters of the received signal and their time variations due to vital signs. In particular, we verify in Chapter 7 that the available band does not allow an efficient vital sign detection based on time of arrival (ToA). Most of the proposed detection techniques are based on ToA variations; however, a large bandwidth is required to observe ToA variations due to heart beating. Moreover, detection is made difficult by the non stationary nature of the heart beating and respiration. Therefore, we investigate detection of vital signs based on amplitude and phase modulation of the radar signal, and we propose a novel technique in Chapter 9. The proposed detection technique requires short observation periods, where we can assume vital signs as stationary and periodic. A novel periodicity based detection algorithm is proposed and compared to the correlation based detection algorithm. Chapter 10 provides numerical results in ideal conditions and experimental results. Computational complexity is also evaluated for the various algorithms.

Chapter 5

Ultra Wide Band Radar Technology

UWB radio is an emerging technology inviting major advances in wireless communications, networking, radar, imaging, and positioning systems. The basic idea of UWB is to transmit a signal characterized by a very large bandwidth and a low power spectral density. UWB is defined as a transmission systems with instantaneous spectral occupancy in excess of 500 MHz or a fractional bandwidth of more than 20%; the fractional bandwidth is defined as B/f_C , where B denotes the -10 dB bandwidth, and f_C is the center frequency. Such systems rely on ultra-short (nanosecond scale) waveforms that can be free of sine-wave carriers and do not require IF processing because they can operate at baseband.

In 2002, the Federal Communications Commission (FCC) in the United States of America released a large bandwidth ($3.1 - 10.6$ GHz) for unlicensed use provided emission levels are kept low (< -41.3 dBm/MHz). This new unlicensed band, called UWB, is the largest unlicensed frequency band ever released. The large bandwidth and low power allows UWB radios overlaying coexistent radio frequency (RF) systems to operate using low-power ultra-short information bearing pulses. Similar regulatory processes are currently in progress in many countries worldwide; the research community is currently targeting several UWB applications, e.g. short-range, high-speed broadband access to the Internet, localization at centimeter-level accuracy, high-resolution ground-penetrating radar, through-wall imaging [57].

Despite the recent renewed interest, UWB has a history as long as radio. In fact, the first radio communication system, invented by Guglielmo Marconi more than a century ago (1901), required enormous bandwidth as information was conveyed using spark-gap transmitters. The first UWB radar technology came in the late 1960s, when high sensitivity to scatterers and low power consumption motivated the introduction of UWB radar systems [59]. The ultra-short duration of UWB pulses provide unique advantages both for communication and radar applications: i) enhanced capability to penetrate through obstacles; ii) ultra high precision ranging at the centimeter level; iii) potential for very high data rates along with a commensurate increase in user capacity; and iv) potentially small size and processing power. We denote as *radar* a system whose aim is to detect a target information hidden in the environment by using electromagnetic (EM) waves. As a communication system, a radar system is composed by transmitting and receiving entities; the main difference between communication and radar systems is the aim of the transmission, and the location of the information source. In fact, in a communication system, the information source is connected to the transmitter side, which sends a EM signal to the receiver side in order to communicate the current information symbols. The receiver side has only a statistical knowledge of the transmitted signal, and receives a signal corrupted by noise and channel; from this signal the receiver performs an estimate of the transmitted information symbols. In a radar signal, both transmitter and receiver have a statistical knowledge of the information source. The transmitter sends a EM signal to the receiver, which is perfectly known at the receiver side; in other words, the transmitted signal does not carry any information. The aim is now the observation, at the receiver side, of a hidden information source on the basis of the received signal. In fact, as the hidden information source influences the channel impulse response, the hidden information source can be observed by estimating the channel conditions. Therefore, the receiver performs an estimate of the channel on the basis of the distortion of the received signal parameters, which are due to both channel and noise.

In this Chapter we discuss the UWB radar technology and the motivation for its application to health monitoring, and in particular to human vital signs detection.

5.1 Research Motivation

Health monitoring in general aims at detecting vital parameters of a target, and may involve several applications, e.g. medical instruments, patient home monitoring and presence detection. For different reasons, these application require some main features:

- Unobtrusiveness, i.e. the monitoring system should not interfere with the target usual activities; this feature is essential e.g. for applications requiring long observations of vital parameters, and presence detection. In order to achieve this goal, it is important to address to remote sensing systems, which avoid the direct contact between the target and the sensor.

- Low power: FCC spectral masks pose a severe bound on the transmitting power, which is set on the same order of magnitude as the noise. Consequently, the monitoring system has to deal with low signal to noise ratio (SNR) scenarios.
- High spatial resolution: this is a key feature to correctly locate the target, to properly separate the target from the channel clutters, and to resolve different targets standing nearby.

Detection of human beings with radars is based on movement detection. Heart beating and respiratory motions cause changes in frequency, phase, amplitude and arrival time of the electromagnetic wave reflected by a human being. Both narrowband and UWB technologies can provide a time modulation of these parameters; however, UWB radar has several key advantages over narrowband wave radars, i.e. the high spatial resolution, allowing the resolution of multiple targets and the separation between targets and clutter, a better immunity against multipath interference and interference of coexisting narrowband systems with respect to narrowband technologies.

5.2 UWB Radar

UWB radar for human being detection can be built based on different UWB technologies, which can be clustered into two families: continuous wave (CW) UWB, where the transmitted signal is continuous in time and impulse radio (IR) UWB, where the transmitted signal is a periodic repetition of a UWB pulse. We briefly describe their advantages and disadvantages, and motivate our choice of impulse UWB radar for vital signs detection.

5.2.1 Continuous Wave UWB Versus Impulse Radio UWB

As the name suggests, continuous wave (CW) radar is a radar technique based on a continuous transmitted signal. The UWB nature of the signal can be obtained either in time or in frequency domain; different strategies have been proposed in literature,

e.g. random noise CW radar [60], frequency modulated continuous wave (FMCW) radar and stepped-frequency continuous wave radar.
The main features of CW radar are:

- the transmitted power is uniformly distributed in time;
- the modulation waveforms are not supposed to have short duration, since the large bandwidth is provided by signal modulation;
- with a proper signal modulation, it is possible to cover all the band allowed by the FCC regulations.

On the other hand, the simplest way to obtain a UWB transmitted signal is a periodic repetition of a short pulse, where the repetition period is longer than the channel impulse response (CIR); also in this case, pulse modulation can be performed. The main features of this transmitting system are:

- the transmitted power is concentrated on a very short period;
- usually not all the FCC band is covered, because generating a pulse of about 0.1 ns duration is not cost effective;
- CIR is easily obtained, as it is completely described in a pulse repetition period.

5.2.2 IR -UWB Radar

We consider an Impulse Radio - Ultra Wide Band (IR-UWB) system for the detection of vital signs of a target in an indoor environment. The transmitted signal is

$$s(t) = \sum_{n=-\infty}^{+\infty} p(t - nT_S)\cos(2\pi f_C t + \phi_0), \tag{5.1}$$

where $p(t)$ is the UWB pulse wave with duration T_P, f_C is the central frequency and T_S is the pulse repetition period. The bandwidth B_P is the inverse of T_P, i.e. $T_P = \frac{1}{B_P}$.
Let $h(t)$ be the channel impulse response, which includes the indoor channel paths, and the effects of target (attenuation, reflections, movements, respiration and heart beating); let also P_t be the power of the transmitted signal $s(t)$ and $\eta(t)$ be the

zero mean additive white Gaussian noise with power σ_η^2. At the receiver side, the resulting signal is

$$r(t) = \int_{-\infty}^{+\infty} s(t-\tau)h(\tau)d\tau + \eta(t). \tag{5.2}$$

We suppose that the shape of the transmitted wave $p(t)$ is perfectly known by the receiver. Then the receiver signal $r(t)$ provides an estimate $\hat{h}(t)$ of the channel impulse response, under the following conditions:

- the pulse repetition period has to be equal to or higher than the pulse duration T_P, i.e. $T_S \geq T_P$;
- in order to guarantee a correct reconstruction of the CIR, the sample theorem requires the sampling frequency F_c to be equal to or higher than the system bandwidth, i.e. $F_c \geq B_P$, or $T_c \leq T_P$, where T_c is the sampling period;
- inter pulse repetition interval interference (ISI) avoidance requires the channel duration $T_l = LT_c$ is smaller than the pulse repetition period, i.e. $LT_c \leq T_S$.

Chapter 6

Vital Signs

In this chapter we define vital signs and characterize the interaction between the UWB signal and the target. In particular, Section 6.1 describes vital signs, respiration and heart beating. In Section 6.2, a model for thorax tissues is introduced and an analytical model for the signal reflected by the target is discussed. Finally, in Section 6.3 a frequency domain characterization of thorax tissues is derived.

6.1 Vital Signs Description

We denote as *vital signs* a set of biological processes, providing information on the state of a living person (*target*); these signs are supposed to characterize all living human beings, and their values or variation are supposed to describe the state of the target.

In general, the main processes described by this definition are those derived by respiration and heart beating, e.g. chest oscillation, periodic heart compression and rapid changes of pressure into veins and arteries. In particular, we focus on the subset of vital signs that can be inferred by their external effects. We describe in the following respiration and heart beating, and we discuss their correlation.

6.1.1 Respiration

Respiration is a complex physiological process whose aim is to ensure both the proper income of oxygen and the disposal of dangerous gases, in particular the carbon dioxide, resulting from the respiration process at cellular level. The amount of oxygen required, and consequently, of waste respiration products to be ejected, is determined by the conditions of the body: physical features (age, gender, weight, etc.) and current activities and feelings (sport, fun, fear, relax). The frequency of the respiration cycle, denoted as *respiration rate*, and the deepness of breathing, i.e., the amount of air inhaled per cycle, is influenced by body conditions, but also by external conditions (e.g., pressure of the air and its composition), and by conscious control, performed to temporarily adapt breathing to other activities such as swimming, or talking. In general, respiration is not a stationary process; in fact, parameters as duration, deepness, proportion inspiration/expiration periods, in general change from one respiration cycle to the next one. Therefore, we may be interested in either a real time estimate of the target respiration rate, or on an estimate of its average.

6.1.2 Heart Beating

The heart is a muscular organ responsible for pumping blood throughout the blood vessels by repeated, rhythmic contractions. Blood is conveyed by the great vessels (pulmonary trunk, aorta, and superior vena cava) to and from body tissues. The heart's rhythmic contractions occur spontaneously, although the rate of contraction is influenced by nervous or hormonal activity, exercise and emotions. The rhythmic sequence of contractions is coordinated by the sinoatrial (SA) and atrioventricular (AV) nodes. The sinoatrial node is located in the upper wall of the right atrium and is responsible for the wave of electrical stimulation that initiates atrial contraction by creating an action potential. The wave reaches then the AV node in the lower right atrium, where it is delayed to allow enough time for all of the blood in the atria to fill their respective ventricles, and then it propagates, leading to a contraction of the ventricles [61].

Due to these electrical signals, atria and ventricles alternately contract and relax in a rhythmic cycle; a single cycle begins and ends with atria and ventricles relaxed. During the first stage, diastole, the blood flows into the right and left atria; due to the open valves between the atria and ventricles, blood flows through to the ventricles. Ventricles are then filled with the atrial contraction, due to the SA electrical signal. The second stage is called systole and represents the ventricular contraction and the ejection of blood from the ventricles to the vessels; in particular, the right ventricle sends blood to the lungs via the pulmonary artery, while the left ventricle pumps blood to the aorta. During this stage the valves between the atria and ventricles are closed. One complete sequence of diastole/systole is called a cardiac cycle, or heartbeat. The heart rate range is very wide: in fact, the lowest heart rate reported in literature for and adult target is 45 beats per minute (bpm), while the highest is about 250.

6.1.3 Correlation Between Respiration and Heart Beating

In general, respiration influences the heart beating process [62]; a close nonlinear coupling exists between the respiratory and cardiovascular systems. In addition to this, we observe that both respiration and heart beating are influenced by the target activity; in other words, the state of the target introduces a correlation between the two processes. However, at the best of the author's knowledge, there is no simple model describing the correlation between the two processes, and therefore in the following we consider respiration and heart beating as independent processes.

6.2 Thorax Tissues Description and Signal Propagation

In a monitoring system, vital signs provide an appreciable modulation of the monitoring signal when it interacts with the target; clearly, the modulation of a process on the monitoring signal is not only due to the process itself, but it depends on the system used to observe it. This motivates the following investigation on the effects of a radar pulse on human tissues; based on this model, a feasibility study is performed in Section 7.4. We focus on thorax tissues, since both respiration and heart beating affect mainly this region of the body. Furthermore, other regions of interest, like neck and abdomen, are characterized by the same external tissues, and, as it is shown in the following, the UWB signal is influenced only by the outer tissues; then, from the radar system perspective, their contributions can be modeled in a similar way.
We assume that

- the pulse is a Transverse Electromagnetic (TEM) wave;
- the pulse impacts the thorax with a normal incidence angle;
- the target chest behaves as a single point reflector;
- all interfaces are planar.

When a TEM plane wave propagating in a homogeneous medium 1 encounters a planar interface with a different medium 2, a portion of the wave is reflected from the interface while the remainder of the wave is transmitted. The reflected and transmitted waves can be determined by enforcing the fundamental electromagnetic field boundary conditions at the media interface. Since the thorax tissues satisfy the condition of good dielectric [63], we can use the approximated expressions for the amplitude attenuation. Defining σ as the conductivity of medium, ε as the dielectric permittivity and μ as the magnetic permeability, the amplitude attenuation (in m^{-1}) can be written as

$$\tilde{\alpha} \cong \frac{\sigma\sqrt{\mu}}{2\sqrt{\varepsilon}}, \tag{6.1}$$

and the intrinsic impedance (in Ohm, Ω) is

$$\tilde{\eta} \cong \sqrt{\frac{\mu}{\varepsilon}}. \tag{6.2}$$

Under these assumptions, at the interface between medium 1 and medium 2 a *transmitted* and a *reflected* wave are generated, having the same wave shape of the incident wave, and relative amplitude given by the amplitude transmission coefficient and the amplitude reflection coefficient, respectively. Assuming that the incident wave is z-directed and x-polarized, and that the planar media interface is located on the x-y plane, the incident, transmitted and reflected waves can be illustrated by Fig. 6.1. Let us indicate with a_x, a_y and a_z the unit vectors lying on direction x,y, and z, respectively. We define also E_0 as the amplitude of the electric field on the interface ($z = 0$), t as the amplitude transmission coefficient and r_c as the amplitude reflection coefficient. In particular, the reflection coefficient is given by

$$r_c = \frac{\tilde{\eta}_2 - \tilde{\eta}_1}{\tilde{\eta}_2 + \tilde{\eta}_1}, \tag{6.3}$$

where $\tilde{\eta}_{1,2}$ is the intrinsic impedance of medium $1, 2$.

The ratio between the reflected power P_r and the transmitted power P_t is the *reflected power ratio*,

$$R = |r_c|^2. \tag{6.4}$$

Let $P_{T,1}$ be the power of the wave incident on medium 1 and z_1 be the thickness of medium 1. At the medium interface the reflected power is

$$P_{1,2}^{(R)} = P_{T,1} R e^{-2\tilde{\alpha}_1 z_1} \tag{6.5}$$

The refracted wave amplitude is given by the transmission coefficient

$$t = \frac{2\tilde{\eta}_2}{\tilde{\eta}_2 + \tilde{\eta}_1}, \tag{6.6}$$

while the relative refracted power ratio is

$$\tilde{T} = 1 - R = \frac{\tilde{\eta}_1}{\tilde{\eta}_2}|t|^2. \tag{6.7}$$

The power of the wave refracted in medium 2 is

$$P_{1,2}^{(T)} = P_{T,1}\tilde{T}e^{-2\tilde{\alpha}z_1}. \tag{6.8}$$

We observe that the relative transmitted and reflected power have the same value also for a wave propagating from medium 2 to medium 1, providing a reflected wave in medium 2 and a refracted wave in medium 1. The phasor fields associated with the incident wave are

$$\begin{aligned} E_i &= E_0 e^{-\tilde{\alpha}_1 z} a_x \\ H_i &= \frac{E_0}{\tilde{\eta}_1} e^{-\tilde{\alpha}_1 z} a_y, \end{aligned} \tag{6.9}$$

while for the transmitted wave we have,

$$\begin{aligned} E_t &= tE_0 e^{-\tilde{\alpha}_2 z} a_x \\ H_t &= t\frac{E_0}{\tilde{\eta}_2} e^{-\tilde{\alpha}_2 z} a_y, \end{aligned} \tag{6.10}$$

and for refracted wave we have,

$$\begin{aligned} E_r &= r_c E_0 e^{\tilde{\alpha}_1 z} a_x \\ H_r &= r_c\frac{E_0}{\tilde{\eta}_1} e^{\tilde{\alpha}_1 z} a_y. \end{aligned} \tag{6.11}$$

Denoting with f the frequency of the transmitted signal, the wavelength of the signal propagating in medium 1 with refraction index n_1 is

$$\lambda_1 = \frac{v_1}{f} = \frac{c}{n_1 f} = \frac{\lambda_0}{n_1}, \tag{6.12}$$

where λ_0 is the wavelength of the signal propagation in vacuum, v_1 indicates the wave speed in medium 1, and c is the speed of light in vacuum. Fig. 6.3 shows the wavelength of a pulse in the tissues of thorax, according to [64]; in Fig. 6.2 the relative permittivity $\epsilon_r = \epsilon/\epsilon_0$ of these tissues is described as a function of frequency. We observe that in the UWB band both the relative permittivity and the wavelength are not significantly changing. Therefore, in the following we describe the power of

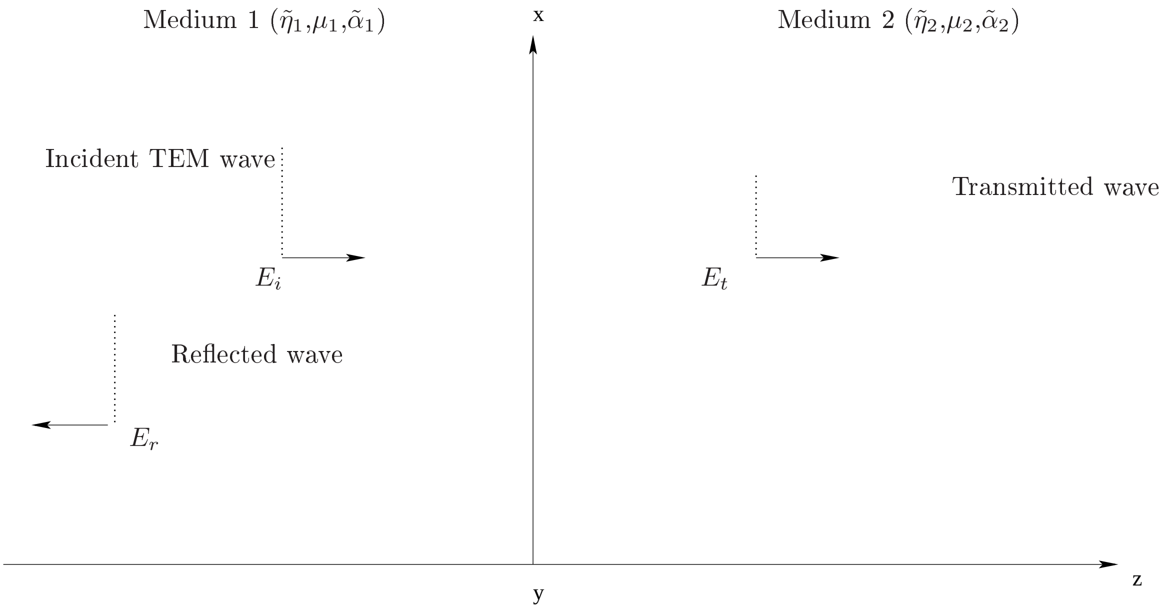

Figure 6.1: Transmitted and reflected waves generated by a planar interface between medium 1 and 2 when a TEM wave with polarization in x direction is normally incident on the interface.

the signals reflected by each interface considering only the frequency 4 GHz, which is the central frequency of the operational band of our UWB device.

The thickness of the thorax tissue layers, where the pulse propagates, are given in Tab. 6.1 from [1].
We denote the interfaces of tissues with numbers: air-skin interface is interface 1, skin-fat interface is interface 2, fat-muscle is interface 3, muscle-cartilage is interface 4, cartilage-lung is interface 5, up to lung-heart interface 6; similarly, the parameters related to each interface are in the following denoted with the corresponding interface number, i.e. R_i for the reflected power ratio and T_i for the corresponding refracted power ratio. We indicate also the tissues by numbers, as described in Tab. 6.1 Air is medium 0. By this notation, each interface has the number of the second medium.

Using the dielectric properties of tissues at 4 GHz, we derive that each media interface provides a reflected signal, whose power and delay depend on the tissues that crossed in its path. We assume that before the air-skin interface 1 we have a signal whose power is P_0; then, the power of the signal reflected from interface

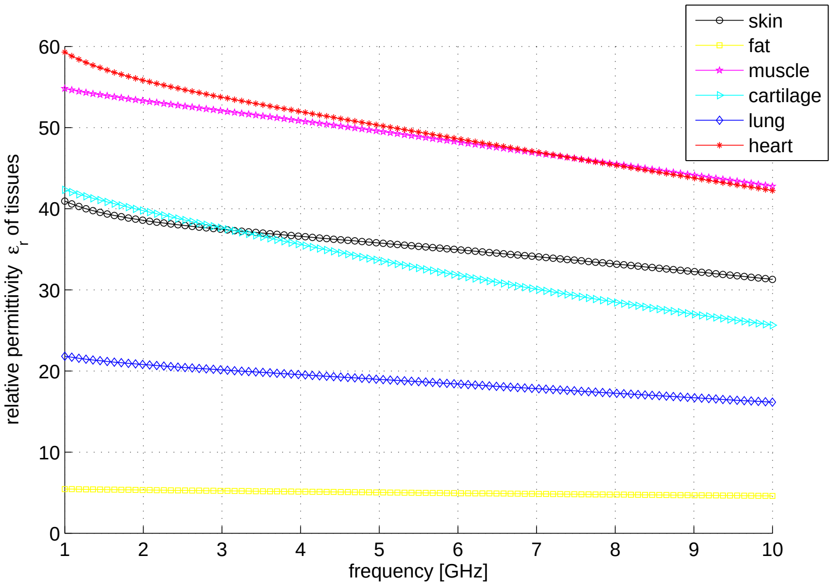

Figure 6.2: Permittivity of tissues from 1 GHz to 10 GHz [1].

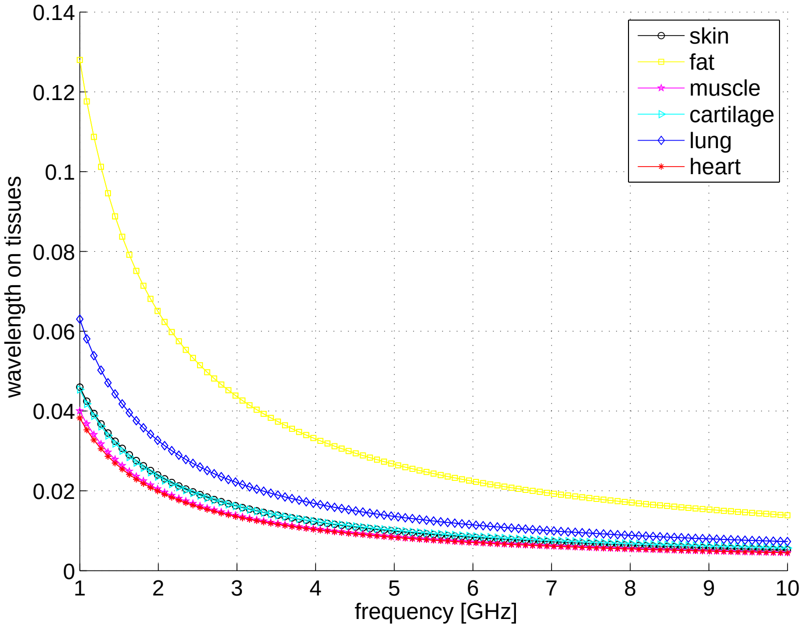

Figure 6.3: Wavelength of tissues from 1 GHz to 10 GHz [1].

Tissue	Tissue number	Thickness [cm]
Skin	1	0.1
Fat	2	0.96
Muscle	3	1.35
Cartilage	4	1.16
Lung	5	0.578

Table 6.1: Thickness of the inner tissues in the thorax [1].

$i \in \{0, \cdots, 6\}$ is

$$P_{r,i} = P_0 R_i \prod_{k=1}^{i} \left[T_k e^{(-2\tilde{\alpha}_k(f) z_k)}\right]^2 = P_0 R_i \prod_{k=1}^{i} \left[(1 - R_k) e^{(-2\tilde{\alpha}_k(f) z_k)}\right]^2 . \tag{6.13}$$

Therefore, we can define the received to incident power ratio (RIPR) Γ_i of the reflected signal of interface i at the target chest surface as

$$\Gamma_i = \frac{P_{r,i}}{P_0} = R_i \prod_{k=1}^{i} \left[(1 - R_k) e^{(-2\tilde{\alpha}_k(f) z_k)}\right]^2 . \tag{6.14}$$

This parameter represents the gain (with $\Gamma_i < 1$) of the signal from the transmitter to the receiver. Ideally, Γ_i is the power level of the signal provided by interface i seen by a on body receiver when $P_0 = 0$ dB. As described in Fig. 6.4 for a transmitted signal of frequency 4 GHz, at the receiver we get

- a signal with RIPR of -2.8977 dB and a delay of 6.67 ns, due to the air-skin interface;
- a signal with RIPR of -13.08 dB and a delay of 6.67 ns, due to the skin-fat interface;
- a signal with RIPR of 17.47 dB and a delay of -6.8 ns, due to the fat-muscle interface.

The signals reflected by muscle-cartilage, cartilage-lung and lung-heart interface are characterized by a lower RIPR, namely -57.38 dB, -72.20 dB and -74.59 dB, and therefore they can not be detected by the receiver.

The dielectric properties of the tissues in [1] refer to a narrowband signal; by considering the UWB pulse as a sum of narrowband signals, we deduce that the received

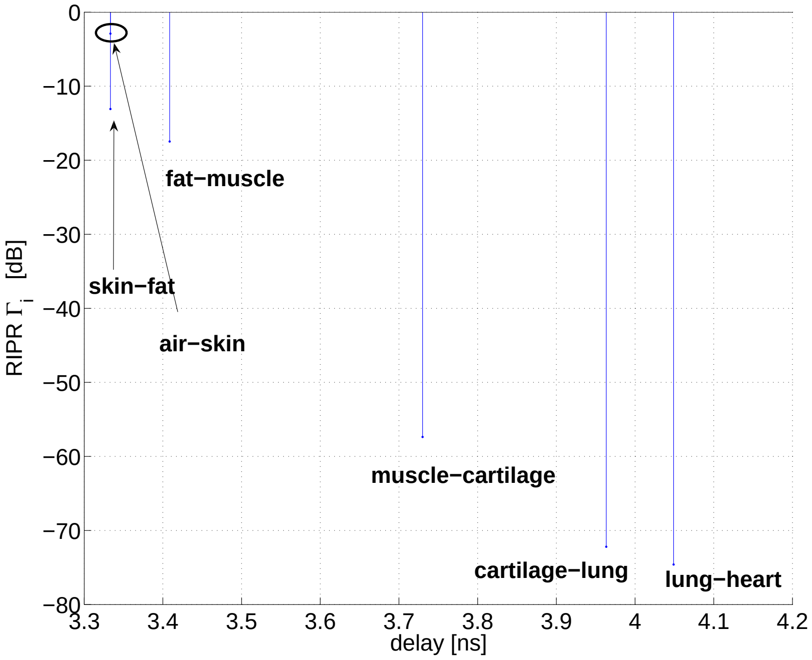

Figure 6.4: Reflected pulses from the target thorax tissues at a central frequency of 4 GHz

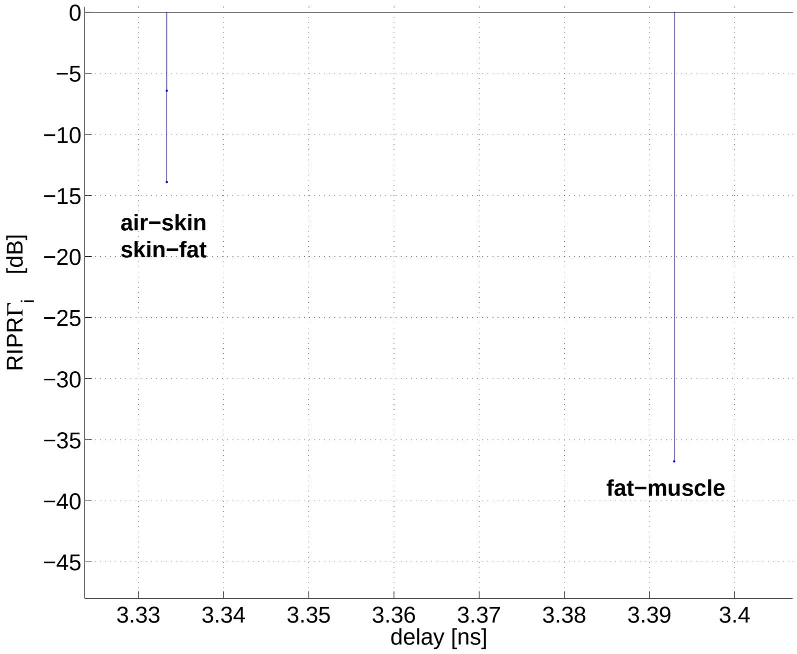

Figure 6.5: Reflected pulses from the target thorax tissues at a central frequency of 60 GHz

signal has not the same shape as the transmitted one, since the tissues introduce a frequency selectivity on the reflected signal. We also note that we are not able to distinguish all these signals since the corresponding delays differ only by about 0.1 ns, requiring a minimum bandwidth of about 10 GHz to resolve them.Finally, we show in Fig. 6.5 the average RIPR of the signals reflected by tissues for a signal in the Ka band, at 60 GHz; we note that at those frequencies, and with a severe constraint on transmitting power we are not able to detect that signals except the one reflected from the skin interface, whose RIPR is 6.4 dB).

6.3 Frequency Domain Characterization of Tissues for a UWB System

We introduce a frequency domain characterization of thorax tissues for a UWB system, in order to characterize the reflection provided by the second interface. In particular we focus on the fat tissue, since from Section 6.2 we don't expect to receive replicas from inner tissues. In particular, to validate the analysis performed till now, we investigate

- the wavelength of the signal propagating on the fat tissue as a function of frequency. In fact, the wavelength affects the propagation speed, and if this parameter depends on frequency, the received pulse would be affected by distortion; in other words, we are verifying if the received replica is a UWB pulse as the transmitted one;
- the received to incident power ratio of the inner and outer reflection (fat-muscle and skin interfaces, respectively) as a function of the frequency, in order to state if there is a frequency selectivity due to propagation and reflection on chest tissues.

6.3.1 Wavelength of Signal Propagating in the Fat Tissue

The wavelength of the signal propagating in the fat tissue λ_{fat} as a function of frequency has been measured and results are reported in [1]. Fig. 6.6 shows the measured wavelength behavior, a linear approximation and a hyperbolic approximation of the measured data, i.e. $\lambda(f) \approx \frac{\lambda(f_C)f_C}{f}$. We see that the hyperbolic function provides a good approximation of the real function, with a mean square error MSE of $5.5e-8$. This motivates the application of this approximation to evaluate the propagation speed as a function of frequency, providing

$$v(f) = f \cdot \lambda(f) \approx \lambda(f_C)f_C. \tag{6.15}$$

By the hyperbolic approximation of the wavelength in fat tissue we expect the propagation speed to be approximately constant in the fat tissue, and therefore the inner reflected signal is not affected by distortion due to a frequency selectivity of the time of arrival (ToA). The outer reflection propagates only on the air, where the propagation speed is approximately the light speed in vacuum, c.

6.3.2 Received to Incident Power Ratio of the Inner and Outer Reflections

In a UWB system, also the RIPR defined in (6.14) is in general a function of the frequency, as it depends on the impedance of the media. The expression of the RIPR

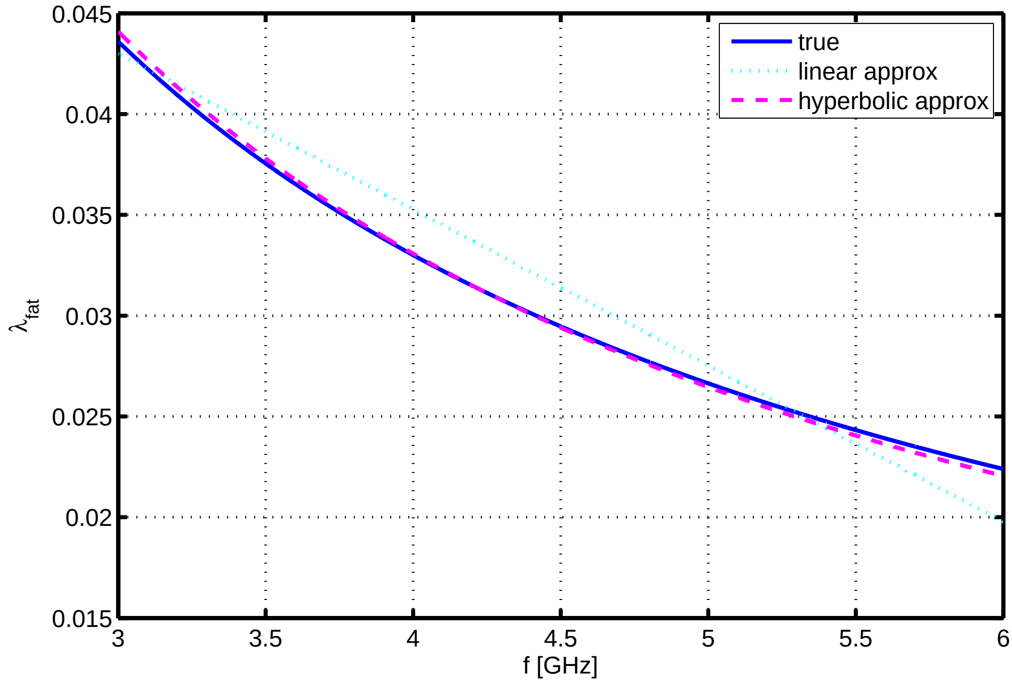

Figure 6.6: Wavelength of a signal propagating in the fat tissue as a function of frequency.

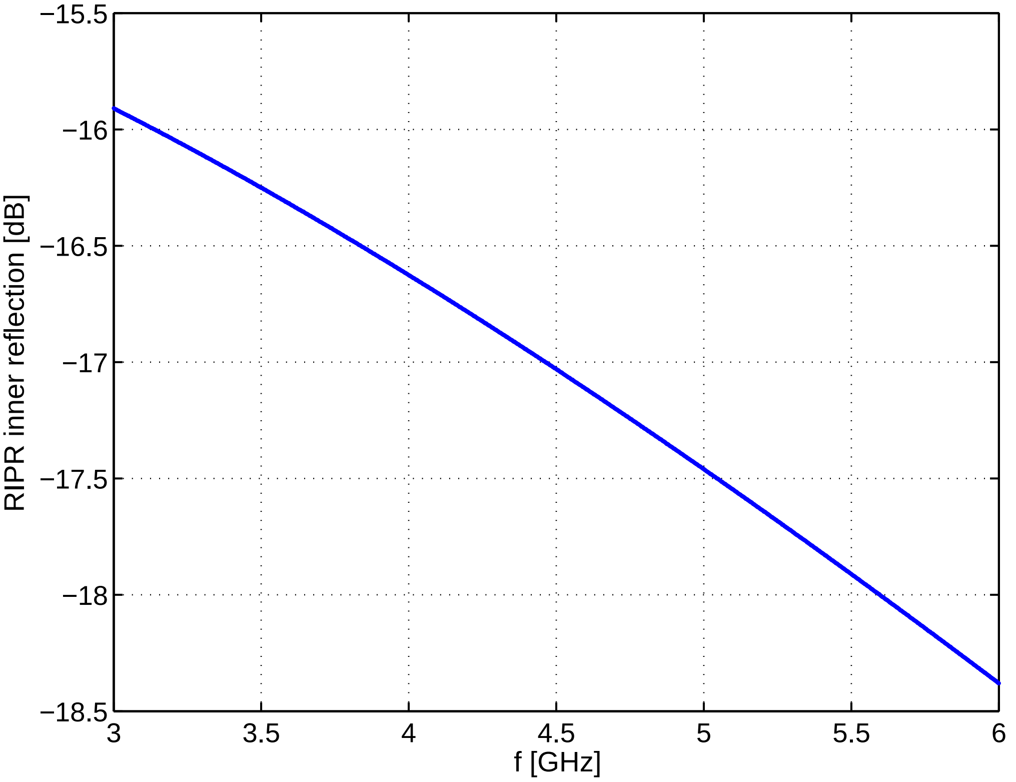

Figure 6.7: Received to incident power ratio of the inner reflection.

of the inner reflected signal can be written from (6.14) as

$$\Gamma_3(f) = \left[(1-R_1)e^{(-2\tilde{\alpha}_1(f)z_1)}(1-R_2(f))e^{(-2\tilde{\alpha}_2(f)z_2)}\right]^2 R_3(f), \tag{6.16}$$

while for the outer reflection we have

$$\Gamma_1(f) = R_1(f). \tag{6.17}$$

We don't consider here the signal provided by the skin-fat interface, Γ_2, as it has the same ToA of the air-skin interface signal and it is 13 dB weaker. Figs. 6.7 and 6.8 show the RIPR for the inner and outer reflection as a function of frequency of the radar pulse.

We observe from Fig. 6.8 that the RIPR of the outer signal is about +2.9 dB on the band of interest of our UWB device (3-5 GHz), while the inner reflected signal shows in Fig. 6.7 a stronger dependence on the frequency. However, the UWB

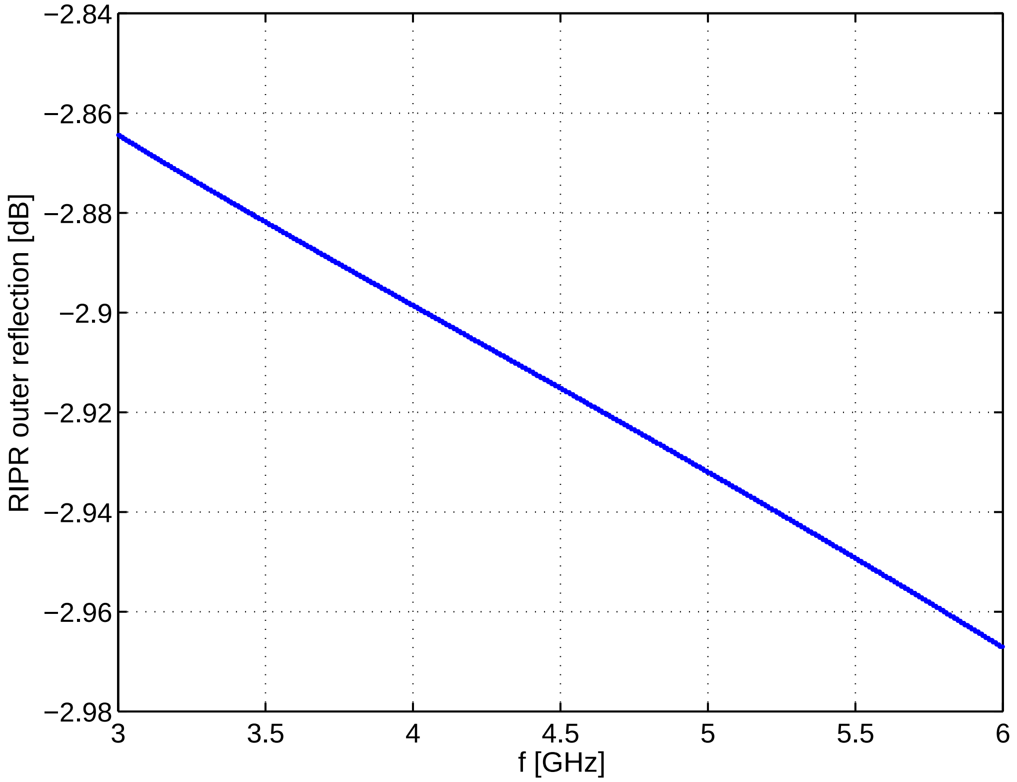

Figure 6.8: Received to incident power ratio of the outer reflection.

system is not able to resolve the two signals, and the outer signal is supposed to be about 14 dB stronger than the inner one; therefore, it is reasonable to assume that the global received signal is not affected by distortion due to frequency selectivity of the body. On the other hand, in the last paragraph we observed that also the propagation speed on the fat tissue can be approximated as a constant in the band of interest. Therefore, we will assume that the received signal reflected by a point scatterer is an UWB pulse with the same shape of the transmitted pulse.

Chapter 7

Channel Model

In the following, we describe the indoor channel model for a UWB signal; in Section 7.1 we introduce the components of the indoor channel model in presence of a target. The effects of the presence of a living target as a scatterer are investigated in detail in Section 6.2. Based on this, we derive a model describing how the received signal is modulated by the vital signs in Section 7.3.

7.1 Indoor Channel Description

We assume an indoor environment with a single still target. We assume that the target is situated at a random distance d_t uniformly distributed in the range $[d_{min}, d_{max}]$, i.e. $d_t \in \mathcal{U}[d_{min}, d_{max}]$ from the transmitter, while the receiver is at distance r from the transmitter. Both transmitting and receiving antennas are supposed to be omnidirectional, then the signal propagates isotropically.

As illustrated in Fig. 7.1, the channel impulse response is composed by different elements, i.e.

- $h_{env}(t)$, the indoor environment impulse response;
- $h_T(t)$, the direct target path;
- $h_{T,env}(t)$, the impulse response of non-direct paths due to the target
- $h_m(t)$, the impulse response due to little target motions.

$$h(t) = h_{env}(t) + h_T(t) + h_{T,env}(t) + h_m(t). \tag{7.1}$$

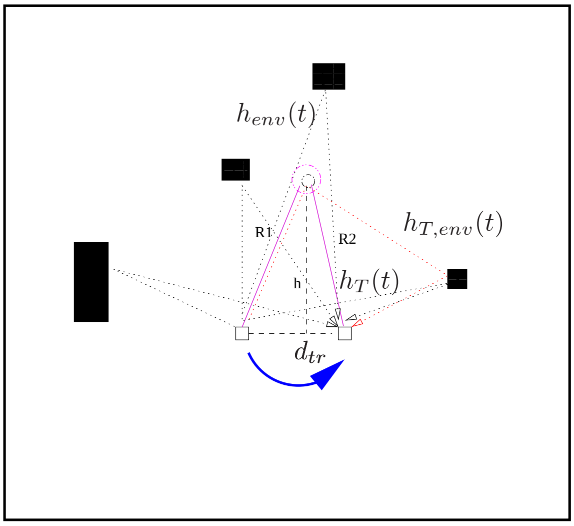

Figure 7.1: Scenario of a UWB radio transmitting in a room with a target

In the following we describe each of these elements and discuss their contribution on the detection of vital signs.

7.1.1 Direct Target Path

The set of direct paths is denoted as $h_T(t)$; channel paths composed by the transmitter, the target and the receiver belong to $h_T(t)$. The delay of these paths is limited to a range which depends on the round trip distance. By performing a Doppler estimation analysis as described in Section 8.1.1, $h_T(t)$ provides information about heart beating and respiration rate. However, $h_T(t)$ may also be affected by spurious Doppler effects, induced by target motions, such as speech and movements of hands and head, in the same delay range; these Doppler components may be modeled in order to compensate their effects.
The main features of this component of the channel impulse response are:

- time variant
- fixed range of delays.

7.1.2 Environment

$h_{env}(t)$ is the traditional indoor channel impulse response; it takes into account the effects of the environment without the presence of the target. It is a stationary process with a long coherence period, and involves cross talk path, and multipath due to the room. Since it does not involve the target, it is not useful to the vital signs detection; we model it as the sum of a constant and a Rayleigh fading indoor channel model. The main features of $h_{env}(t)$:

- time invariant
- large range of delays.

In the following, we assume that the receiver is able of perfectly estimating and canceling all the replicas referring to the static part of the channel; scientific literature provides algorithms aiming at the *background subtraction*, e.g. [65, 66].

7.1.3 Multipath Involving the Target

$h_{T,env}(t)$ contains the non direct paths involving the target. This paths are characterized by an higher delay and attenuation w.r.t. the direct path $h_T(t)$. As for all paths involving the target, we can recognize it by the presence of Doppler components, as the presence of vital signs introduces a time variation on the main parameter of the received signal. The main features of $h_{T,env}(t)$ are:

- time variant
- a range of delays larger then the direct path
- higher attenuation compared to the direct path.

7.1.4 Target Motions

Besides the vital signs, with high probability the target introduces variations on the received replicas due to little movements (e.g. moving the head, coughing, moving the hands...). The effects of the spurious target motions (small movements) are taken into account by $h_m(t)$. This channel component is characterized by i) time variation, and ii) by delays in general not included in the direct target path delay range. Note in fact that in general little movements involve peripheral parts of the body, e.g. the head and the limbs, while the chest is involved with a lower probability.

7.2 Geometric Channel Model

We consider in the following only the direct target path, and how it is influenced by the vital signs. We assume the target as a point, ideal reflector. Therefore, we do not consider the effect of the target motion and multiple reflections involving the target. As stated previously, the other channel components differ from the direct path for some parameter, and in particular time variance, and delay range. Background subtraction allows the cancellation of the static components, while a windowing on the delays of the channel impulse response allows focusing only on the direct path delay range. Considering only the outer reflection, the received signal is given by

$$r_T(t) = h_T(t)p(t - \tau(t)) \cos(2\pi f_C t + \phi_0) + \eta(t), \tag{7.2}$$

where $\tau(t) = \dfrac{d(t)}{c}$ is the delay of the target path, $d(t)$ is the round trip distance (transmitter-target-receiver) and c is the speed of the light in the air. In the following, we describe $d(t)$, and we discuss on the effects of vital signs on the amplitude, delay and phase of the received signal.

7.2.1 Round Trip Distance $d(t)$

We first consider the signal reflected by the air/skin interface; this signal is affected by the chest surface oscillations, due to both respiration and heartbeat. In Fig. 7.2 a detail of the target chest motion is described; the two paths between the transmitter (T) and the receiver (R) indicate the wave path in two different times through the target, O (average chest position) and A (generic chest position). In particular, the path $\overrightarrow{TOR}$ has length $d(t) = R_{tx,0} + R_{rx,0}$ under the condition of deflated lungs, while the path $\overrightarrow{TAR}$ has length $d(t) = R_{tx}(t) + R_{rx}(t)$ at a generic instant t.

We model the chest motion as the sum of the oscillation due to respiration, $x_r(t)$, and the weaker oscillation due to the heart beating, $x_h(t)$, i.e.

$$x(t) = x_r(t) + \xi x_h(t) \tag{7.3}$$

where $\xi < 1$ is an attenuation parameter which underlines the weakness of the heart beating signal on the chest with respect to the respiration signal.

The oscillation $x(t)$ covers the segment AO, i.e. the segment between the average chest position O and the current chest position A, forming an angle θ with the TO segment, as illustrated in Fig. 7.2, and influences both $R_{tx}(t)$ and $R_{rx}(t)$

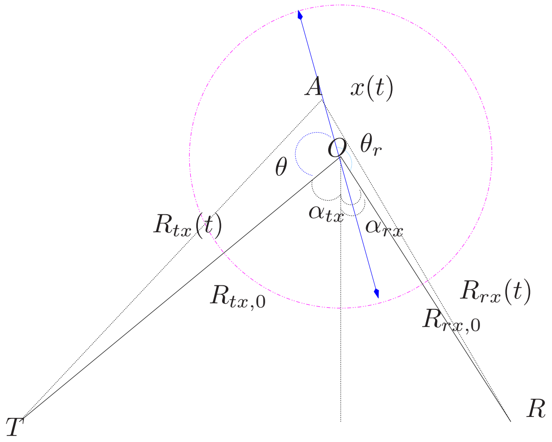

Figure 7.2: Detail of the target chest oscillation due to breathing

Then we define

$$\Delta_{tx}(t) = R_{tx}(t) - R_{tx,0} \tag{7.4}$$

and

$$\Delta_{rx}(t) = R_{rx}(t) - R_{rx,0}. \tag{7.5}$$

Their value depends on the chest motion $x(t)$ of (7.3), on the oscillation angle θ and on the angles $\alpha_{tx} = \widehat{TOy}$ and $\alpha_{rx} = \widehat{yOR}$, where y is the axis of the height of triangle TOR related to the segment TR. The direction of the chest oscillation is indicated by the (blue) arrow, while the (magenta) circle indicates the maximum amplitude.

Generic Bistatic Scenario

We consider the generic bistatic configuration, where the transmitter and the receiver are two different devices; an alternative configuration is the monostatic, where the transmitter and the receiver are located in the same device. By applying the trigonometric rules to the triangle TOA we have

$$R_{tx}(t) = \sqrt{R_{tx,0}^2 + x^2(t) - 2R_{tx,0}x(t)\cos(\theta)}; \tag{7.6}$$

similarly, observing that $\theta_r = 2\pi - \alpha_{tx} - \alpha_{rx} - \theta$ we have

$$R_{rx}(t) = \sqrt{R_{rx,0}^2 + x^2(t) - 2R_{rx,0}x(t)\cos(\theta + \alpha_{rx} + \alpha_{tx})}. \tag{7.7}$$

We derive here $R_{rx,0}$ from the other system parameters; then, we will find the range of angles describing the target area for a given distance range. Referring to Fig. 7.2, we assume to know the parameters:

- α_{tx} and α_{rx} are determined by the positions of T,R and O, and on the directivity of antennas. In our scenario, antennas are omnidirectional;
- $d_{tr} = |\overrightarrow{TR}|$ is fixed as part of the set up;
- $h_0 = d(O, \overrightarrow{TR})$ is the distance of the target to the transmitter-receiver segment.

The following constraints have to be satisfied:

- $R_{tx,0} \sin(\alpha_{tx}) = h_0$;
- $R_{rx,0} \sin(\alpha_{rx}) = h_0$;
- $R_{tx,0} \cos(\alpha_{tx}) + R_{rx,0} \cos(\alpha_{rx}) = d_{tr}$;

then

$$R_{tx,0} \cos(\alpha_{tx}) + R_{tx,0} \frac{\sin(\alpha_{tx})}{\sin(\alpha_{rx})} \cos(\alpha_{rx}) = d_{tr}. \tag{7.8}$$

If α_{tx}, α_{rx} and d_{tr} are fixed, the values of $R_{tx,0}, R_{rx,0}$ are given by

$$R_{tx,0} = \frac{d_{tr}}{|\cos(\alpha_{tx}) + \sin(\alpha_{tx}) \cot(\alpha_{rx})|} \tag{7.9}$$

and

$$R_{rx,0} = R_{tx,0} \left| \frac{\sin(\alpha_{tx})}{\sin(\alpha_{rx})} \right|. \tag{7.10}$$

Then, for a given h_0 and d_{tr}, the set of possible angles is defined by the condition

$$|\cot(\alpha_{tx}) + \cot(\alpha_{rx})| = \frac{d_{tr}}{h_0}. \tag{7.11}$$

Monostatic Scenario

In the monostatic scenario, the same device hosts both transmitter and receiver; therefore, $\alpha_{tx}, \alpha_{rx} \approx 0$. This motivates the assumption of normal incidence.

We also observe that

- the distance between transmitter and receiver is little compared to the distance between them and the target, i.e. $TR \ll TO, TR$; this implies $\alpha_{tx} + \alpha_{rx} \ll \pi/2$;

- we assume normal incidence of the wavelength on the chest tissue interfaces.

Since we also assume normal incidence of the transmitted and reflected waveform, we have $\alpha_{tx} + \alpha_{rx} \approx 0$ and $\theta \approx \pi - \alpha_{tx} \approx \pi$, $\theta_r \approx \pi - \alpha_{rx} \approx \pi$. By applying the assumptions 7.2.1 in the generic configuration

$$R_{tx}(t) = \sqrt{R_{tx,0}^2 + x^2(t) - 2R_{tx,0}x(t)\cos(\theta)} \approx R_{tx,0} + x(t); \tag{7.12}$$

and

$$R_{rx}(t) = \sqrt{R_{rx,0}^2 + x^2(t) - 2R_{rx,0}x(t)\cos(\theta + \alpha_{rx} + \alpha_{tx})} \approx R_{rx,0} + x(t), \tag{7.13}$$

so that

$$d(t) \approx R_{tx,0} + R_{rx,0} + 2x(t). \tag{7.14}$$

Since now, we assume to be in the monostatic configuration.

7.3 Vital Sign Modulation on the Received Signal

The time variations of the target chest position provide a modulation of the main parameters of the received replicas, i.e. the attenuation ρ, the phase β and the ToA $\frac{d(t)}{c}$. We introduce here the parameters, for a generic signal with a central frequency of 4 GHz; in the last of the chapter we describe in detail the parameters, depending on the nature of the transmitted signal.

7.3.1 Attenuation Coefficient Modulation

According to far field assumptions, the received signal power attenuation is inversely proportional to the square of the path length, which in our scenario is a function of $x(t)$; therefore, $\rho(t) \propto \frac{1}{(d(t))}$. By assuming a path length of $d_{max} = 2$ m, and an oscillation amplitude of 5 cm, corresponding to a deep breath, we have a variation whose maximum amplitude is about -38 dB, and therefore not relevant for vital sign detection, $\rho(t) \approx \rho_0$.

7.3.2 Phase Modulation

Path length variation modulates also the phase of the received signal. In particular, for the considered carrier frequency and bandwidth we verified that a path length variation of 2 cm is sufficient to provide a phase shift of about $\frac{\pi}{2}$.

7.3.3 Time of Arrival Modulation

To determine whether our system is able to detect the path distance variation by a delay variation, we need to specify the system bandwidth B; in fact, the received signal is now sampled with period $T_c = \frac{1}{B}$, then $t = lT_c \quad l \in \mathbb{Z}^+$; we underline that we can sample with a smaller period, in order to improve the SNR, but we are not able to extract more accurate information about the CIR. We deduce then that the minimum path distance variation that we can detect is

$$\Delta d_{min,s} = c \cdot T_c = 13.64 \quad \text{cm}. \tag{7.15}$$

In Chapter 6 we evaluated the propagation speed in fat tissue, whose value for a signal propagating at 4 GHz is $v_{fat} \approx 1.3 \cdot 10^8$, and therefore we have

$$\Delta d_{min,f} = v_{fat} \cdot T_c = 5.9 \quad \text{cm}. \tag{7.16}$$

In our model we could detect the path distance variation by a delay variation only if a) the air-skin interface has an oscillation amplitude of about 7 cm, and/or b) the $\Delta_{fat}(t)$ amplitude is about 3 cm. If the condition a) could be verified in some cases, when the target takes a very deep breath, condition b) is never verified. Therefore, in general we are not able to detect the vital signs by variation on delays of target path.

7.4 Vital Sign Signal Power

We propose here a feasibility study for detecting vital signs, and in particular the heart rate, using a UWB technology under the compliance of FCC regulations with a *monostatic configuration*, i.e. where the transmitter and the receiver of the radar signal are located in the same device, as described in Fig. 7.3. We aim at evaluating the range of distances d between the radar and the target where the received power is enough to allow the detection of vital signs. A similar case has been investigated in [67], where the author evaluates the maximum distance allowed to see the signal reflected by the heart, modeled as a spherical metallic reflector, with a UWB radar system centered at 4.1 GHz. As illustrated in [63] and confirmed in Chapter 6, the expected received signal on the chest surface, i.e. when $d = 0$, is composed by a pulse reflected by the air skin interface, with expected SNR of -3 dB, and a weaker reflected pulse at -17 dB, due to the fat-muscle interface. For this study, we consider only the first reflection; the study can be extended also to consider the inner reflection, which carries the same information of respiration, and a stronger signal for heart beating. We perform the analysis in far field region, as it provides a simple analysis; this approximation is not well verified, due to both low distances and the presence of the interface of the target tissue, which violates the condition of free space propagation.

We are interested on the variation of the channel tap describing the target chest; we denote this signal as the *vital sign signal*, because it provides the desired information on target vital signs. The vital signal power P_u is then only a fraction D_{VS} of the received power P_r, i.e.

$$P_u = P_r D_{VS}.$$

In particular, D_{VS} represents the dynamic of the vital sign, i.e. the ratio between the power of the channel variation, due to the chest oscillation $x(t)$, and the received power. We summarize here all the assumptions used in the following:

- far field propagation;
- only line of sight (LOS) wireless signal propagation;
- one reflection due to the air-skin interface;
- the target chest is modeled as a spherical reflector whose radius is $a = 15$ cm
- the medium describing the target is an homogeneous and ideal dielectric;
- since we are interested in detecting both the respiration rate and the heart rate, and the latter is the weakest one, we expect the D_{VS} parameter of the heart beat signal to be very small. Therefore, we assume the D_{VS} parameter of heart beating as the worst case scenario, and we evaluate its expected value in the following.

7.4.1 Power of the Received Signal

Let

- EIRP be the effective radiated power; FCC regulations imposes a bound, depending on the system bandwidth [58];
- d be the round trip distance;

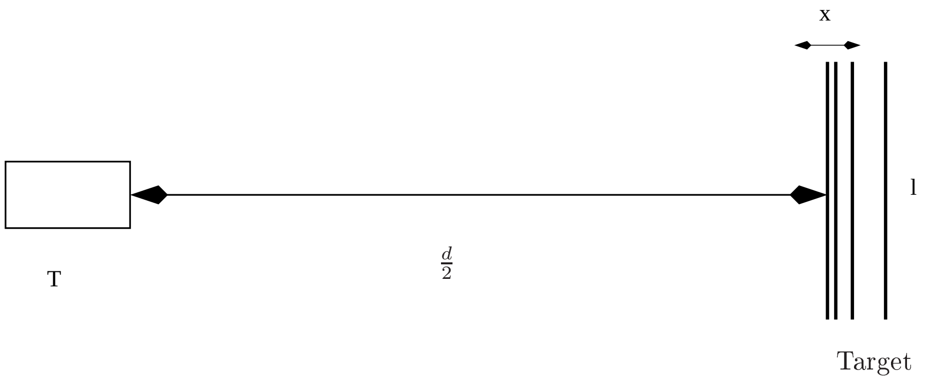

Figure 7.3: Description of the target chest with respect to the radar device in a monostatic configuration.

- σ be the radar cross section (RCS);
- $A_e = \dfrac{\lambda^2}{4\pi}$ be the receiving antenna aperture;
- $\dfrac{\sigma}{4\pi d^2}$ be the fraction of EIRP reflected by the target chest;
- $\dfrac{A_e}{4\pi d^2}$ be the fraction of the reflected power received by the receiving antenna aperture.

The received power is then given by [67]

$$P_r = \mathrm{EIRP}\frac{\sigma}{4\pi d^2}\frac{A_e}{4\pi d^2} \tag{7.17}$$

7.4.2 Main Features of the Commercial UWB System

We consider a Time Domain PulseOn210 system [68].

We report the main parameters

- central frequency $f_C = 4.2$ GHz;
- system bandwidth $B = 2.2$ GHz;
- FCC power spectral density limit $PSD_{FCC} = -41.3$ dBm/MHz.

Due to the limits on the transmitted power, we have unitary antenna gain at the transmitter ($G_t = 1$) and in our scenario

$$EIRP|_{dBm} = PSD_{FCC}|_{dBm/MHz} + B|_{dBMHz} = -7.88\text{dBm}.$$

7.4.3 Radar Cross Section Evaluation

We evaluate here the RCS of the target chest, seen as a spherical reflector of a homogeneous dielectric medium. For a spherical reflector, RCS is given by

$$\sigma = |A_{tgt} R_{tgt} G_{tgt}| \tag{7.18}$$

where A_{tgt} is the projected area of the target seen by the radar, R_{tgt} is the reflectivity of the target and G_{tgt} is the antenna-like gain of the target. In the following we evaluate each of these terms

A_{tgt}

The projected area of the target depends on the carrier frequency, and in particular on the value of the parameter $\frac{2\pi a}{\lambda}$; in our case, since the condition of the optical region $\frac{2\pi a}{\lambda} > 10$ is verified in the system band, we have $A_{tgt} \approx \pi a^2$.

R_{tgt}

We discussed in Section 6.2 the reflectivity of the target; since we assume only the first and strongest reflection, from the air skin interface, the reflected power ratio is

$$R_{tgt}(f) = R_1(f) = \left| \frac{\tilde{\eta}_1(f) - \tilde{\eta}_0}{\tilde{\eta}_1(f) + \tilde{\eta}_0} \right|^2 . \tag{7.19}$$

In general, $\tilde{\eta}_i$ is a function of the frequency, and in our scenario its value is around -3 dB. This approximation has been derived with a widely used method [1, 63], and provides a better insight with respect to the metallic sphere model.

G_{tgt}

We assume the worst case scenario, where the target has no antenna-like gain, i.e. $G_{tgt} = 1$.

7.4.4 Maximum Detection Distance

In our scenario the desired signal power is given by

$$
\begin{aligned}
P_u = P_r D_{VS} = D_{VS}\mathrm{EIRP}\frac{\sigma}{4\pi d^2}\frac{A_e}{4\pi d^2} = D_{VS}\mathrm{EIRP}\frac{\sigma\lambda^2}{(4\pi)^3 d^4} = \\
= D_{VS}\mathrm{EIRP}\frac{\lambda^2 R_1(f)\pi a^2}{(4\pi)^3 d^4}.
\end{aligned}
\tag{7.20}
$$

The maximum distance d_{max} allowed to sense the heart beating is the distance d where P_u is equal to the receiver sensitivity $P_{u,min}$. We assume from [69] that $P_{u,min} = -85$ dBm.
From (7.20) we have then

$$
\begin{aligned}
R_{max} = \sqrt[4]{\frac{D_{VS}\mathrm{EIRP}\sigma\lambda^2}{P_{u,min}(4\pi)^3}} = \\
= \sqrt[4]{\frac{D_{VS}\mathrm{EIRP}R_1(f)\pi a^2 c^2}{P_{u,min}(4\pi)^3 f^2}}.
\end{aligned}
\tag{7.21}
$$

At the best of our knowledge, there are not accurate measurements of the amplitude of the oscillation of the chest skin due to heart beating. However, we observe that this oscillation in general can not be detected by the eye, while it can be detected by touch. The maximum theoretical resolution of the eye, at its best acuity, has been estimated as 0.35 mm, while the minimum oscillation can be detected by touch is on the order of 10^{-5} m [70]; we consider then the worst case oscillation amplitude of the skin Δx on the order of 10μm, i.e. almost two orders of magnitude lower than the eye acuity bound. This oscillation provides a variation on the ToA of the received pulse of $\Delta x/c$, which is too small to be detected with our system; however, it will affect the received signal both in amplitude and phase. Then, the desired signal will be related to the value $2\pi f 2\Delta x/c \approx 10^{-3}$, and then $D_{VS} \approx 10^{-6}$. The resulting value of the detection range is described in Fig. 7.4; as we can see, detecting heart beating in the considered band is possible only for a distance lower than 25 cm.

We can repeat the same study for the detection of the respiration rate; it is easily verified that in this case the signal dynamic $D_{VS} \approx 10^{-2}$. In this case, the detection range is about 2.5 m.

7.4.5 Signal to Noise Ratio (SNR) Optimization Using UWB Redundancy

With the pulse UWB technology, the pulse repetition period is very small with respect to the coherence time of vital signs; in the considered PulseOn application, the

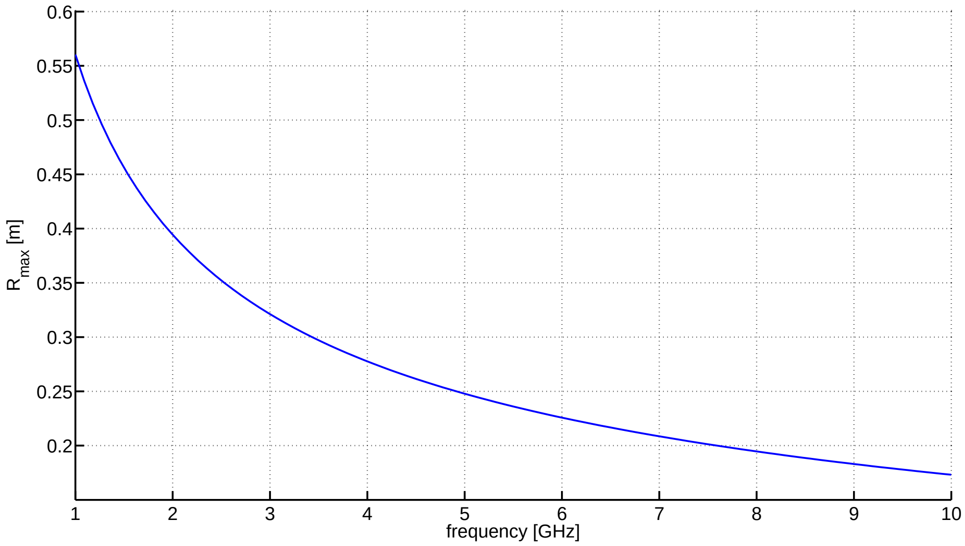

Figure 7.4: Maximum range as a function of frequency

repetition frequency is 10 MHz, while vital signs have a rate of some Hz. By assuming that the vital signs are constant on a time period of 0.1 s, we have about 10^6 pulses providing the same sample of the vital sign process. We can use this redundancy to increase the desired signal power P_u; theoretically, we could achieve a maximum gain of about $10^5 \div 10^6$. However, hardware limitations usually prevent the system from achieving the maximum gain; in particular, the maximum gain achievable with the PulseOn Time Domain device is $G_{UWB} \approx 10^3$. Then the maximum range is

$$\begin{aligned} d_{max} &= \sqrt[4]{G_{UWB}\frac{D_{VS}\mathrm{EIRP}\sigma\lambda^2}{P_{u,min}(4\pi)^3}} = \\ &= \sqrt[4]{\frac{D_{VS}\mathrm{EIRP}R_1(f)\pi a^2 c^2}{P_{u,min}(4\pi)^3 f^2}}. \end{aligned} \tag{7.22}$$

The corresponding detection range is described in Fig. 7.5; we observe that with this operation we are able to detect the heart beating in our band with a distance up to 8 m, which is a reasonable value for an indoor scenario. For the respiration, the detection range is about 80 m. The operation of increasing the SNR is already implemented in the UWB device as an averaging operation, which is optimal for an additive while Gaussian noise (AWGN) channel.

We conclude this study with some considerations:

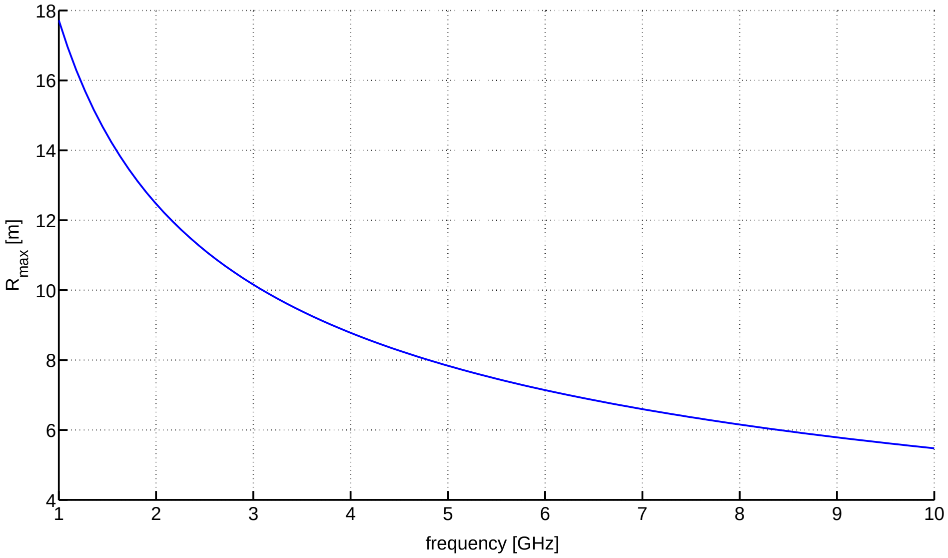

Figure 7.5: Maximum range as a function of frequency considering the average gain.

- FCC compliance poses a severe limit for detection of vital signs, and in particular for heart beating;
- the detection range sensibly depends on frequency;
- signal to noise ratio (SNR) maximization is a key issue to address for remote sensing;
- UWB technology provides a description of the channel with a detail higher than necessary for our processes, which are very slow with respect to the pulse repetition duration; this redundancy can be used to increase the vital signs signal power, and therefore also the maximum detection range.

Chapter 8

System Model

System model is a result of different steps, with an increasing level of complexity of the considered scenario. In fact, as a first step in Section 8.1 we derive a *narrowband model* for a single scattering scenario; we derive for this model the Doppler analysis i.e., how the chest motion is related to the variations of the received signal. The second step is to extend the model to a *single scattering, wideband model*, modeled as a parallel of narrowband subsystems in Section 8.2.1. The third step is to extend the model to a *multiscattering, wideband model*, described in Section 8.2.2; in this condition, two different scenarios are investigated: line of sight scenario (LOS), where all the reflections are in phase, and local rich scattering scenario (LRS) where all the reflected signals are not exactly in phase. Finally, we introduce the complete channel model, where we consider the entire channel impulse response, LRS scenario and the presence of two reflections, inner and outer, from the target, in Section 8.3. Part of this work has been published in [71].

8.1 Narrowband System Model

We first discuss the vital signs modulation on the parameters of the received signal for a narrowband system, as the simple analysis describing the narrowband scenario is useful to describe the wideband system. In a narrowband system, the transmitted pulse is a narrowband pulse $p_N(t)$. Let us suppose that we have only the reflection by the air skin interface of the target, without multipath. We consider the target chest as a point scatterer. Then the received signal for a single pulse can be written as

$$r(t) = \rho_t \sqrt{R_1} p_N \left(t - \frac{d(t)}{c}\right) \cos\left(2\pi f_C \left(t - \frac{d(t)}{c}\right) + \phi_0 + \phi_t\right) + \eta(t), \tag{8.1}$$

where ϕ_0 is the initial phase, ϕ_t is the phase shift introduced by the reflection, ρ_t is the propagation attenuation coefficient and R_1 is the reflection coefficient. There is no amplitude modulation, while the relationship between the instantaneous phase of the received replica $\beta(t)$ and $d(t)$ is known, i.e.

$$\beta(t) = -2\pi f_C \left(\frac{d(t)}{c}\right) + \phi_0 + \phi_t. \tag{8.2}$$

8.1.1 Doppler Estimation Theory

From (8.1), the instantaneous phase of $r(t)$ is

$$\beta(t) = -2\pi f_C \left(\frac{d(t)}{\lambda_C}\right) + \phi_0 + \phi_t, \tag{8.3}$$

and then the Doppler frequency is

$$f_d \triangleq \frac{1}{2\pi}\frac{\partial \phi_r(t)}{\partial t} = -\frac{1}{\lambda_C}\frac{\partial d(t)}{\partial t}. \tag{8.4}$$

In general, if we consider the presence of different paths involving the target in motion, we have $d(t) = \sum_{i=1}^{N_{hop}} d_i$. Each path is affected by Doppler whose frequency is

$$f_{d,m} \triangleq \frac{1}{2\pi}\frac{\partial \phi_{r,m}(t)}{\partial t} = \sum_{i=1}^{N_{hop}} -\frac{1}{\lambda_i}\frac{\partial\left(d_i\right)}{\partial t}, \tag{8.5}$$

where N_{hop} is the number of reflections which occur from the transmitter to the receiver, and λ_i is the wavelength of the signal propagating on the medium of path i.

8.2 Wideband System Model

The narrowband Doppler analysis is not sufficient to describe an UWB scenario; in fact, all the parameters used in that analysis, such as the speed, the wavelength, the attenuation, depend on the frequency. However, the narrowband Doppler approach allows a simple model of the effects of vital signs on the received signal. This motivates our suggestion of modeling the UWB system as a parallel of N_B narrowband

systems. By this model, we can apply the narrowband analysis to each subsystem; the value of N_B is chosen in order to have on each sub-band a flat pulse frequency response, and a flat attenuation.
We consider now two scenarios: in one case, where the chest is still modeled as a single scatterer, while in the second case the chest is modeled as a set of scatterers.

8.2.1 Single Scatterer Scenario

We model the signal $r(t)$ as the sum of the N_B received signals of the narrowband subsystems. For each subsystem b, the central frequency is $f_b = f_I + b\frac{B}{N_B}$, where f_I is the lower bound of the UWB band. The corresponding equivalent pulse $p_b(\tau)$ is assumed to be a constant in frequency domain on sub-band b, i.e. $P_b(f) = P(f_b)\mathrm{rect}(\frac{f-f_b}{N_B/2})$, and therefore in time domain can be written as i.e.

$$p_b(\tau) = P(f_b)\mathrm{sinc}\left(\frac{B}{N_B}\tau\right). \tag{8.6}$$

Then, the received signal can be written as

$$\begin{aligned} r(t) = & \sum_{b=0}^{N_B-1} \rho_0\sqrt{R_1}p_b\left(t-\frac{d(t)}{c}\right)\cos\left(2\pi(f_I+b\frac{B}{N_B})\left(t-\frac{d(t)}{c}\right)+\phi_0+\phi_t\right)+ \\ & +\eta(t) \end{aligned} \tag{8.7}$$

where $\eta(t)$ is the noise term. The equivalent baseband signal is

$$r_{BB}(t) = \sum_{b=0}^{N_B-1} \rho_0\sqrt{R_1}p_b\left(t-\frac{d(t)}{c}\right)e^{-j2\pi(f_I+b\frac{B}{N_B})\frac{d(t)}{c}+\phi_0} + \eta_{BB}(t). \tag{8.8}$$

Under the assumption of flat frequency fading of the narrowband pulses p_b on their sub-bands, i.e. $P(b) \approx P$, and $A = P\rho_0\sqrt{R_1}\exp(\phi_0)$ we have

$$\begin{aligned}
r_{BB}(t) &\approx A\mathrm{sinc}\left(\frac{B}{N_B}\left(t-\frac{d(t)}{c}\right)\right)\sum_{b=0}^{N_B-1} e^{-j2\pi\left(f_I+b\frac{B}{N_B}\right)\frac{d(t)}{c}}+\eta_{BB}(t)=\\
&= Ae^{-j2\pi f_I\frac{d(t)}{c}}\sum_{b=0}^{N_B-1}\left[e^{-j2\pi\frac{B}{N_B}\frac{d(t)}{c}}\right]^b+\eta_{BB}(t)=\\
&= A\mathrm{sinc}\left(\frac{B}{N_B}\left(t-\frac{d(t)}{c}\right)\right)e^{-j2\pi f_I\frac{d(t)}{c}}\frac{1-\left[e^{-j2\pi\frac{B}{N_B}\frac{d(t)}{c}}\right]^{N_B}}{1-e^{-j2\pi\frac{B}{N_B}\frac{d(t)}{c}}}+\eta_{BB}(t)=\\
&= A\mathrm{sinc}\left(\frac{B}{N_B}\left(t-\frac{d(t)}{c}\right)\right)e^{-j2\pi f_I\frac{d(t)}{c}}\frac{e^{-j2\pi\frac{B}{2}\frac{d(t)}{c}}}{e^{-j2\pi\frac{B}{2N_B}\frac{d(t)}{c}}}\frac{\sin\left(2\pi\frac{B}{2}\frac{d(t)}{c}\right)}{\sin\left(2\pi\frac{B}{2N_B}\frac{d(t)}{c}\right)}+\eta_{BB}(t)=\\
&= A\mathrm{sinc}\left(\frac{B}{N_B}\left(t-\frac{d(t)}{c}\right)\right)e^{-j2\pi\left(f_C-\frac{B}{2N_B}\right)\frac{d(t)}{c}}\cdot\\
&\cdot\frac{\sin\left(2\pi\frac{B}{2}\frac{d(t)}{c}\right)}{\sin\left(2\pi\frac{B}{2N_B}\frac{d(t)}{c}\right)}+\eta_{BB}(t)
\end{aligned}\tag{8.9}$$

After some algebra we obtain $\alpha(t) = \dfrac{\sin\left(2\pi\frac{B}{2}\frac{d(t)}{c}\right)}{\sin\left(2\pi\frac{B}{2N_B}\frac{d(t)}{c}\right)}$, while $\beta(t) = e^{-j2\pi\left(f_C-\frac{B}{2N_B}\right)\frac{d(t)}{c}}$. In Fig. 8.1 the absolute value and phase modulation of the received signal are shown for a system whose bandwidth is 2.2 GHz, divided into $N_B = 10^6$ subsystems, where the target is at distance of 1 m oscillating as a sinusoidal function with amplitude 2 mm. We observe that the oscillation of the target modulates also the amplitude of the received signal; in particular, the modulation functions of amplitude and phase have the same frequency of the target oscillation and a phase shift of $\pi/2$.

In general, we observe that the UWB signal is modulated by vital signs both in amplitude and phase; however, the modulation is not as simple as (8.9), since this formula has been derived under singe scatterer and very short pulse assumptions.

8.2.2 Rich Scattering Scenario

Until now, we modeled the chest as a point reflector; a more realistic approximation is to consider the chest as a set of reflecting points, each providing a reflected signal

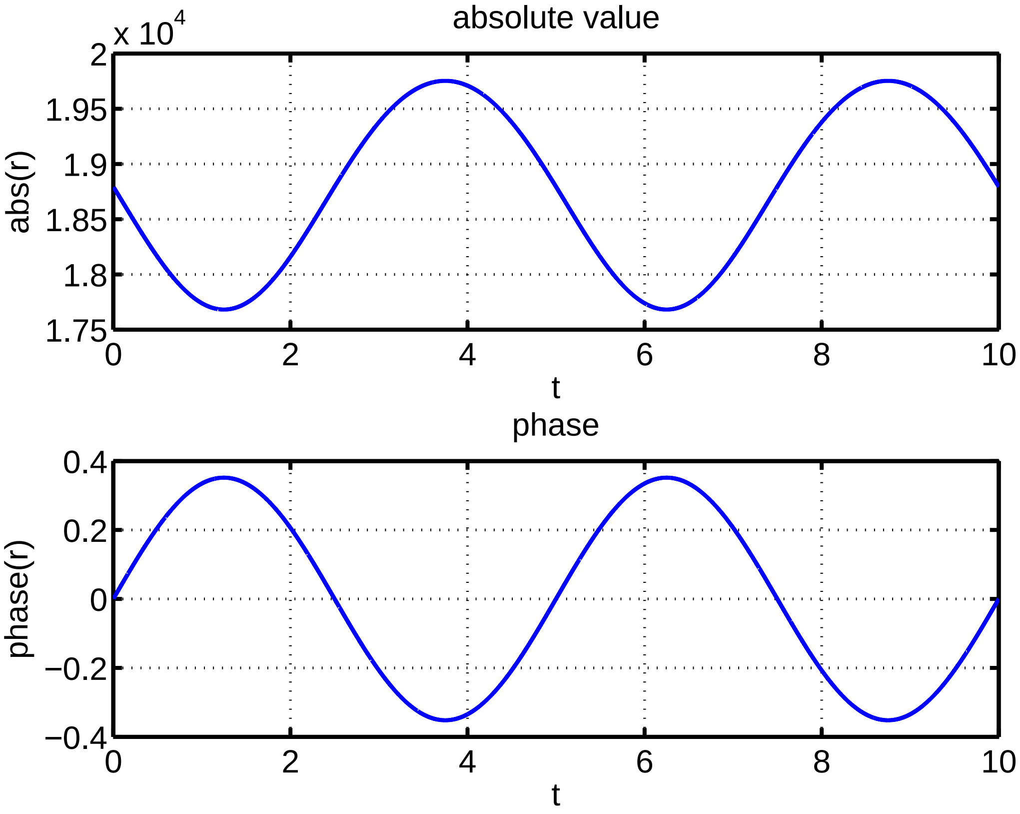

Figure 8.1: Modulation of amplitude and phase of the received signal in UWB single scattering scenario

with its phase shift and delay. In general, the chest section can be seen as an ellipse expanding and contracting due to respiration and heart beating. Using the spherical waves propagation model, it is easily shown that the receiver collects the signal reflected by a small area around the center of the chest. In fact, the waves reflected at the borders don't reach the receiver in a monostatic configuration. Therefore, we can approximate the chest as a planar surface, moving according to a rigid translation; the reflected waves differ slightly in phase, because of very little differences of path length from each point of the surface. Even if our system is not able to resolve the differences in delay, if there are enough reflections, we may observe also an amplitude modulation of the received signal. The target chest, and in general the entire target body could also behave as a set of scatterers, each of them with its own incidence angle, reflection coefficient and phase. This hypothesis differs from the rich scattering, considered for wireless communications [2] because in this case all the scatterers are concentrated on a limited region of the space, and then they are not uniformly distributed w.r.t. the receiver. However, in general we assume that the amplitude and phase diversity provided by all the received replicas is sufficient to cause a significant variation of the amplitude of the received signal, together with its phase. This effect is combined with the UWB amplitude modulation, as seen in the previous paragraph.
Let us consider Ns scatterers; each scatterer n_s is characterized by its own distance from the radar $d_n(t)$.

$$\begin{aligned} r_{BB}(t) = \sum_{n_s=1}^{Ns} \sum_{b=0}^{N_B-1} \rho_0 \sqrt{R_1} p_b \left(t - \frac{d_{n_s}(t)}{c} \right) \cdot \\ \cdot \, e^{-j2\pi (f_I + b\frac{B}{N_B}) \frac{d_{n_s}(t)}{c} + \phi_0} + \eta_{BB}(t). \end{aligned} \tag{8.10}$$

Although the number and the distances of the scatterers are unknown, (8.10) suggests that both $\alpha(t)$ and $\beta(t)$ are functions of time with the same periodicity features of the chest oscillation function $x(t)$.

8.3 UWB Model with Multiple Target Reflections

We consider now the most generic configuration, which includes multipath due to the indoor scenario and multiple target reflections due to the multilayer nature of the chest, i.e. an indoor channel scenario with a discrete and finite number N_{tap} of reflectors. Then the received signal becomes

$$r_{BB}(t) = \sum_{i=1}^{N_{tap}} s_{BB}(t - \tau_i(t))h_{BB}(\tau_i(t)) + \eta_{BB}(t) \tag{8.11}$$

where

$$s_{BB}(t) = \sum_{j=-\infty}^{\infty} p(t - jT_S)$$

is the baseband equivalent transmitted signal, $\tau_i(t)$ defines the ToA of the replica reflected by reflector i, and h_{BB} is the equivalent baseband channel impulse response. Let us define $N_{layer}^{(i)}$ as the number of layers of path i, $d_{i,l}(t)$ the length of layer l of path i, and $v_{i,l}$ the speed of light in layer l of path i; then we have

$$\tau_i(t) = \sum_{l=1}^{N_{layer}^{(i)}} \frac{d_{i,l}(t)}{v_{i,l}}$$

, i.e., the ToA of the replica reflected by reflector i is the sum of the delays provided by the propagation on medium layer l with propagation speed $v_{i,l}$. We assume all other reflectors as static and ideal conductive objects; they are described with only one layer, and with a time-invariant distance. Furthermore, the analysis provided in Chapter 6 suggests to model the target as two interfaces, each one reflecting the transmitted signal with its attenuation and a phase shift of π. We will indicate with index T the target; we also indicate with the subscript 1 the outer interface (air-skin-fat), and with 3 the inner one (fat-muscle), using the same notation introduced in Chapter 6; the two interfaces are separated by $z_3 \approx 0.96$ cm. We consider the fat tissue as a rigid tissue; then, both the interfaces will have the same motion due to respiration, modeled as $x_r(t)$. The motion of the two interfaces due to the heart beat takes into account the attenuation due to the tissues i.e., we expect the inner interface to be more affected by the heart beat then the outer interface. For the inner interface we have $x_{h,3}(t)$ while for the outer $x_{h,1}(t)$; these two functions differ only for the attenuation factor, which is higher for the outer reflection. By combining the effect of respiration and heart beating we have that the round trip distances for the two interfaces are $d_1(t) = R_T + x_r(t) + x_{h,1}(t)$ and $d_3(t) = d_1(t) + \Delta_3(t) =$

$d_1(t) + z_{fat} - 2(x_{h,3}(t) - x_{h,1}(t))$. Then we can write

$$\begin{aligned} r_{BB}(t) = & \sum_{i \neq T} s_{BB}\left(t - \frac{d_i}{c}\right) h_{BB}\left(\frac{R_i}{c}\right) + \eta_{BB}(t) + \\ & + s_{BB}\left(t - \frac{d_1(t)}{c}\right) h_{BB}\left(\frac{d_1(t)}{c}\right) + \\ & + s_{BB}\left(t - \left(\frac{d_1(t)}{c} + \frac{\Delta_3(t)}{v_f}\right)\right) h_{BB}\left(\frac{d_1(t)}{c} + \frac{\Delta_3(t)}{v_f}\right). \end{aligned} \tag{8.12}$$

Let us now indicate with $r_{TI}(t)$ the first component of the signal; in the following we will describe how we cancel it. We have

$$\begin{aligned} r_{BB}(t) = & \, r_{TI}(t) + \eta_{BB}(t) + \\ & + s_{BB}\left(t - \frac{d_1(t)}{c}\right) h_{BB}\left(\frac{d_1(t)}{c}\right) + \\ & + s_{BB}\left(t - \left(\frac{d_1(t)}{c} + \frac{\Delta_3(t)}{v_f}\right)\right) h_{BB}\left(\frac{d_1(t)}{c} + \frac{\Delta_3(t)}{v_f}\right). \end{aligned} \tag{8.13}$$

We recall here some results that we verified in the previous Chapters:

- in general, even using all the band allowed by FCC, we are not able to detect the vital signs by variation on delays of target path;
- since $z_3 < 3$ cm, the inner and outer paths are represented by the same time sample, defined as τ_T;
- the non aliasing condition is verified, $T_c > 2T_P$ and then we don't have aliasing between adjacent pulses;
- the theoretical narrowband and wideband model described in Sections 8.1 and 8.2 suggests that the target replicas are modulated by vital signs both in amplitude and in phase.

An exact expression of modulation has been derived in Section 8.2, by considering only the outer reflection; a similar analysis can be performed also for the inner reflection, which provides its own amplitude and phase modulation to the received signal. In general, we describe both amplitude and phase of the received replica as functions of chest oscillation, i.e.

$$\begin{aligned} h_{BB}\left(\frac{d_1(t)}{c}\right) &= \alpha_1(t) e^{-j\beta(t)} \\ h_{BB}\left(\frac{d_3(t)}{c}\right) &= \alpha_3(t) e^{-j\beta(t)}. \end{aligned} \tag{8.14}$$

In general, we observe that function $\beta(t)$ is proportional to $d(t)$, while there is not a general analysis providing an expected behavior of α_1 and α_3. The sampled received signal expression becomes

$$\begin{aligned} r_{BB}(lT_c) &= r_{TI}(lT_c) + s_{BB}\left(lT_c - \tau\right)\big[\alpha_1(d_1(lT_c))e^{-j\beta(d_1(lT_c))} + \\ &+ \alpha_3(d_1(lT_c) + \frac{\Delta_3(lT_c)}{v_f})e^{-j\beta(d_1(lT_c)+\frac{\Delta_3(lT_c)}{v_f})}\Big] + \eta_{BB}(lT_c). \end{aligned} \tag{8.15}$$

We remind now the properties of this signal: $s_{BB}(lT_c)$ is a periodic function with repetition frequency equal to PRF. We also suppose that $2\pi\frac{f_C}{PRF}$ is a multiple of 2π. Then we divide the temporal axis into pulse repetition periods of duration $T_{REP} = \frac{1}{PRF}$ with length KT_c (larger then the CIR length), $K = \frac{T_{REP}}{T_c}$. We verified that $s_{BB}(lT_c) = s_{BB}(lT_c + T_{REP}) = p(lT_c)$. Then we write

$$lT_c = n_{REP}T_{REP} + n_K T_c \quad n_K = 0, \cdots, K-1; \quad n_{REP} \in \mathbb{Z}^+, \tag{8.16}$$

and the received signal is

$$\begin{aligned} r_{BB}(n_{REP}T_{REP} + n_K T_c) &= r_{TI}(lT_c) + p\left(lT_c - \tau\right)\left[\alpha_1(d_1(n_{REP}T_{REP} + n_K T_c))\cdot\right. \\ &\cdot e^{-j\beta(d_1(n_{REP}T_{REP}+n_K T_c))} + \alpha_3(d_1(n_{REP}T_{REP} + n_K T_c) + \frac{\Delta_3(n_{REP}T_{REP} + n_K T_c)}{v_f})\cdot \\ &\left.\cdot e^{-j\beta(d_1(n_{REP}T_{REP}+n_K T_c)+\frac{\Delta_3(n_{REP}T_{REP}+n_K T_c)}{v_f})}\right] + \eta_{BB}(n_{REP}T_{REP} + n_K T_c) \end{aligned} \tag{8.17}$$

We observe that the coherence time of the observed processes is larger than both T_c and T_{REP}; in fact, $f_r, f_h < 10\text{Hz} \ll 9.611$ MHz; we can then use the redundant amount of samples to improve the SNR. We call slot a set of N_S successive symbols, and we assume that the slot duration is lower than the coherence time of vital signs. At the transmitter we modulate the transmitted pulses with a pseudonoise sequence; then the receiver performs a despreading with a spreading factor of N_S.

To correctly reconstruct the vital sign signal, it is then sufficient a sample period of $T_{scan} = N_S T_{REP}$; $d_1(n_{REP}T_{REP} + n_K T_c), d_3(n_{REP}T_{REP} + n_K T_c), \Delta_3(n_{REP}T_{REP} + n_K T_c)$ are supposed to be constant in a slot. We have

$$\begin{aligned} r_{BB}(kT_{scan} + n_K T_c) &= r_{TI}(n_K T_c) + p\left(n_K T_c - \tau\right)\big[\alpha_1(d_1(kT_{scan}))e^{-j\beta(d_1(kT_{scan}))} + \\ &+ \alpha_3(d_1(kT_{scan}) + \frac{\Delta_3(kT_{scan})}{v_f})e^{-j\beta(d_1(kT_{scan})+\frac{\Delta_3(kT_{scan})}{v_f})}\Big] + \eta_{BB}(kT_{scan} + n_K T_c) \end{aligned} \tag{8.18}$$

In the following we consider $T_{scan} = 1$ ms. The time scale $n_K T_c$ represents the delays of CIR. We observe that $r_{TI}(n_K T_c)$ does not depend on n_K; in fact, in our model the vital signs and the white noise are supposed to be the only time variant processes in the channel. We can estimate this static part of the CIR and cancel it using a background subtraction operation; one simple method to estimate it is taking the average of $r_{BB}(kT_{scan} + n_K T_c)$ over k. After background subtraction from (8.18) we obtain a noisy version of the target component

$$\begin{aligned} r_T(kT_{scan} + n_K T_c) = p\left(n_K T_c - \tau\right) \Big[& \alpha_1(d_1(kT_{scan}))e^{-j\beta(d_1(kT_{scan}))} + \\ +\alpha_3(d_1(kT_{scan}) + \frac{\Delta_3(kT_{scan})}{v_f})& e^{-j\beta(d_1(kT_{scan}) + \frac{\Delta_3(kT_{scan})}{v_f})} \Big]. \end{aligned} \tag{8.19}$$

Note that $r_T(n_K T_c + kT_{scan})$ is a time-varying signal since the round trip distance from the air-skin interface $d_1(kT_{scan})$ and from the fat-muscle interface $d_1(kT_{scan}) + \frac{\Delta_3(kT_{scan}}{v_f})$ depend on respiration and heart beating.

We then model the wide band system as a parallel of N_B narrowband systems. By this model, we can apply the Doppler analysis to each subsystem; furthermore, we avoid to perform deconvolution with $p(t)$, since on each subsystem the pulse frequency response is supposed to be constant.

8.3.1 Combination of the UWB Signal at Each Scan to Maximize SNR

In Subsection 7.3.3 we verified that the delays of different points of the target chest cannot be distinguished; therefore, in our assumptions and without noise, one value of n_K, corresponding to the target delay τ_T, is sufficient to describe the received pulse, with $Tc = \frac{1}{B}$. The presence of more then one values of n_K where $r_T(n_K T_c + kT_{scan}) \neq 0$ occurs if oversampling is performed. In fact, the presence of noise and distortion on the received signal suggests to benefit from the oversampling factor to improve the SNR, i.e. to find the best way to combine the samples describing the same channel path and obtain the vital sign signal $v(kT_{scan})$. From the theoretical point of view, in absence of ISI, the linear combination that maximizes the SNR is provided by the match filter [41]. In absence of noise, the combination of all samples $r_T(n_K T_c + kT_{scan})$ for each scan providing the maximum SNR is given by

$$v(nT_{scan}) = \max_{n_K}\{r_T * g_1 \quad (n_K T_c + kT_{scan})\}. \tag{8.20}$$

where $g_1(t) = p^*(-t)$ is the matched filter [41] and $*$ is the convolution operator. By assuming only the AWGN noise as disturb, performing the convolution described in (8.20) we obtain

$$\tilde{v}(kT_{scan}) = v(nT_{scan}) + w(nT_{scan}), \tag{8.21}$$

where $w(nT_{scan})$ is the resulting noise component.

Chapter 9

Detection Techniques

We aim at detecting the heart rate and respiration rate of the target, based on the knowledge of the noisy signal $\tilde{v}(k)$ which collects the contribution of both phenomena. As the convolution in (8.20) is a linear operator, the resulting signal $\tilde{v}(nT_{scan})$ is a zero mean signal affected by zero mean AWGN noise $w(nT_{scan})$, i.e.

$$\tilde{v}(nT_{scan}) = v(nT_{scan}) + w(nT_{scan}). \tag{9.1}$$

We verified that the shape of respiration and heart beating changes significantly with many factors, e.g. angle of incidence, distance of the radar, position of the target. Therefore, we cannot exploit any a priori information on the signal shape.

In general, $v(k)$ is a non stationary signal, mainly because of the irregular nature of the respiration process. Therefore, $v(k)$ cannot be considered as a periodic signal in strict sense; it is then assumed locally periodic, i.e. the periodicity of $v(k)$ is assumed to be slowly varying and constant in a range of samples of length N. In the following, we will focus on the period estimation performed on a window of N samples and therefore consider an observation of the signal $\tilde{v}(k)$, $k = 1 \dots N$.

The choice of the number of observed samples N is dictated both by the desired estimation time and by the fact that signal $v(k)$ may be regarded as periodic only for a limited time. This is the case of vital signs (heart beating and respiration rate), which can be assumed periodic as long as the target conditions, including his movements, speaking activity, etc., are not changing. The investigations on respiration and heart beating allow us to consider two ranges $\mathcal{I}_r$, $\mathcal{I}_h$ of periods, suitable for respiration and heart beating, respectively. In particular, for a healthy adult target we consider $\mathcal{I}_r = [0.5s\ 10s]$, and $\mathcal{I}_h = [0.3s\ 1.2s]$, corresponding to a heart rate range of $50 - 200$ beats per minute (bpm). Since we can not make any assumption on the shape of $v(k)$, we ignore correlation among samples within a period. In particular we model $v(k)$ as a white Gaussian process with unitary variance $\mathrm{E}\left[|v(k)|^2\right] = 1$ and zero mean within the elementary period. Consequently, the column vector $\mathbf{v} = [v(1), \cdots, v(N)]^H$ is a zero mean Gaussian vector with covariance matrix

$$\mathbf{\Sigma_r}(P) = \mathrm{E}\left[\mathbf{v}\mathbf{v}^H\right], \tag{9.2}$$

where we have highlighted its dependence on the period P, and ^{H} denotes the Hermitian operator. Assuming that $\tilde{v}(k)$ has period P, the entries of $\mathbf{\Sigma_v}(P)$ are

$$\left[\mathbf{\Sigma_v}(P)\right](k, k+l) = \mathrm{E}\left[v(k)v(k+l)^H\right] = \begin{cases} 1, & \text{if } l = mP, m \in \mathcal{Z} \setminus \{0\} \\ 1+\sigma_w^2 & \text{if } l = 0, \\ 0 & \text{elsewhere} \end{cases} \tag{9.3}$$

where in the last case the assumption of white process for $v(k)$ is used.

9.1 Autocorrelation Based Period Detection

A significant amount of literature uses the correlation to estimate the period of the signal $v(k)$ [72], [73]. If the signal is ergodic, an estimate of the correlation is given by

$$C(n) = \frac{1}{N}\sum_{l=1}^{N} v(l)v^*((l+n)_N), \quad n = 0 \ldots N-1, \tag{9.4}$$

where the averaging is performed over N samples and the expression $(a)_N$ stands for a mod N. The optimum value of N depends on the noise level and on the validity of the assumption of ergodicity. In absence of noise, the real part of $C(n)$, $\Re[C(n)]$, is periodic and reaches its maxima for $n = mP$. Hence, according to the correlation based (CORR) algorithm, the period estimation is performed as

$$P_{\text{CORR}} = \text{argmax}_n \quad \Re[C(n)]. \tag{9.5}$$

The method in (9.4) does not take into account the presence of noise. The function $|C(n)|$ is periodic and reaches its maxima if n is a multiple of the period $\bar{P}$. The same periodicity information provided by the autocorrelation function can be seen in frequency domain through the periodogram; different algorithms have been proposed to evaluate the periodogram of a function.

9.2 Maximum Likelihood Period Detection

We propose the maximum likelihood (ML) period estimator for the considered signal. Let $f(\mathbf{v}|n)$ be the conditioned probability density function (pdf) of v given that $P = n$. Then, the log-likelihood function is

$$\Lambda(n) = \log(f(\mathbf{v})) \tag{9.6}$$

and the ML estimator is

$$P_{\mathrm{ML}} = \mathrm{argmax}_n \quad \Lambda(n) \tag{9.7}$$

Reminding that the conditional pdf of the zero mean Gaussian vector v is

$$f(\mathbf{v}|n) = \frac{1}{(2\pi)^{N/2} \parallel \mathbf{\Sigma_v}(n) \parallel^{1/2}} e^{-\frac{1}{2}\mathbf{v}^H \mathbf{\Sigma_v}^{-1}(n)\mathbf{v}}, \tag{9.8}$$

the log-likelihood function for a candidate period n is given by

$$\Lambda(n) = \log(f(\mathbf{v}|n)) = \log\left[\frac{1}{(2\pi)^{N/2} \parallel \mathbf{\Sigma_v}(n) \parallel^{1/2}}\right] - \frac{1}{2}\mathbf{v}^H \mathbf{\Sigma_v}^{-1}(n)\mathbf{v}. \tag{9.9}$$

From (9.3) we observe that $\mathbf{\Sigma_v}(n)$ is a Toeplitz matrix. Furthermore, if N is a multiple of n, i.e. $N = Ln$, $\mathbf{\Sigma_v}(n)$ is circulant, generated by vector $\mathbf{c} = [1 + \sigma_w^2 \quad \mathbf{0}_{n-1}^T \quad 1 \quad \mathbf{0}_{n-1}^T \cdots \mathbf{0}_{n-1}^T]$.
In the following we consider $N \gg n$, $n \in \mathcal{I}_P$, so that

$$\lfloor \frac{N}{\max \quad n} \rfloor \max \quad n \approx \lfloor \frac{N}{\min \quad n} \rfloor \min \quad n \approx N.$$

Under this assumption, in the following we assume N as a multiple of n. If $\sigma_w^2 \neq 0$, the inverse matrix is non singular, still circulant and its first row is

$$\left[\mathbf{\Sigma_v}^{-1}(n)\right]_{1,\cdot} = \frac{1}{\sigma_w^2(L + \sigma_w^2)} \left[(L-1) + \sigma_w^2, \mathbf{0}_{n-1}^T, -1, \mathbf{0}_{n-1}^T, -1, \cdots, 0\right]. \tag{9.10}$$

The log-likelihood function becomes

$$\begin{aligned}
\Lambda(n) &= \log\left[\frac{1}{(2\pi)^{N/2} \parallel \mathbf{\Sigma_v}(n) \parallel^{1/2}}\right] + \\
&- \frac{1}{2\sigma_w^2(L+\sigma_w^2)}\left(((L-1)+\sigma_w^2)\sum_{k=1}^{N}|v(k)|^2 - \sum_{k=1}^{N}\sum_{m=1}^{L-1} v^*(k)v(k+mn)_N\right) = \\
&= \left[\log\left(\frac{1}{(2\pi)^{N/2} \parallel \mathbf{\Sigma_v}(n) \parallel^{1/2}}\right) - \frac{1}{2\sigma_w^2(L+\sigma_w^2)}(L+\sigma_w^2)\sum_{k=1}^{N} v^*(k)v(k)\right] + \\
&- \frac{1}{2\sigma_w^2(L+\sigma_w^2)}\left(-\sum_{k=1}^{N} v^*(k)v(k) - \sum_{k=1}^{N}\sum_{m=1}^{L-1} v^*(k)v(k+mn)\right) \\
&= \log\left[\frac{1}{(2\pi)^{N/2} \parallel \mathbf{\Sigma_v}(n) \parallel^{1/2}}\right] - \frac{1}{2\sigma_w^2}\left(\sum_{k=1}^{N}|v(k)|^2\right) + \\
&+ \frac{1}{2\sigma_w^2(L+\sigma_w^2)}\left(\sum_{k=1}^{N}\sum_{m=0}^{L-1} v^*(k)v(k+mn)_N\right)
\end{aligned} \tag{9.11}$$

We assume that the first term as constant with respect to n. Neglecting additive terms that do not depend on n, which are not involved in the maximization of the log-likelihood function, we have

$$\begin{aligned}
P_{\mathrm{ML}} &= \mathrm{argmax}_n \quad \frac{1}{2\sigma_w^2(L+\sigma_w^2)}\left(\sum_{k=1}^{N}\sum_{m=0}^{L-1} v^*(k)v(k+mn)_N\right) = \\
&= \mathrm{argmax}_n \quad \frac{1}{(L+\sigma_w^2)}\sum_{m=0}^{L-1} C(mn).
\end{aligned} \tag{9.12}$$

9.2.1 Low Complexity Implementation of ML Detection

We propose a method that estimates the periodicity without initially estimating the correlation. In fact, if $v(k)$ describes a large number of periods, i.e. $L \gg \sigma_w^2$, we have

$$\begin{aligned}
P_{\mathrm{ML}} &= \mathrm{argmax} \quad \Lambda(n) = \\
&= \mathrm{argmax} \quad \frac{N}{2\sigma_w^2(L+\sigma_w^2)}\left(\sum_{m=0}^{L-1} C(mn)\right) = \\
&= \mathrm{argmax} \quad \frac{1}{L+\sigma_w^2}\sum_{m=1}^{L-1} C(mn) \approx \mathrm{argmax}_n \quad e(n) = P_{\mathrm{LCML}}.
\end{aligned} \tag{9.13}$$

For each candidate period $n \in \mathcal{I}_{\mathcal{P}}$, we divide the signal $v(l)$ in L blocks of length n, with $Ln \leq N$, i.e. we make the change of variable $l = k + in$ with $k = 1 \dots n$, $i = 1 \dots L$. If the period P is correct, then $v(k + jP) = v(k + iP)$, with i, j the block index. The function $e(n)$ is a linear combination of the autocorrelation function evaluated on multiple values of n, i.e.

$$\begin{aligned} e(n) &= \frac{1}{n} \sum_{k=1}^{n} \frac{1}{L^2} \sum_{i=0}^{L-1} \sum_{j=0}^{L-1} v(k + in) v^*(k + jn) = \\ &= \frac{1}{L} \sum_{m=0}^{L-1} C(mn). \end{aligned} \tag{9.14}$$

However, $e(n)$ can also be computed as

$$e(n) = \frac{1}{n} \sum_{l=1}^{n} |q(l, n)|^2, \quad n \in \mathcal{I}_{\mathcal{P}}. \tag{9.15}$$

where

$$q_L(l, n) = \frac{1}{L} \sum_{m=0}^{L-1} v(l + mn), \quad k = 1, \cdots, n. \tag{9.16}$$

We denote this method as low complexity ML detection (LCML) method; in fact, it allows a low complexity implementation of the ML strategy, as we discuss in Sec. 10.4.4. If the signal is periodic with period $\bar{n}$ and it has zero mean, the function $e(n)$ of (9.15) is periodic with the same period of the signal $v(\cdot)$. The intuition behind this method is that the sum in (9.16) allows for an averaging of the noise thus reducing the noise impact on the final estimate.

If all the processes are ergodic, we have

$$\begin{aligned} &\lim_{L \to \infty} q_L(k, n) = E[v(k + in)] = \\ &= v(k) \delta(n - m\bar{P}), \quad n \in \mathcal{I}_{\mathcal{P}}, m \in \mathcal{Z}, \end{aligned} \tag{9.17}$$

where the expectation is done with respect to i, and

$$e(n) = \sigma_w \cdot \delta(n - m\bar{P}), \quad n \in \mathcal{I}_{\mathcal{P}}, m \in \mathcal{Z}. \tag{9.18}$$

Asymptotically, the LCML estimation tends to a periodic delta function with period equal to the period to be estimated.

As illustrated in Subsection 9.3.1, the average autocorrelation $e(n)$ is affected by a noise component with mean $\frac{\sigma_w^2}{L}$. Therefore, if an estimate of the noise power is available, we can further refine the LCML method by removing the mean value of the noise component, obtaining the LCML2 method

$$P_{\text{LCML2}} = \text{argmax}_n \quad \frac{1}{L}\sum_{m=0}^{L-1} C(mn) - \frac{\sigma_\eta^2}{L}. \tag{9.19}$$

9.3 Vital Signs Period Estimation

Remote sensing of vital signs using UWB radar technology is a possible application of the period estimation problem. We assume a monostatic configuration, where the target chest is in front of the radar device in a line of sight configuration, and the receiver perfectly estimates and cancels all the replicas referring to the static part of the channel, using background subtraction techniques [65, 66]. At the receiver, a filter matched to the UWB pulse is applied and after sampling we obtain a signal $v(k)$ as in (8.20). We verified that the shape of $v(k)$ changes significantly with many factors, e.g. the angle of incidence, the radar distance, the target position. In general, $v(k)$ is a non stationary signal, mainly because of the irregular nature of the respiration process. Therefore, it can not be considered as a periodic signal in strict sense. We instead model it as locally periodic on N samples.

Period estimation can benefit from the wide knowledge on heart beating and respiration features provided by medicine. In fact, the human physiology provides upper and lower bounds to the vital signs rate, depending on target parameters, e.g. age and resting/activity of the target [61]. In particular, for a healthy adult target, the ranges of the period durations are $[0.5\text{s}; 10\text{s}]$ for respiration, and $[0.3\text{s}; 1.2\text{s}]$ for heart beating, corresponding to a heart rate range of $50 - 200$ beats per minute (bpm).

We observe that $\tilde{v}(k)$ is a zero mean signal, since the average has been nulled by background subtraction.

9.3.1 Theoretical SNR Evaluation

In this section, we analytically describe the statistical noise description for the functions $C(n)$ and $e(n)$, in order to investigate how the presence of noise affects the methods CORR and LCML, respectively.

9.3.2 Autocorrelation

By considering the presence of noise and finite N, we have

$$\begin{aligned} C(n) = \frac{1}{N}\sum_{l=1}^{N} v(l)v^*((l+n)_N) = \tilde{C}(n) + \\ + \frac{1}{N}\sum_{l=1}^{N} [\tilde{v}(l)w^*((l+n)_N) + w(l)v^*((l+n)_N)] + \\ + \frac{1}{N}\sum_{l=1}^{N} w^*(l)w((l+n)_N). \end{aligned} \tag{9.20}$$

where

- $\tilde{C}(n) = E[v(l)v^*(l+n)]$ is the autocorrelation function;
- $\eta_A(n) = 1/N\sum_{l=1}^{N}[v(l)w^*((l+n)_N) + w(l)v^*((l+n)_N)]$ is the mixed noise and signal term. To further elaborate this term, we denote with η_R, η_I the real and imaginary part of η_A, respectively. They are both Gaussian random variables with zero mean and variance $\sigma_w^2/2$. Then, we have

  $$\begin{aligned} \eta_A(n) = \frac{1}{N}\sum_{l=1}^{N} [v((l-n)_N)w^*(l) + w(l)v^*((l+n)_N)] = \\ \frac{1}{N}\sum_{l=1}^{N} \eta_R(lTs)[v^*((l+n)_N) + v((l-n)_N)] + \eta_I(l)[v^*((l+n)_N) - v((l-n)_N)], \end{aligned} \tag{9.21}$$

  in which the two terms inside the sum are independent, Gaussian, and zero mean. The variance of the first term is $\sigma_w^2[2\sigma_v^2 + 2C(2n)]/2$ while the variance of the second one is $\sigma_w^2[2\sigma_v^2 - 2C(2n)]/2$. Therefore, $\eta_A(n)$ is a zero mean Gaussian random process with variance $2\sigma_w^2\sigma_v^2/N$.
- The last term $\eta_B(n) = 1/N\sum_{l=1}^{N} w(l)^*w((l+n)_N)$ is the sum of random variables whose probability distribution is a modified Bessel function of null order $K_0(x)$ and statistical power σ_w^4. Since $w(\cdot)$ are independent identically distributed (iid) random variables with zero mean, the statistical power of $\eta_B(n)$ is σ_w^4/N.

In the presence of a noisy observation of a signal, the conventional approach to estimate the correlation is characterized by a noise contribution which can be separated in two terms. One has variance $2\sigma_w^2\sigma_v^2/N$ and the other has variance σ_w^4/N. The signal to noise ratio of $C(\bar{P})$ is

$$\mathrm{SNR}_{\mathrm{corr}} = \frac{\mathrm{E}[|\tilde{C}(n)|^2]}{2\sigma_w^2\sigma_v^2/N + \sigma_w^4/N} = \frac{\sigma_w^4}{2\sigma_w^2\sigma_v^2/N + \sigma_w^4/N}. \tag{9.22}$$

9.3.3 Low Complexity ML

In order to obtain a low complexity ML (LCML) method we note that if L does not approach infinity, (9.16) becomes

$$q_L(k,n) = \frac{1}{L}\sum_{i=0}^{L-1} v(k+in) + \frac{1}{L}\sum_{i=0}^{L-1} w(k+in), \quad k = 1, \cdots, n; \tag{9.23}$$

the term $\eta_1(k,n) = 1/L\sum_{i=0}^{L-1} w(k+in)$ in (9.23) is a Gaussian random process with zero mean and variance $\sigma_1^2(n) = \sigma_w^2/L$. We can then write

$$\begin{aligned} e(n) &= \frac{1}{n}\sum_{k=1}^{n}\left(\eta_1(k,n) + \frac{1}{L}\sum_{i=0}^{L-1} v(k+in)\right)\left(\eta_1^*(k,n) + \frac{1}{L}\sum_{j=0}^{L-1} v^*(k+jn)\right) = \\ &= \frac{1}{n}\sum_{k=1}^{n}\left[|\eta_1(k,n)|^2 + \frac{1}{L^2}\sum_{i=0}^{L-1}\sum_{j=0}^{L-1} v(k+in)v^*(k+jn) + \frac{1}{L}\eta_1(k,n)\sum_{i=0}^{L-1}[v^*(k+in)] + \right. \\ &\left. + \frac{1}{L}\eta_1^*(k,n)\sum_{i=0}^{L-1}[v(k+in)]\right] = \\ &= \eta_3(n) + \frac{1}{L^2}\sum_{i=0}^{L-1}\sum_{j=0}^{L-1}\tilde{C}((i-j)n) + \eta_2(n), \end{aligned} \tag{9.24}$$

where

- The first term is

$$\eta_3(n) = \frac{1}{n}\sum_{k=1}^{n}|\eta_1(k,n)|^2 = \frac{\sigma_1^2}{n}\sum_{k=1}^{n}|\frac{\eta_1(k,n)}{\sigma_1}|^2 = \frac{\sigma_1^2}{2n}X \tag{9.25}$$

  where X is a chi-square distributed random variable of order $2n$ χ^2_{2n}[1]. The expected value and variance of η_3 is

$$E[\eta_3] = \frac{\sigma_1^2}{2n}E[X] = \sigma_1^2 = \frac{\sigma_w^2}{L}, \tag{9.26}$$

---

[1] The order is the number of terms of the sum; in our case is $2n$ because $\eta_1(k,n)$ is a complex number.

$$\sigma_{\eta_3}^2 = \frac{\sigma_1^4}{4n^2}\sigma_X^2 = \frac{\sigma_1^4}{n} = \frac{\sigma_w^4}{L^2 n}. \tag{9.27}$$

We notice how the mean of η_3 can provide an estimate of the statistical power σ_w^2. We observe that

- $C((i-j)n)$ is an estimate of the autocorrelation function evaluated on $(i-j)n$; the quality of the estimation increases with n. However, since the value of Ln is constant, we observe from (9.24) that for low values of n the average on multiple values of n is performed on a higher number of terms.

- $\eta_2(n) = \frac{1}{Ln}\sum_{k=1}^{n} 2\mathrm{Re}\left[\eta_1(k,n)\sum_{l=0}^{L-1} v^*(k+ln)\right]$ is obtained reminding that $A^*B = (AB^*)^*$, where A, B are complex numbers. Both the real and imaginary part of η_1 are Gaussian, while $\tilde{v}(\cdot)$ is a deterministic process. Then, $\eta_2(n)$ is a Gaussian random process with zero mean and statistical power

$$\begin{aligned} \sigma_2^2(n) &= \frac{4}{n^2L^2}\frac{\sigma_1^2(n)}{2}\sum_{k=1}^{n} E\left[|\sum_{l=0}^{L-1} v^*(k+ln)|^2\right] = \\ &= \frac{2}{n}\sigma_1^2(n)A(n) \end{aligned} \tag{9.28}$$

  where $A(n) = E\left[|\frac{1}{L}\sum_{l=0}^{L-1} v(k+ln)|^2\right] = \frac{1}{L}\sum_{l=0}^{L-1} C(ln)$; in particular, $A(n) = \sigma_w^2$ if $n = m\bar{P}$, $m \in \mathcal{Z}$. We note also that $A(n)$ does not depend on k.

As done in the previous subsection, we can define the SNR for the proposed method for $n = \bar{P}$ as

$$\mathrm{SNR}_{\mathrm{prop}} = \frac{\left|\frac{1}{L^2}\sum_{i=0}^{L-1}\sum_{j=0}^{L-1}\tilde{C}((i-j)n)\right|^2}{2\sigma_w^2\sigma_s^2/N + \sigma_w^4/(L^2n)} = \frac{\sigma_w^4}{2\sigma_w^2\sigma_s^2/N + \sigma_w^4/(L^2n)}. \tag{9.29}$$

The SNR of the two methods are very close, cf. (9.22) with (9.29). However, the distribution of the noise is different, and the shape of the the useful signal too. In particular, by recalling (9.18), we notice that with the increase of L the useful signal in the proposed method tends to be a delta function whose exact position can be detected in a robust way. According to this analysis, we introduce a third method LCML-2, which approximates the ML and is based on the function

$$e2(n) = e(n) - \frac{\sigma_w^2}{L}. \tag{9.30}$$

9.3.4 Simulation Setup

The ML method is compared with the state of the art algorithms, i.e.

- the AMDF method, which minimizes the average magnitude of the difference function between adjacent periods [74];
- the algorithm based on the weighed autocorrelation function (WEIGHT), which has been shown to improve the autocorrelation based detection algorithm [75];
- the method based on the Welch periodogram (WELCH), which evaluates the peak of the Welch periodogram [76];
- the Music based algorithm (PMUSIC) [77].

In the following, we show that the proposed LCML method outperforms the state of the art algorithms, as expected since it represents a low complexity implementation of the ML estimation strategy.

Chapter 10

Experiment Results

10.1 System Description

We consider a TD PulsON 210 IR-UWB system for the detection of vital signs of a target in an indoor environment. As described in Section 5.2.2, the transmitted wave $p(t)$ is a Gaussian pulse, and then the transmitted signal is

$$s(t) = \sum_{n=-\infty}^{+\infty} \frac{e^{-\left(\frac{(t-nT_{REP})^2}{2\sigma^2}\right)}}{\sqrt{2\pi}\sigma} \cos(2\pi f_C t + \phi_0), \tag{10.1}$$

where T_{REP} is the pulse repetition period and σ is the pulse variance, depending on its bandwidth. The P210 Standard waveform has a 10 dB bandwidth $B = 2.2$ GHz, and a central frequency $f_C = 4.2$ GHz; in the following we indicate as $f_i = 3.1$ GHz the lower limit of the band. The duration of the impulse response is $T_P = 1000$ ps (99.91% of the total energy), or $T_P = 800$ ps (99.3%).

We note that the maximum sample period verifying the sample theorem is $T_{samp} = \frac{1}{B} = 454.5$ ps; this is also the maximum resolution we can obtain on the channel impulse response estimate. However, the sample theorem is not strictly verified. Aliasing is introduced by the presence of real filters and non finite duration of the impulse response. We set the value of the pulse repetition frequency (PRF) to 9.611 MHz.

We define a slot as a set of K transmitted pulses coded by a pseudo-noise sequence $\nu(k) \quad k = 1, \cdots, K$. We observe that the maximum channel impulse response (CIR) length that can be included in a pulse period is $\frac{1}{PRF} \sim 1\mu$s, and the corresponding distance of the farthest reflector is 15 m. In our scenario we assume that this

condition is verified, and then for each pulse repetition period the receiver gets the whole set of replicas generated by the corresponding pulse, and interference between adjacent pulse repetition intervals (ISI) is absent.
According to the PulseOn notation, we define as *waveform* the set of received replicas; in a ideal scenario, i.e. absence of ISI and distortion, and a discrete and finite CIR, waveform is given by the convolution of the CIR with the transmitted pulse. Based on the waveforms received in each slot, the receiver provides a *waveform scan* by a weighted average of the received symbols. The packet transmission interval is 1 ms, i.e., two adjacent waveform scans refer to times t_0, t_0+1 ms; we assume then that the coherence period of vital sign processes is higher than 1 ms, i.e., the processing of the received signal in a slot does not affect the vital signs detection.

10.1.1 Hardware Configuration

The PulseON 210 kit provides several utilities and programming examples both for communication and sensing purpose. All the applications consist of two components: an embedded side and a host side. The embedded component runs on the device using the UWB Kernel included with the hardware. The host side runs on a PC, where simulation parameters are set by the user through a graphic interface (API). The embedded side and the host side are linked by a Ethernet connection and controls the radio using the UWB Kernel included with the hardware. The host side runs on a PC; and through the network sends commands to and receives status info and radar scans from the embedded component.

10.1.2 Parameters Description

We describe in the following the main parameters of our experiment setup

Link Rate The Ethernet link connecting the embedded side on the device with the host side on the PC has a rate LR of 600 kbps.

Pulse Repetition Frequency The PRF can be selected by the user; in our scenario it has always been set to 9.6 MHz. Therefore, the pulse repetition period T_S is about 0.1μs.

Hardware Integration The hardware Integration (HWI) is the number of pulses that are integrated to build a sample. $\mathrm{HWI} \in \{32, 64, 128, 256, 512\}$.

Software Integration The software Integration (SWI) is the number of samples that are averaged at each step to form a single sample value, i.e., at each scan step, SWI samples are summed to yield the current sample. $\mathrm{SWI} \in \{2, 4, 8, 16, 32, 64\}$.

Pulses per sample Pulses per sample (PPS) is the number of UWB radio pulses required for each scan sample: $\mathrm{PPS} = \mathrm{HWI} \cdot \mathrm{SWI}$.

Start position for the scan windowing (ST) : It denotes the start position of the scan windowing, evaluated in feet [ft] or in bins [bins].

Stop position of the scan windowing (EN) It denotes the stop position of the scan windowing, evaluated in feet [ft] or in bins [bins].

Scan window The limited capacity of the Ethernet link $LP = 600$ kbps is a severe bound on the received data rate. Furthermore, the high level of noise suggests to set an high value of HWI and SWI. Therefore, the scan is limited to a short window around the position of the target, which is supposed to be known. From the theoretical point of view, this operation is equivalent to taking the maximum scan size, whose length is equal to the pulse repetition period, and applying the window $\mathrm{SW} = \mathrm{EN} - \mathrm{ST}$ [bins].

Step size The step size (STEP), provided in [bins], or waveform resolution, is equal or higher than $\frac{1}{B}$.

Number of samples in a scan The number of samples in a scan (L_S) is given by $\mathrm{L_S} = \frac{\mathrm{SW}}{\mathrm{STEP}}$. It is a multiple of 32.

Pulse per waveform The number of pulses per waveform (PPW) is the number of UWB radio pulses required for the entire waveform:

$$\mathrm{PPW} = \mathrm{PPS} * \mathrm{L_S} = \mathrm{HWI} \cdot \mathrm{SWI} \cdot \frac{\mathrm{SW}}{\mathrm{STEP}}.$$

Scan rate The scan rate (SR) is the number of scans per second: $\mathrm{SR} = \frac{\mathrm{PRF}}{PPW}$. The maximum scan rate is

$$\mathrm{maxSR} = \frac{\mathrm{maxPRF}}{\mathrm{minHWI} \cdot \mathrm{minSWI} \cdot \mathrm{minSW}} = \frac{9.6 \cdot 10^6}{32 \cdot 2 \cdot 2} = 586 \quad \mathrm{kbps} < \mathrm{LR}.$$

10.1.3 Practical Scheme

In Chapter 8 we described the theoretical receiving scheme, performed in ideal conditions; a scheme of the theoretical approach is described in Fig. 10.1; we note that the sampling of the received signal is performed at a frequency of $U \cdot B$, where U is the upsampling factor, and the corresponding sampling period is

$$STEP = \frac{1}{U \cdot B}$$

; then, for each slot, where vital signs are supposed to be a constant, our theoretical scheme performs an averaging.
The practical scheme has to deal with a non ideal scenario and hardware constraint. In particular, in our scenario, we have a limited capacity of the Ethernet link $LP =$ 600 kbps, and limited complexity available.

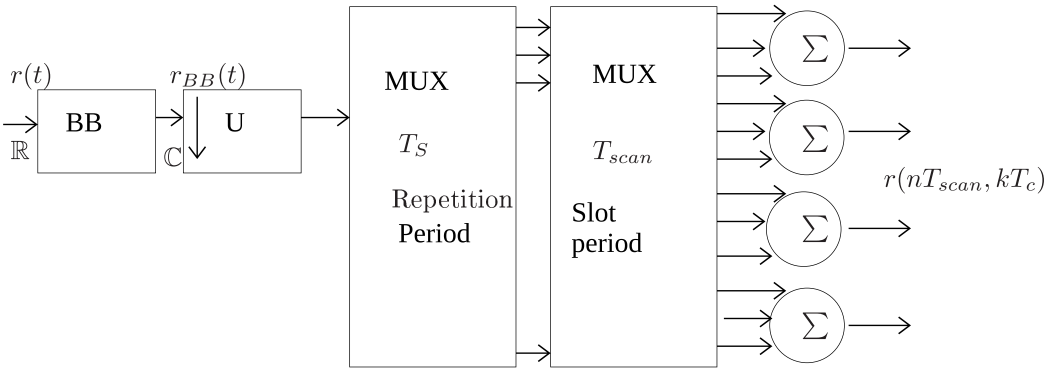

Figure 10.1: Theoretical receiving scheme.

For the considered hardware, the sampling of the received signal is not performed with a period $STEP$. In fact, the device takes one sample for each pulse repetition period, while the theoretic receiver saves all the L_S samples describing the waveform. Therefore, the resulting device is simpler, because the sampler period is $\frac{1}{PRF} + \frac{1}{UB} \approx$ 0.1μs instead of the theoretical $\frac{1}{UB} < 0.5$ ns, i.e., 3 orders of magnitude slower; on the other hand, the SNR of the resulting scan is L_S times lower with respect to the theoretical one. A key role on this simplicity to SNR loss ratio is given by the presence of the scan window; in fact, the device takes the samples only inside the scan window, and neglects the other samples of the waveform. On the other hand, this approach allow a better focus on the desired window, which can be described with an high number of samples. This upsampling factor on the window

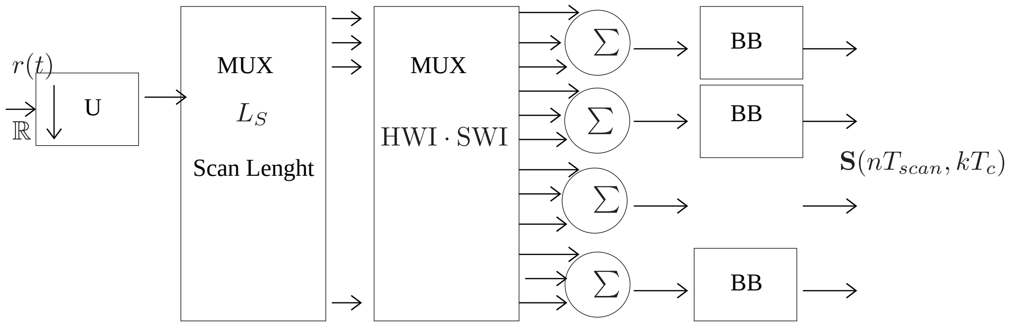

Figure 10.2: Practical receiving scheme.

10.1.4 Baseband Operation

After the pre processing operations performed by the PulseOn device, the received signal $r(n,k)$ is a bandpass signal, function of variables n, index of the current scan, and k, index of the current delay in the received signal of scan n,

$$r(n,k) = \sum_{i=1}^{L_s} \gamma_i(n)\cos(2\pi f_C k + \phi_i(n))\delta(k-i) + \eta(n,k); \tag{10.2}$$

In the practical scheme, as shown in Fig. 10.2, baseband operation is performed on the k dimension; if $f_C T_{scan} \in Z$, and if the low pass filter has a impulse response shorter than the pulse repetition period, performing the baseband operation on each waveform scan is equivalent to performing it before the sampling process. In fact, if the sampling process complies the sampling theorem, it is equivalent to perform the baseband operation before or after the sampler. Therefore, the baseband operation performed in the theoretical scheme is

$$r_{BB}(lT_c) = \sum_{m=-\infty}^{+\infty} r(mT_c)e^{j2\pi f_C mT_c} g_{LP}(lT_c - mT_c), \tag{10.3}$$

where $g_{LP}(lT_c)$ is the low pass filter. Then, by writing $lT_c = n_l T_{scan} + k_l T_c$ and $mT_c = n_m T_{scan} + k_m T_c$

$$
\begin{aligned}
r_{BB}(n_l T_{scan} + k_l T_c) = & \sum_{n_m=-\infty}^{+\infty} \sum_{k_m=-\infty}^{+\infty} r(n_m T_{scan} + k_m T_c) e^{j2\pi f_C n_m T_{scan} + k_m T_c} \cdot \\
& \cdot g_{LP}(n_l T_{scan} + k_l T_c - n_m T_{scan} - k_m T_c) = \qquad (10.4) \\
= & \sum_{k_m=-\infty}^{+\infty} r(n_m, k_m) e^{j2\pi f_C k_m T_c} g_{LP}(k_l T_c - k_m T_c);
\end{aligned}
$$

which is equivalent to the baseband operation performed on each waveform scan in the practical scheme.

However, the presence of the window scan in the practical scheme provides only a portion of the waveform to the low pass filter; therefore, in general the baseband waveform evaluated with the practical scheme is not equivalent to the theoretical baseband waveform.

10.2 Signal Processing

Both for theoretical and practical scheme, the receiver gets a complex matrix $\mathbf{S}$, whose rows are the baseband waveform scans; the i-th columns of $\mathbf{S}$ is the time variation of the i th sample of the scan window, sampled at period T_{scan}. The first step of signal processing is the background subtraction; it is performed as it is described in the theoretical model, in Chapter 8. As described in Section 8.3.1, we combine the samples describing each received replica, to determine the parameters of the corresponding channel tap, i.e.

$$
\tilde{v}(kT_{scan}) = \mathrm{max}_{n_K} \{ r_T * g \quad (n_K T_c + kT_{scan}) \}. \qquad (10.5)
$$

where $g(t)$ is a generic filter. From the theoretical point of view, in absence of ISI, the combination that maximizes the SNR is provided by the matched filter, i.e.

$$
g_1(k) = p^*(-k + L_S/2)\,. \qquad (10.6)
$$

However, the practical scenario introduces some new condition on the combination problem, and its solution. First of all, the scan window may include portions of replicas; in fact, the sampling algorithm of the device suggests to have small scan windows, in order to improve the averaging (HWI and/or SWI) with the same scan rate. Secondly, distortion may have occurred during transmission, due to the interaction with the human body, or to the presence of multiple scatterers whose delays are closer then $1/B$. For this reason, together with the theoretical math filter, we consider the *estimated matched filter*, and the *average filter*.

Estimated matched filter The theoretical approach suggests as optimum combination the filter matched to the transmitted pulse in a AWGN scenario. We assume the received baseband matrix $\mathbf{S}$ to be the result of a unknown transmitted pulse propagated in an AWGN scenario; therefore, we assume all variations on the channel behavior, including the variations due to vital signs, as a Gaussian white noise. We estimate the pulse from the received baseband matrix $\mathbf{S}$ as

$$\hat{p}(k) = \frac{1}{N_{scan}} \sum_{j=1}^{N_{scan}} \mathbf{S}(j,k), \tag{10.7}$$

and then the estimated matched filter is

$$g_2(k) = \hat{p}^*(-k + L_S/2). \tag{10.8}$$

Average filter We propose as the simplest solution a rectangular filter, i.e.,

$$g_3(k) = \mathrm{rect}\left(\frac{k - L_S/2}{L_S}\right). \tag{10.9}$$

Fig. 10.3 shows the impulse response of the three filters proposed; it has been obtained in an ideal scenario, with periodic vital sign, AWGN channel, scan window equal to a replica. We observe that the shape of the estimated pulse is very close to the theoretical pulse.

The average SNR of the resulting sample as a function of the average SNR before the combination is illustrated in Fig. 10.4; we can observe that the theoretical and estimated matched filter provide the same SNR gain of 18 dB, corresponding to the upsampling factor $U = 64$ used in our scenario. We also observe that the averaging provides almost the same performance of the optimal approach.

10.3 Experimental Results on Signal Modulation

As a first experiment, we evaluate the SNR of the system; we verified that, if the target breaths at a regular rate, the SNR is about 30 dB, while if the target holds

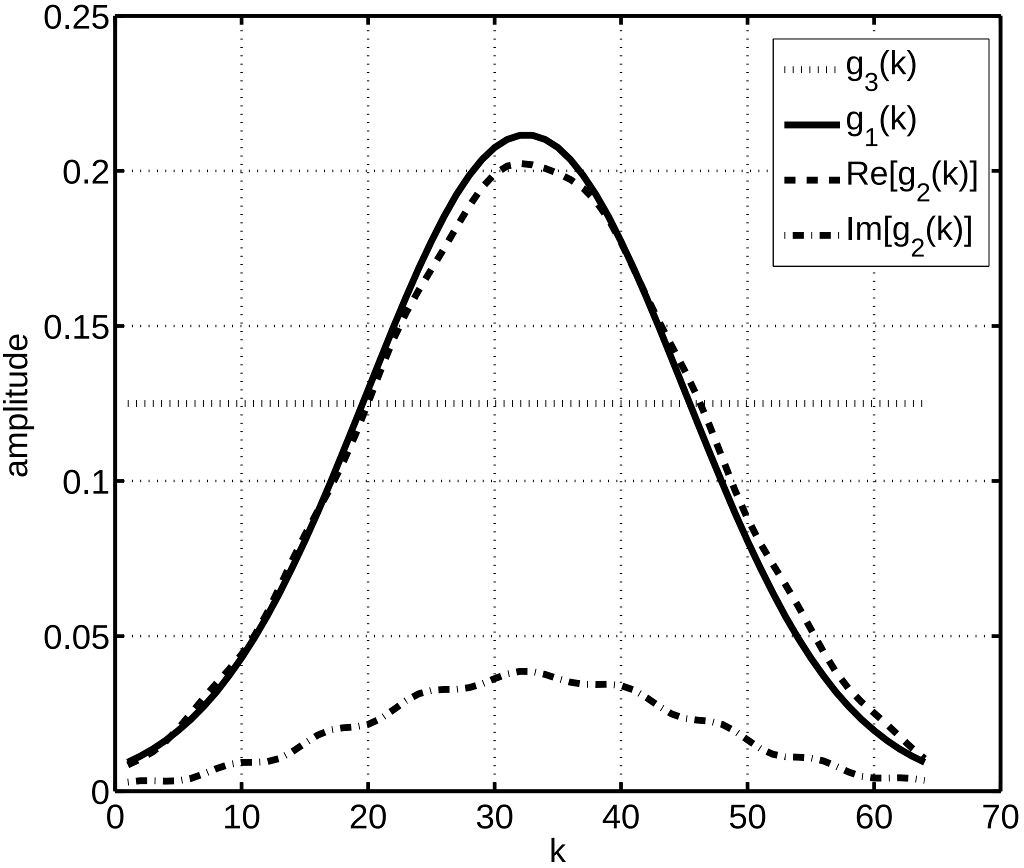

Figure 10.3: Normalized matched filters shapes

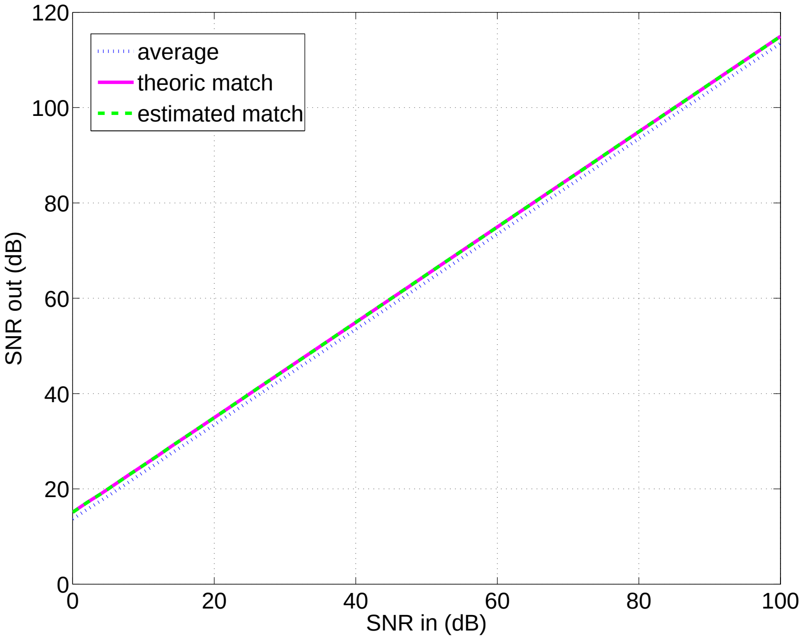

Figure 10.4: SNR of the signal resulting from the combination of the samples in a scan window

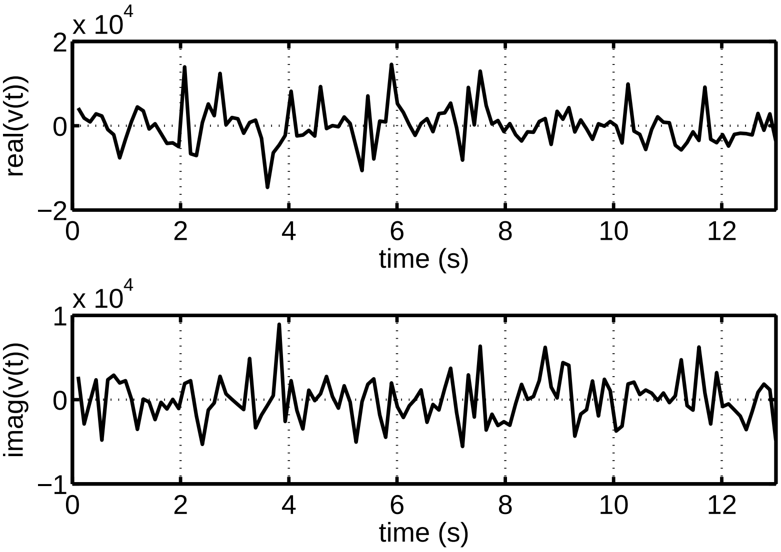

Figure 10.5: Vital sign signal $v(t)$ obtained without the target

his breath the SNR is about 5 dB; the actual values of the SNR depend on many factors;therefore these values are suggestive of the actual SNR. Fig. 10.5 shows the absolute value and the phase of the $v(t)$ when the target is not present; we can see that neither the absolute value nor the phase is modulated.

As a intermediate step we evaluate the normalized signal $v(t)$ with a 5 cent coin covered by a metallic film and oscillating at a known frequency of 2 Hz. As shown by Fig. 10.6, in this case we can observe a remarkable phase modulation, while the amplitude modulation is less pronounced. In fact, in this case the scattering surface is very small, and then the phase modulation is the same for each scattering point. In other words, the scatterer does not provide a sufficient phase diversity to provide an amplitude modulation. However, the wide band nature of the signal provides a slight amplitude modulation.

Finally, the experiment with the target was performed; the target was asked to be still and to sit with the chest in front of the radar device. As illustrated in Fig. 10.7, in this case we can observe an evident modulation on both absolute value and phase of $v(t)$.

The theoretical analysis for a wideband signal performed for a 2.2 GHz system, compliant with FCC rules, shows that the received signal is affected both in phase and amplitude parameters by vital signs; simulation results validates the theoretical analysis, showing that the amplitude modulation is due to both the wideband nature

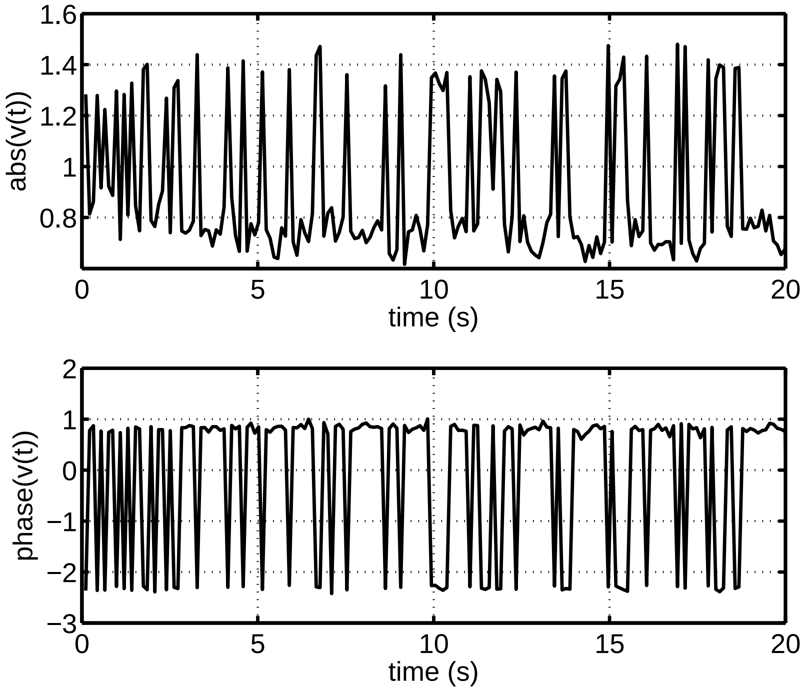

Figure 10.6: Normalized vital sign signal $v(t)$ obtained in the 5 cent experiment.

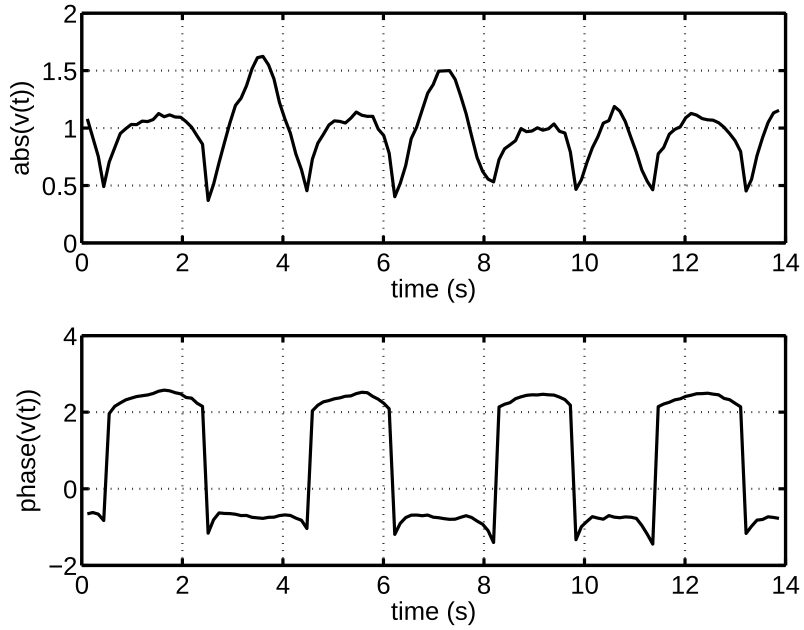

Figure 10.7: Normalized vital sign signal $v(t)$ obtained with the target breathing.

of the transmitted pulse, and to a multiple scattering effect provided by the chest surface.

10.4 Detection Techniques

10.4.1 Theoretical Comparison

We first consider the periodic signal $v(k) = \exp(j2\pi kP)$, with $k = 0, 1, \ldots 1000$ and $P = 5$, corrupted by an additive white Gaussian noise. The signal to noise ratio is defined as SNR=$1/\sigma_w^2$. To compare the two methods we evaluate the normalized (with respect to the period) mean error (MSE) defined as

$$\rho = \mathrm{E}\{|P - P_{\text{est}}|\}/P \tag{10.10}$$

where P_{est} is the period estimate, e.g. P_{CORR} or P_{LCML}. We express this error in terms of percentage of the period. The signal to noise ratio is defined as SNR=$1/\sigma_\eta^2$. We note that in this scenario ML algorithm is not optimal; in fact, the signal $v(k)$ does not comply with the assumption of i.i.d. Gaussian signal. Still, this is a signal of interest in many applications. Fig. 10.8 shows the normalized MSE as a function of N/P for SNR=-5 dB. We observe that the proposed LCML method outperforms the state of the art algorithms, as expected since it represents a low complexity implementation of the ML estimation strategy. In particular, the knowledge of the noise power exploited by LCML2 provides the best performance.

Fig. 10.8 shows the MSE as a function of N, represented in terms of number of periods for SNR=-5 dB. We observe that the proposed LCML method outperforms the state of the art algorithms, as expected since it represents a low complexity implementation of the ML estimation strategy. In particular, the knowledge of the noise power exploited by LCML2 provides the best performance.

Fig. 10.9 shows the same simulation results with an SNR=0dB. The results are similar, as they still indicate an advantage of the proposed method with respect to the state of the art algorithms. However, the advantage become less and less relevant in terms of the envisioned application.

10.4.2 Experimental Comparison

The experiment is then performed with the target still and sitting at a distance of approximately 30 cm from the radar and with the chest facing the radar device. As

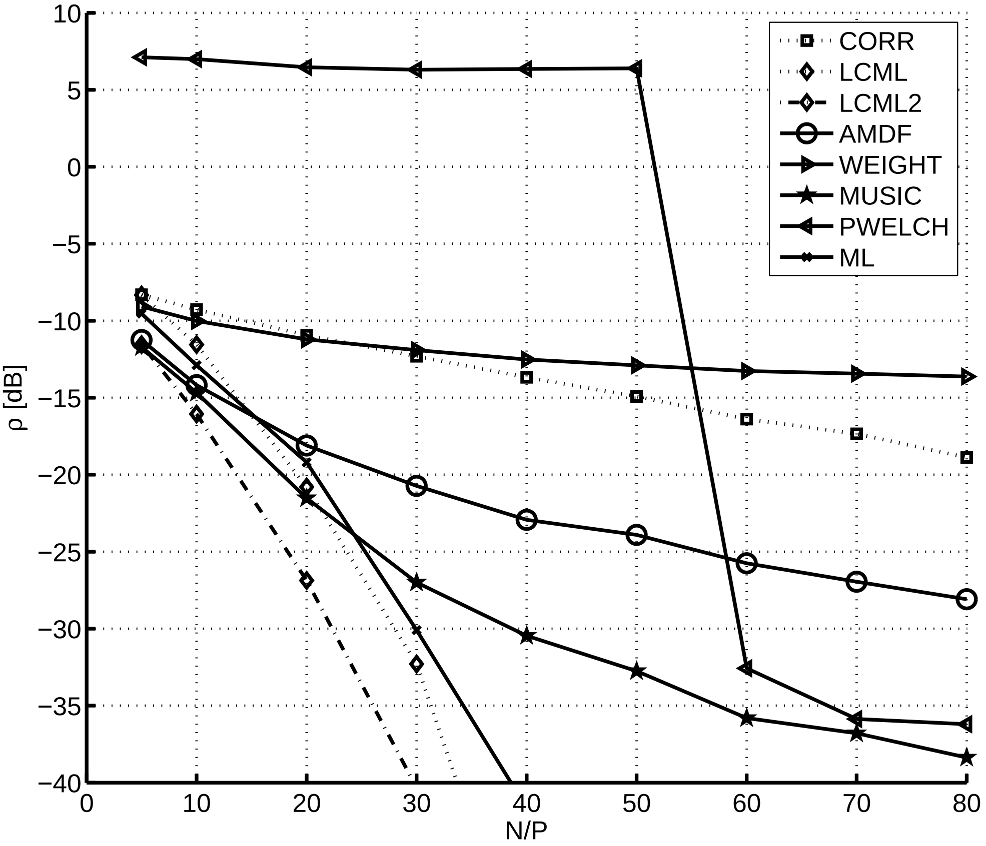

Figure 10.8: Normalized MSE of the estimated period as a function of N/P with SNR=-5dB

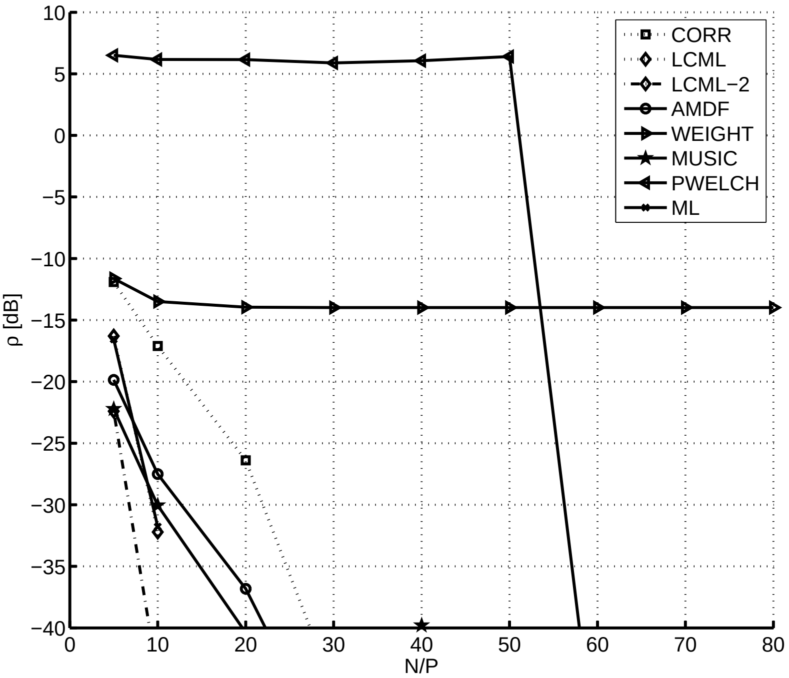

Figure 10.9: Normalized MSE of the estimated period as a function of N/P with SNR=0dB.

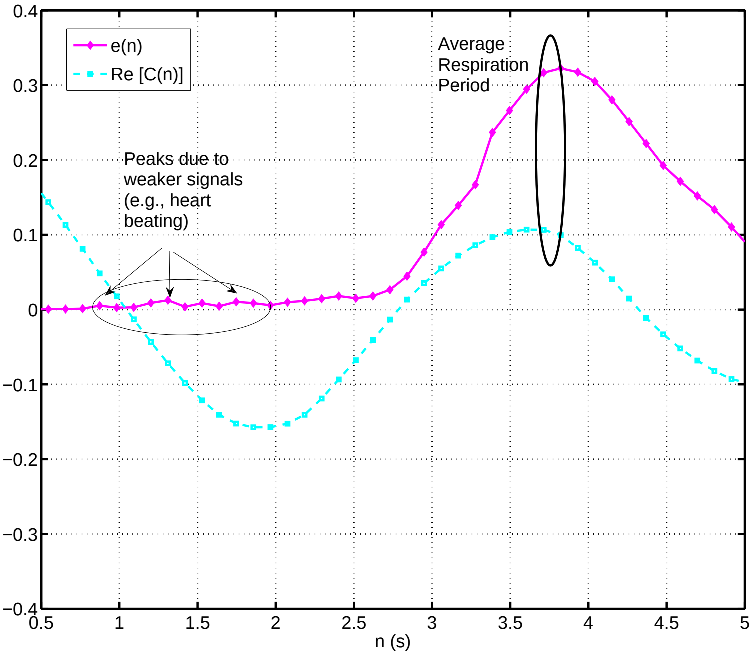

Figure 10.10: Normalized $e(n)$ and $Re[C(n)]$ functions obtained with the target breathing.

illustrated in Fig. 10.10, respiration rate can be easily detected by both the proposed method and the autocorrelation function. Both functions have been evaluated with an observation window of length $N = 10$s, for candidate periods $n \in \mathcal{I}_r$.

Furthermore, we observe that the proposed function $e(n)$ has weaker peaks in correspondence of a lower periods; there peaks are due to noise, to the non-periodic nature of the signal, and to the heart beating signal. The peak in correspondence of the lowest period is at about 0.85 s, which is the value of the target heart beating, 70 bpm. Although $e(n)$ provides information about the heart beating, it is not possible to distinguish the correspondent peak from spurious.

Therefore, in order to estimate the heart beating, we evaluate the functions with a shorter observation window; i.e., the signal $v(t)$ is divided into tokens of length $N = 2.2$ s, and the heart beating period is evaluated for each token. The value of N is the lowest window size allowing to detect the slowest heart beat for a healthy target, i.e. 50 bps; in fact, the functions are evaluated for candidate periods $n \in \mathcal{I}_h$. Fig. 10.11 shows an example of the resulting functions $e(n)$ and $C(n)$. In this case, the peak due to heart beating is clearly visible. By estimating the heart beating

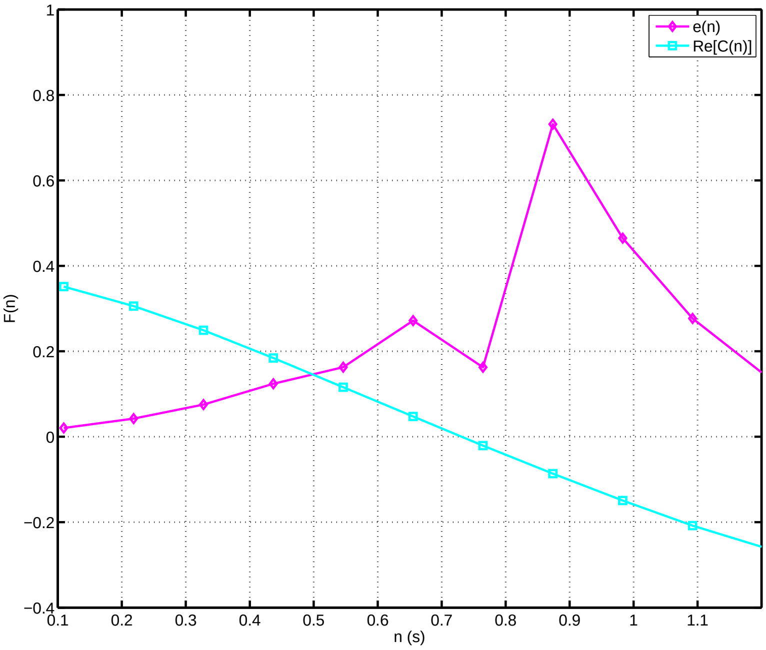

Figure 10.11: Normalized $e(n)$ and $Re[C(n)]$ functions obtained with the target breathing with $N = 2$s.

period according to eq. (9.5) and (9.13), the MSE of the detection is about 56% for the autocorrelation method, and 15% for the proposed method.

10.4.3 Detection Techniques Comparison

We consider a TD PulsON 210 IR-UWB system for the detection of vital signs of a target in an indoor environment [68]. Besides the radar device, the experimental setup is composed by the target, sitting in front of the radar in order to have a line of sight (LOS) with the chest, and a on-body sensor measuring the heart rate. The radar device faces the chest of the target who wears an on-body sensor detecting the heart rate. The experiment is performed with the target still and sitting at a distance of approximately 30 cm from the radar and with the chest facing the radar device.

The received signal is the sum of the respiration signal and the heart beating signal, which is weaker; although respiration rate can be easily detected, its unknown and time variant shape does not allow a simple subtraction of this signal from the received signal. Therefore, a low complexity heart rate detection has to be performed on the global signal. In order to estimate the heart beating, we consider a shorter observation window; i.e., the signal $v(k)$ is divided into tokens of length N from 2.2 to 4.4 s, and the heart beating period is evaluated for each token. In fact, higher values of N would include a breathing period, which strongly modulates the signal; furthermore, higher values of N would increase the detection delay, while we are interested on the real time value of heart beating. The minimum value of N corresponds to the lowest window size allowing to detect the slowest heart beat for a healthy target, i.e. 50 bps; in fact, the functions are evaluated for candidate periods $n \in \mathcal{I}_h$.

By estimating the heart beating period according to the proposed methods, we obtain the MSE values shown in Fig. 10.12. We observe that, while the state of the art algorithms are all affected by the periodicity of the respiration signal, which is the strongest contribution, for small periods the proposed method provides the best estimate of heart beating period. When longer tokens are considered, its estimation accuracy deteriorates due to the presence of respiration periodicity on $v(k)$, despite the higher number of heart beat period considered.

10.4.4 Computational Complexity

We evaluate the computational complexities of both ML and LCML, and then compare them with the complexity of the state of the art algorithms. Let μ be the cost of a complex multiplication and γ be the cost of a complex sum. Let also M be the dimension of $\mathcal{I}_P$, i.e. the number of candidate periods n. For the correlation based method the computational cost is

$$\mathcal{C}_{\text{CORR}} = M[N\gamma + N\mu]. \tag{10.11}$$

For the LCML method and AMDF method we have

$$\mathcal{C}_{\text{LCML}} = \mathcal{C}_{\text{AMDF}} = \sum_{n \in \mathcal{I}_P} \left(\frac{N}{n} + n \right) \gamma + M\mu, \tag{10.12}$$

while for the ML method we have

$$\mathcal{C}_{ML} = \mathcal{C}_{\text{CORR}} + \gamma M. \tag{10.13}$$

For the WEIGHT method we have

$$\mathcal{C}_{\text{WEIGHT}} = \mathcal{C}_{\text{CORR}} + \mathcal{C}_{\text{AMDF}} + N. \tag{10.14}$$

Complexity of the WELCH method depends on the algorithm implementation. The input signal is divided into N_w overlapping segments of size L_w; each segment is then windowed and processed by fast Fourier transform (FFT). The dominant component of complexity is due to FFT, i.e.

$$\mathcal{C}_{\text{WELCH}} \approx \mu[N \log 2(L_w) + N] + \gamma[N \log 2(L_w) + N]. \tag{10.15}$$

Similarly, complexity of PMUSIC algorithm depends on its implementation; however, the main components are the evaluation of the autocorrelation function, the eigen decomposition, and the pseudospectrum evaluation, i.e.

$$\mathcal{C}_{\text{PMUSIC}} \approx \mathcal{C}_{\text{CORR}} + \mu N^2 + \mu[N \log 2(N)]. \tag{10.16}$$

The proposed method requires significantly less complex multiplications (L instead of N) which are actually even less since they are used to calculate the absolute square value. In our simple case, with $N = 20$ and candidate heart beating periods $\mathcal{I}_P = 0.6 : 0.1 : 1.4$ s, corresponding to the range $45 - 120$ bpm, we have $\mathcal{C}_{\text{LCML}} = \mathcal{C}_{\text{AMDF}} = 220\mu + 220\gamma$ while $\mathcal{C}_{\text{CORR}} = 95\mu + 120\gamma$, $\mathcal{C}_{\text{WEIGHT}} = 335\mu + 340\gamma$, $\mathcal{C}_{\text{WELCH}} = 126\mu + 126\gamma$ and $\mathcal{C}_{\text{PMUSIC}} = 601\mu + 226\gamma$. The proposed method requires approximately half of the operations needed by the correlation based method; we note that the simplicity of the proposed method is already appreciable for a simple application, where the number of samples and the candidate periods are very small.

10.5 Conclusions

We derived analytically the optimal ML period estimator of a signal whose shape is unknown. Furthermore, we have presented a novel low complexity implementation of the ML estimator. The proposed method might have application in many areas where only the periodicity is required and the complexity is an important parameter. In particular, we applied the proposed algorithm to the remote heart rate estimation problem; as expected, both simulation and experimental results indicate that the proposed method outperforms the state of the art methods in detecting the period of weak signal like the heart beating, even with a short observation of the periodic signal.

By this period detection rule, if the target is breathing we will detect the respiration rate; to detect the heart beating we could cancel from the signal the respiration component. However, in the following we show that heart rate detection is possible

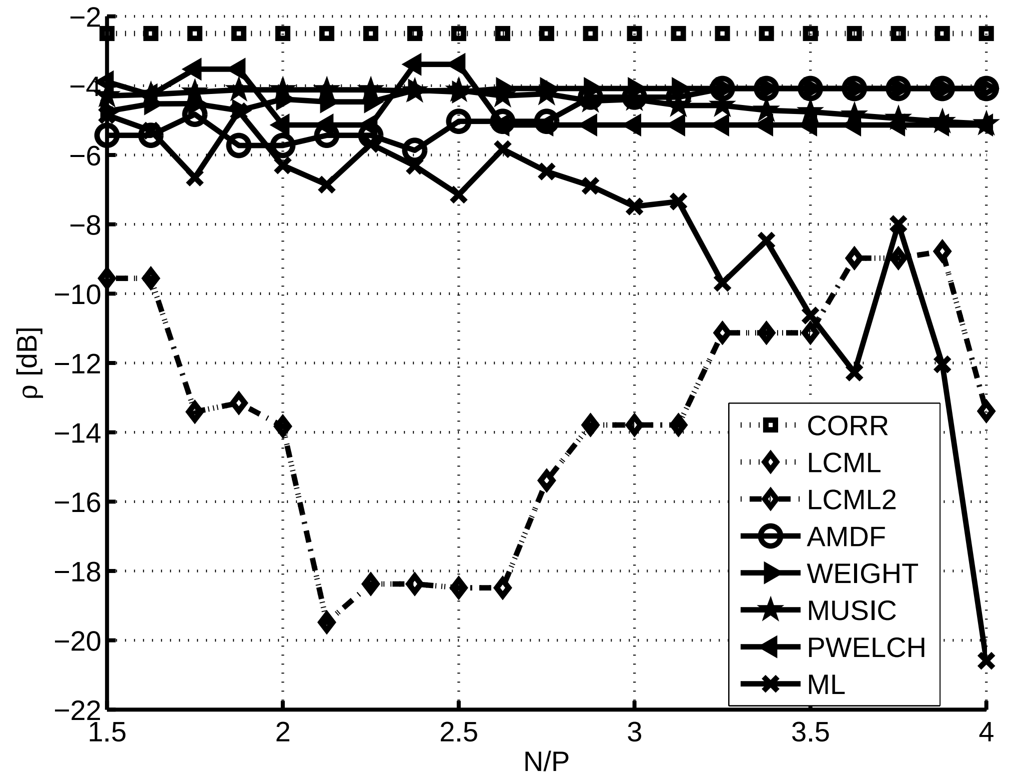

Figure 10.12: Normalized MSE of the estimated period as a function of N.

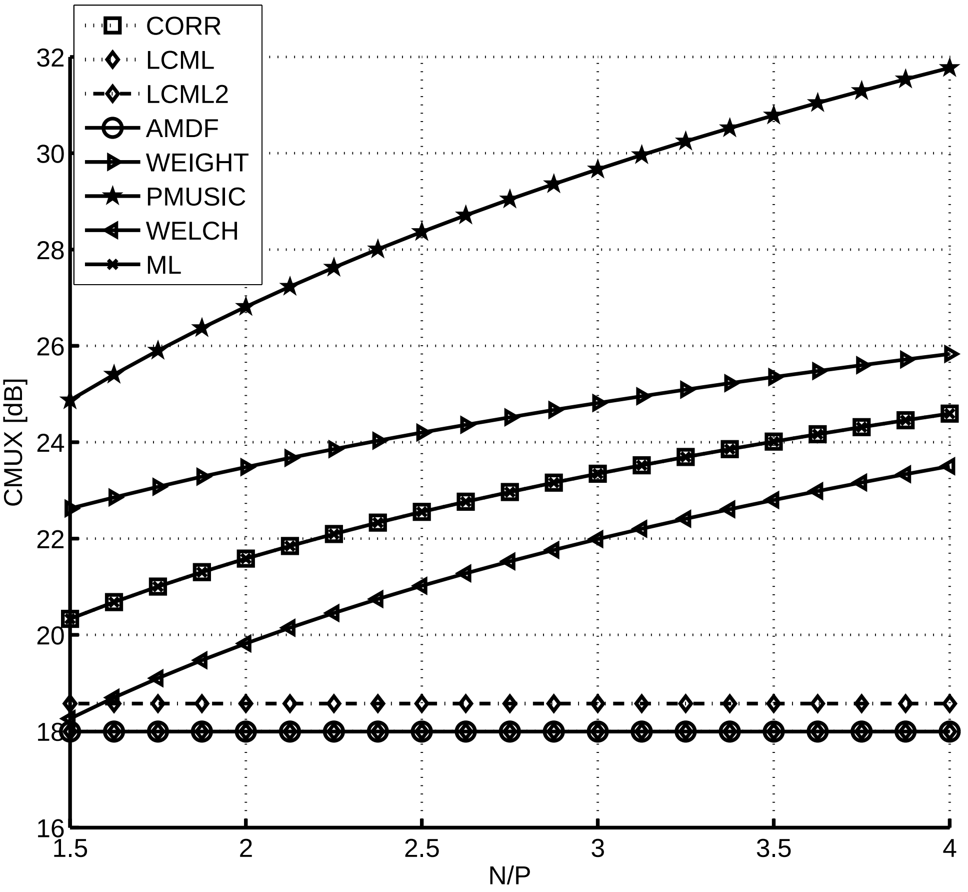

Figure 10.13: Complex multiplications required by the period detection algorithms as a function of N.

using the proposed method without further signal processing. The main difference between the proposed method and the correlation based technique is that in the first approach the autocorrelation is evaluated with P averages while the latter approach considers N averages.

Conclusions

In this second part of the thesis we addressed the topic of remote sensing of vital signs in an indoor scenario, onsidering a radar device working on the $3.1 - 5.3$ GHz band, which is available for consumer applications according to FCC rules. In particular we focus on describing the received signal with respect to the vital sign signal, and on detection techniques of respiration and heart beating rates. We have presented a simple and general model of the received signal for a Pulse UWB system in a indoor scenario with a human target; in particular, we described how the main parameters of the received signal is related to the chest motion of the target due to breathing and heart beating. A theoretical analysis for a wideband signal is performed for a 2.2 GHz system, compliant with FCC rules, showing that the received signal is affected both in phase and amplitude parameters by vital signs. Simulation results validates the theoretical analysis, showing that the amplitude modulation is due to both the wideband nature of the transmitted pulse, and to a multiple scattering effect provided by the chest surface.
Furthermore, due to the large number of parameters influencing the shape of the vital sign signal, we focus on blind detection techniques, which do not assume a defined shape. We have presented a extremely simple novel method to estimate the period of a periodic function. The analytical analysis and the simulation results indicate that the proposed method performs better than the correlation based method in detecting the period of weak signal like the heart beating.

Bibliography

[1] E. M. Staderini, "UWB radars in medicine," *IEEE Aerospace and Electronic Systems Magazine*, vol. 17, no. 1, Jan 2002.

[2] D. Tse and P. Viswanath, *Fundamentals of Wireless Communication*, Cambridge University Press, 2005.

[3] G. Caire and S. Shamai, "On the achievable throughput of a multiantenna broadcast Gaussian channel," *IEEE Trans. Inform. Theory*, vol. 49, pp. 1691–1706, July 2003.

[4] T. Yoo and A. Goldsmith, "On the optimality of multiantenna broadcast scheduling using zero-forcing beamforming," *IEEE J. Select. Areas Commun.*, vol. 24, no. 3, pp. 528–541, Mar. 2006.

[5] T. Yoo and A. Goldsmith, "Sum-rate optimal multi-antenna downlink beamforming strategy based on clique search," in *Proc. IEEE Global Commun. Conf. (GLOBECOM)*, St. Louis, MO, Nov. 2005.

[6] Z. Shen, R. Chen, J. G. Andrews, R. W. Heath, and B. L. Evans, "Low complexity user selection algorithms for multiuser MIMO systems with block diagonalization," *IEEE Trans. Signal Proc.*, vol. 54, no. 9, pp. 3658–3663, Sept. 2006.

[7] J. Wang, D. J. Love, and M. D. Zoltowski, "User selection for the MIMO broadcast channel with a fairness constraint," in *Proc. Int. Conf. Acoustics, Speech and Signal Proc. (ICASSP)*, Honolulu,Hawaii,USA, Apr. 2007.

[8] H. Viswanathan and K. Kumaran, "Rate scheduling in multiple antenna downlink wireless systems," in *Proc. Allerton Conf. Commun., Control, Comput.*, Allerton, IL, Oct. 2001.

[9] C. Swannack, E. Uysal-Biyikoglu, and G.W.Wornell, “Low complexity multiuser scheduling for maximizing throughput in the MIMO broadcast channel,” in *Proc. Allerton Conf. Commun., Control, Comput.*, Allerton, IL, Oct. 2004.

[10] T. Yoo, N. Jindal and A. Goldsmith, “Multi-antenna broadcast channels with limited feedback and user selection,” *IEEE J. Select. Areas Commun.*, vol. 25, pp. 1478–1491, Sept. 2007.

[11] J. Diaz, O. Simeone, and Y. Bar Ness, “Sum-rate of MIMO broacast channels with one bit feedback,” in *Proc. Int. Symp. Information Theory (ISIT)*, Seattle, WA, June 2006.

[12] M. Kobayashi and G. Caire, “An iterative waterfilling algorithm for maximum weighted sum-rate Gaussian MIMO-BC,” *IEEE J. Select. Areas Commun.*, vol. 24, pp. 1640–1646, Aug. 2006.

[13] M. Fuchs, G. Del Galdo, and M. Haardt, “Low-complexity space-time-frequency scheduling for MIMO systems with SDMA,” *IEEE Trans. Vehic. Tech.*, vol. 56, no. 5, pp. 2775–2784, Sept. 2007.

[14] Mingyan Jiang, Francisco Rubio, Yong Wang, Jesus Gomez, and Dongfeng Yuan, “User selection for maximum sum-rate in multi-user and MISO system with evolutionary algorithm,” in *Proc. Int. Workshop on Cross Layer Design (IWCLD)*, Jinan, China, Sept. 2007.

[15] G. Dimic and N. D. Sidiropoulos, “On downlink beamforming with greedy user selection: performance analysis and a simple new algorithm,” *IEEE Trans. Comm.*, vol. 53, no. 10, Oct.

[16] M. Trivellato, F. Boccardi, and F. Tosato, “User selection schemes for MIMO broadcast channels with limited feedback,” in *Proc. IEEE Vehic. Tech. Conf. 2007 (VTC)*, Dublin, Ireland, Apr. 2007.

[17] A Alexiou, J Reis, and A Gameiro, “QoS-based multiuser scheduling in MIMO systems,” in *Proc. Personal Indoor and Mobile Radio Commun. Conf. (PIMRC)*, Berlin, Germany, sep 2005.

[18] C. Anton-Haro, P. Svedman, A. Alexiou, and A. Gameiro, “Cross layer scheduling for multi user MIMO systems,” *IEEE Commun. Mag.*, vol. 44, no. 9, pp. 39–45, Sept. 2006.

[19] P. Trifonov, E. Costa, and A. Filippi, “Adaptive coding in MC-CDMA/FDMA systems with adaptive sub-band allocation,” *European Trans. on Telecom. (ETT), Special Issues on MC-SS*, vol. 15, no. 3, May-June 2004.

[20] “Overview of the 3GPP long term evolution physical layer,” http://www.freescale.com/files/wireless_comm/doc/white_paper/3GPPEVOLUTIONWP.pdf, Jan 2003, Motorola.

[21] H. Ekstrom, A. Furuskar, J. Karlsson, M. Meyer, and S. Parkvall, “Technical solutions for the 3G long-term evolution,” *IEEE Commun. Mag.*, vol. 44, no. 3, pp. 38–45, Mar. 2006.

[22] N. Benvenuto, E. Conte, S. Tomasin, and M. Trivellato, “Low rate predictive feedback for the OFDM MIMO broadcast channel,” in *Proc. Tyrrhenian Int. Workshop on Digital Commun.*, Ischia Island, Naples, Italy, Sept. 2007, p. 72.

[23] E. Conte, S. Tomasin, and N. Benvenuto, “Scheduling strategies for multiuser MIMO OFDM systems with limited feedback,” in *Proc. IEEE Int. Symp. on Personal, Indoor and Mobile Radio Commun. (PIMRC)*, Cannes, France, Sept. 2008.

[24] E. Conte, S. Tomasin, and N. Benvenuto, “A simplified greedy algorithm for joint scheduling and beamforming in multiuser MIMO OFDM,” *to appear in IEEE Comm. Letters.*

[25] D. J. Love, R. W. Heath, W. Santipach, and M. L. Honig, “What is the value of limited feedback for MIMO channels?,” *IEEE Commun. Mag.*, vol. 42, no. 10, pp. 54–59, Oct. 2004.

[26] T. Yoo, N. Jindal, and A. Goldsmith, “Multi-antenna broadcast channels with limited feedback and user selection,” *IEEE J. Select. Areas Commun.*, vol. 25, no. 7, pp. 1478–1491, Sept. 2007.

[27] M. Kobayashi and G. Caire, “Joint beamforming and scheduling for a multi-antenna downlink with imperfect transmitter channel knowledge,” *IEEE J. Select. Areas Commun., 2007*, vol. 25, pp. 1468–1477, Sept 2007.

[28] K. Huang, J. G. Andrews, and R. W. Heath Jr., “Performance of orthogonal beamforming for sdma with limited feedback,” *IEEE Trans. on Veh. Tech.*, vol. 57, pp. 1959–1975, May 2006.

[29] M-Sharif and B. Hassibi, “On the capacity of MIMO broadcast channels with partial side information,” *IEEE Trans. Inform. Theory*, vol. 51, no. 2, pp. 506–522, Feb. 2005.

[30] D. J. Love, R. W. Heath, and T. Strohmer, “Grassmannian beamforming for multiple-input multiple-output wireless systems,” *IEEE Trans. Inform. Theory*, vol. 49, no. 10, pp. 2735–2747, Oct. 2003.

[31] D. J. Love and R. W. Heath Jr., “Grassmannian beamforming on correlated mimo channels,” in *in proc. IEEE Global Commun. Conf. (GLOBECOM) 2004*, Dallas, TX, USA, Dec 2004.

[32] N. Ravindran and N. Jindal, “Multi-user diversity vs. accurate channel feedback for mimo broadcast channels,” in *Proc. IEEE Int. Conf. on Commun. (ICC)*, May 2008.

[33] T. Yoo, N. Jindal, and A. Goldsmith, “Multi-antenna broadcast channels with limited feedback and user selection,” *submitted to IEEE Journal Sel. Areas in Comm.*, May 2006.

[34] N. Benvenuto, E. Conte, S. Tomasin, and M. Trivellato, “Predictive channel quantization and beamformer design for MIMO-BC with limited feedback,” in *Proc. Global Commun. Conf. (GLOBECOM)*, Washington, DC,USA, nov 2007.

[35] F. Boccardi, F. Tosato, and G. Caire, “Precoding schemes for the MIMO-GBC,” in *IEEE Int. Zurich Seminar on Communication*, Zurich, Feb. 2006.

[36] N. Benvenuto and G. Cherubini, *Algorithms for Communications Systems and their Applications*, Wiley, 2002.

[37] N. Benvenuto, E. Conte, S. Tomasin, and M. Trivellato, “Joint low-rate feedback and channel quantization for the mimo broadcast channel,” in *IEEE Africon’07*, Windhoek, Namibia, Sept. 2007.

[38] F. Boccardi, H. Huang, and A. Alexiou, “Hierarchical quantization and its application to multiuser eigenmode transmissions for mimo broadcast channels with limited feedback,” in *Personal, Indoor and Mobile Radio Communications(PIMRC 2007)*, Sept. 2007.

[39] M. Trivellato, F. Boccardi, , and H. Huang, "On transceiver design and channel quantization for downlink multiuser mimo systems with limited feedback," *IEEE J. Select. Areas Commun., special issue on Limited Feedback, Oct. 2008*, Oct 2008.

[40] L. Liu and H. Jafarkhani, "Novel transmit beamforming schemes for time-selective fading multiantenna systems," *IEEE Trans. on Signal Proc.*, vol. 54, no. 12, pp. 47–67, Dec. 2006.

[41] N. Benvenuto and G. Cherubini, *Algorithms for Communications Systems and their Applications*, Wiley, 2002.

[42] C. R. Murthy and B. D. Rao, "Quantization methods for equal gain transmission with finite rate feedback," *IEEE Trans. Signal Processing*, vol. 55, no. 1, pp. 233–245, Jan. 2007.

[43] Y. Linde, A. Buzo, and R. M. Gray, "An algorithm for vector quantizer design," *IEEE Trans. Commun.*, vol. 28, pp. 84–95, Jan. 1980.

[44] J.H. Conway, R. H. Hardin, and N. J. A. Sloane, "Packing lines, planes, etc.: packings in Grassmannian frames," Tech. Rep., AT&T Bell Laboratories, Apr. 1996, Available on-line: http://www.research.att.com/ njas/doc/grass.pdf.

[45] A. Gersho and R. M. Gray, *Vector Quantization and Signal Compression*, KAP, 1992.

[46] L. Hanzo, M. Münster, B.J. Chei, and T. Keller, *OFDM and MC-CDMA for Broadband multi-user Communications, WLANS and Broadcasting*, Wiley, 2003.

[47] P. Svedman, S. K.Wilson, M. V. Eyuboglu, Jr. L. J. Cimini, and B. Ottersten, "Opportunistic beamforming and scheduling for OFDMA systems," *IEEE Trans. Commun.*, vol. 55, no. 5, pp. 941–952, May 2007.

[48] M. Kountouris and D. Gesbert, "Memory-based opportunistic multi-user beamforming," in *Proc. Int. Symp. Info. Theory (ISIT)*, Adelaide, Australia, Sept. 2005.

[49] A. Jalali, R. Padovani, and R. Pankaj, "Data throughput of CDMA-HDR a high efficiency-high data rate personal communication wireless system," in *Proc. Vehic. Tech. Conf. (VTC)*, Tokyo, Japan, May 2000.

[50] J. Salo, G. Del Galdo, J. Salmi, P. Kyösti, M. Milojevic, D. Laselva, and C. Schneider, "Matlab implementation of the 3GPP spatial channel model," Tech. Rep., 3GPP TR 25.996, Jan. 2005, Available on-line : http://www.tkk.fi/Units/Radio/scm/.

[51] "SCM micro cell and urban canyon model," http://www.3gpp.org/ftp/tsg_ran/WG1_RL1/3GPP_3GPP2_SCM/ConfCall-10-20030130/, Jan 2003, Motorola.

[52] E.W: Jang, C. Younggeun, C. Ji-Woong, and J.M. Cioffi, "Scheduling algorithms for time-varying downlink channels," *IEEE Trans. Wireless Commun.*, vol. 7, no. 6, pp. 2063–2068, June 2008.

[53] Y. Xiao, J. Lin, O. Boric-Lubecke, and V.M. Lubecke, "Frequency tuning technique for remote detection of heartbeat and respiration using low power double-sideband transmission in the ka-band," *IEEE Trans. on Microwave Theory and Techniques*, vol. 54, no. 5, May 2006.

[54] R. M. Narayanan and M. Dawood, "Doppler estimation using a coherent ultrawide-band random noise radar," *IEEE Trans. on Antennas and Propagation*, vol. 48, no. 6, Jun 2000.

[55] A.G. Yarovoy, X. Zhuge, T.G. Savelyev, and L.P. Ligthart, "Comparison of UWB technologies for human being detection with radar," in *Proc. of the 37th European Microwave Conference*, Munich, Germany, Oct. 2007.

[56] G. Ossberger, T. Buchegger, E. Schimback, A. Stelzer, and R. Weigel, "Non-invasive respiratory movement detection and monitoring of hidden humans using ultra wideband pulse radar," in *Ultra Wideband Systems, Int. Workshop on*, 2004.

[57] Y. Liuqing and G.B. Giannakis, "Ultra-wideband communications: an idea whose time has come," *IEEE Signal Proc. Magazine*, vol. 21, no. 1, Nov. 2004.

[58] Federal Communication Commission, "Code of federal regulations, title 47: Telecommunications," Tech. Rep., Radio Frequency Devices, 2007.

[59] T.W. Barrett, "History of ultra wideband (uwb) radar and communications: Pioneers and innovators," in *Proc. Progress in Electromagnetics Symposium*, 2000.

[60] D.S. Garmatyuk and R. M. Narayanan, "Ultra-wideband continuous-wave random noise arc-sar," *IEEE Trans. on Geoscience and Remote Sensing*, vol. 40, no. 12, Dec. 2002.

[61] A. C. Guyton and J.E. Hall, *Textbook of Medical Physiology*, Saunders, 2005.

[62] V. Novak, P. Novak, J. de Champlain, A. R. Le Blanc, R. Martin, and R. Nadeau, "Influence of respiration on heart rate and blood pressure fluctuations," *Journal of Applied Physiology*, vol. 74, no. 2, 1993.

[63] C.G. Bilich, "UWB radars for bio-medical sensing: Attenuation model for wave propagation in the body at 4 GHz," Tech. Rep., University of Trento, 2006.

[64] C. Gabriel, "Compilation of the dielectric properties of body tissues at RF and microwave frequencies," Tech. Rep., Occupational and environmental health directorate Radiofrequency Radiation Division Brooks Air Force Base Texas (USA), 1996.

[65] A. Nezirovic, A.G. Yarovoy, and L.P. Ligthart, "Experimental verification of human being detection dependency on operational UWB frequency band," in *Proc. 2007 IEEE ICUWB*, Singapore, Sept. 24-26 2007.

[66] G. Ossberger, T. Buchegger, E. Schimback, A. Stelzer, and R. Weigel, "Non-invasive respiratory movement detection and monitoring of hidden humans using ultra wideband pulse radar," in *Proc. 2004 IEEE Joint UWBST and IWUWBS 2004*, May. 18-21 2004.

[67] C.G. Bilich, "Bio-medical sensing using ultra wideband communications and radar technology: A feasibility study," in *IEEE Pervasive Health Conference and Workshops, 2006*, 2006.

[68] Time Domain, "Pulson 210 technical documentation," in *Time Domain Doc.*, 2006.

[69] M. Welborn, M. Kolhno, R. Mc Laughlin, and R. Fisher, "Ds-uwb physical layer submission to 802.15 task group 3a," Tech. Rep., IEEE P802.15 Working Group for Wireless Personal Area Networks (WPANs), 2004.

[70] J. C. Russ, *The Image Processing Handbook*, CRC Press, 2006.

[71] E. Conte, A. Filippi, and S. Tomasin, "On the modulation of ultra wide band pulse radar signal by target vital signs," in *in Proc. Int. Symposium on Bioelectronics and Bioinformatics (ISBB2009)*, Melbourne, Australia, Dec. 9-11 2009.

[72] L.R. Rabiner, M.J. Chang, A.E. Rosenberg, and C.A. McGonegal, "A comparative performance study of several pitch detection algorithms," *IEEE Trans. on Acoustics, Speech and Signal Proc.*, vol. ASSP-24, no. 5, pp. 399– 418, Oct. 1976.

[73] B.G. Quinn and E. J. Hannan, *The Estimation and Tracking of Frequency*, Cambridge, U.K., Cambridge Univ. Press, 2001.

[74] M.J. Ross, H.L. Shaffer, A. Cohen, R. Freudberg, and H.J. Manley, "Average magnitude difference function pitch extractor," *IEEE Trans. on Acoustic, Speech, and Signal Proc.*, vol. ASSP-22, no. 5, pp. 353– 362, Oct. 1974.

[75] T. Shimamura and H. Kobayashi, "A weighted autocorrelation method for pitch extraction of noisy speech," *IEEE Trans. on Speech and Audio Proc.*, vol. 9, no. 7, Oct. 2001.

[76] P.D. Welch, "The use of fast Fourier transform for the estimation of power spectra: A method based on time averaging over short, modified periodograms," *IEEE Trans. Audio Electroacoustics*, vol. AU-15, pp. 70–73, June 1967.

[77] R.O. Schmidt, "Multiple emitter location and signal parameter estimation," *IEEE Trans. Antennas Propagation*, vol. 34, pp. 276–290, Mar. 1986.